Department of Mechanical and Aerospace Engineering

Faculty of Engineering

University of Strathclyde

University of Strathclyde Glasgow

Pore-scale dynamics of immiscible two-phase flow in porous and fractured media

Qingqing Gu

Submitted in fulfilment of the requirements for the degree of

Doctor of Philosophy

2019

This thesis is the result of the author's original research. It has been composed by the author and has not been previously submitted for examination which has led to the award of a degree.

Qingqing Gu
Glasgow, Scotland, July 2019

This thesis is in memory of my dearest mum.

Supervisors

Professor Yonghao Zhang
Department of Mechanical and Aerospace Engineering
University of Strathclyde
Glasgow, United Kingdom

Dr. William Dempster
Department of Mechanical and Aerospace Engineering
University of Strathclyde
Glasgow, United Kingdom

Examiners

Professor Kai Luo
Department of Mechanical Engineering
University College London
London, United Kingdom

Dr Sina Haeri
Department of Mechanical and Aerospace Engineering
University of Strathclyde
Glasgow, United Kingdom

"Everything can be taken from a man but one thing:
the last of the human freedoms
– to choose one's attitude in any given set of circumstances,
to choose one's own way."
– Viktor Emil Frankl (1905-1997)

Acknowledgement

First and foremost I would like to thank my supervisors Prof. Yonghao Zhang and Dr. William Dempster for giving me the opportunity to embark on this wonderful journey. I am greatly indebted to Prof. Yonghao Zhang for the time he spent being my mentor. It would be an impossible mission for me to finish this thesis without his patience and guidance. Prof. Yonghao Zhang has always been there to support me, offer his keen insight into academic problems and allow me the freedom to explore. In the jungle of pursuing the PhD, it is his leading that keep me in the right direction. I would also like to acknowledge Prof. Haihu Liu for his generous sharing of his immense knowledge of multiphase flow and critical view which made an invaluable contribution to this work. His endless passion towards science and truth has great influence on me and will continue to impact in my future career path.

I am also grateful to be a member of the James Weir Fluids Laboratory, my colleagues Prof. Jun Zhang, Dr. Thomas Burel and Dr. Peng Wang were there to offer unconditional support in the early stage of my PhD study. I am also very grateful to Nikos, Ferdin, Joana, Minh-Tuan and Paolo for their encouragement and advice during various stages of my PhD. It has been a very rewarding experience for me to work with everyone else who has contributed to the great dynamic in the James Weir Fluids Laboratory.

My thanks also goes to the support I received from Aileen Petrie and all the staff from the Department of Mechanical and Aerospace Engineering at University of Strathclyde. I am also grateful to the department and the university for providing the PhD training including the Researcher Development Programme which contributed to my development as a researcher.

I greatly acknowledge the University of Strathclyde for the studentship and the China

Scholarship Council for the maintenance to support my PhD. My time at Strathclyde was enriched by Ya Zhang, Dr. Yuchen Wang, Dr. Wei Su, Yuan Yu, Weiqi Yang, Dr. Lei Wu and his family, thank you all for the great time spent together in Scotland. Special thanks to Yaling Lu, Chenhui Kong, Qin Yao and Xiao Xiao for the long-lasting friendship and happiness you have brought even far away from me.

I would also like to thank the thesis examination committee for their time and constructional suggestions that improve the quality of this thesis.

Lastly, I thank my family for their love and encouragement. For my parents who raised me with love and always believing in me. For the presence of my sister in UK for one of my years here and the optimism and wisdom she sheds on me. And most of all, for my loving and caring fiance whose faithful support during the final stages of this PhD is also deeply appreciated.

Qingqing Gu
Glasgow, Scotland
July, 2019

Scientific Contribution

- Journal Papers

  1. Gu, Q. and Liu, H. and Zhang, Y., *Lattice Boltzmann Simulation of Immiscible Two-Phase Displacement in Two-Dimensional Berea Sandstone*, Applied Sciences, 2018, 8, 1497. DOI: 10.3390/app8091497.
  2. Gu, Q. and Zhu, L. and Zhang, Y. and Liu, H. , *Pore-scale study of counter-current imbibition in strongly water-wet fractured porous media using lattice Boltzmann method*, Physics of Fluids, 2019, 31, 086602. DOI: 10.1063/1.5099500.

- Conference Presentations

  1. 2017, 14th International Conference for Mesoscopic Methods in Engineering and Science (ICMMES), Nantes, France, oral presentation titled "Lattice Boltzmann Simulation of immiscible displacement of binary fluids in porous media".
  2. Droplets 2019, poster presentation titled "Pore-scale study of counter-current imbibition in strongly water-wet fractured porous media using lattice Boltzmann method".

Abstract

Pore-scale investigations of immiscible two-phase flow displacement dynamics in porous media provides crucial information to natural and industrial processes such as non-aqueous phase liquid (NAPL) contamination of groundwater, carbon dioxide injection and storage, and enhanced oil recovery (EOR) operations. It has the potential to transform our understanding of multiphase flow processes, to improve oil and gas recovery efficiency, and to facilitate safe carbon dioxide storage. However, the modelled pore-space geometry is naturally complex for these fields of application. For directly simulating multiphase flow within the complex structure, the most widely-used approach is the lattice Boltzmann method (LBM).

In this thesis, the implementation of the state-of-the-art colour gradient two-phase LBM has been validated against the theoretical solution for capillary filling, and analytical solutions for relative permeabilities in a cocurrent flow in a 2D channel. Then it is employed to investigate the effects of interfacial tension, wettability, and the viscosity ratio on displacement of one fluid by another immiscible fluid in a two-dimensional (2D) Berea sandstone. Through invasion of the wetting phase into the porous matrix, it is observed that the viscosity ratio plays an important role in the non-wetting phase recovery. At the viscosity ratio (λ) of unity, the saturation of the wetting fluid is highest, and linearly increases with time. The displacing fluid saturation reduces drastically when λ increases to 20; however, when λ is beyond 20, the reduction becomes less significant for both imbibition and drainage. The front of the bottom fingers is finally halted at a position near the inlet as the viscosity ratio increases to 10. Increasing the interfacial tension generally results in higher saturation of the wetting fluid. Finally, the contact angle is found to have a limited effect on the efficiency of displacement in the 2D Berea sandstone.

In addition, it has also been utilized to provide a better understanding of spontaneous imbibition, a key oil recovery mechanism in the fractured reservoir rocks. A pore-scale computational study of the water imbibition into an artificially generated dual-permeability porous matrix with a fracture attached on top is conducted. Several factors affecting the dynamic counter-current imbibition processes and the resulting oil recovery have been analysed, including the water injection velocity, the geometry configuration of the dual permeability zones, interfacial tension, viscosity ratio of water to oil phases, and fracture spacing if there are multiple fractures. By examining different water injection velocities and interfacial tensions, it is identified for the first time that the three distinct imbibition regimes exist: the squeezing regime, the jetting regime and the dripping regime, and they can be distinguished with different expelled oil morphologies in the fracture (piston-like plug, elongated liquid thread or isolated drops). The geometry configuration of the high and low permeability zones affects the amount of oil that can be recovered by the counter-current imbibition in a fracture-matrix system through transition of the different regimes. In the squeezing regime, which occurs at low water injection velocity, it is interestingly found that the built-up squeezing pressure upstream in the fracture enables more water to imbibe into the permeability zone closer to the fracture inlet thus increasing the oil recovery factor. A larger interfacial tension or a lower water-to-oil viscosity ratio is favorable for enhancing oil recovery and new insights into the effect of viscosity ratio are provided. Introducing an extra parallel fracture can effectively increase the oil recovery factor and there is an optimal fracture spacing between the two adjacent horizontal fractures to maximize the oil recovery. These findings can aid the optimal design of water-injecting oil extraction in fractured rocks in reservoirs of low permeability like oil-bearing shale or tight sandstone.

We conclude that the pore-scale modelling can act as a reliable tool to assess and predict oil and gas resources and facilitate more efficient oil and gas recovery.

Contents

List of Figures

List of Tables

Nomenclature

Acronyms

BGK Bhatnagar-Gross-Krook

CFD Computational Fluid Dynamics

CO_2 Carbon Dioxyde

DVBE Discrete Velocity Boltzmann Equation

EDF Equilibrium Distribution Function

EOR Enhanced Oil Recovery

FD Finite Difference

GPBC Generalized Periodic Boundary Condition

HPC High Performance Computing

LBE Lattice Boltzmann Equation

LBM Lattice Boltzmann Method

LGA Lattice Gas Automata

LS Level Set

MRT Multiple-relaxation-time

NAPL Non-aqueous Phase Liquid

NSE Navier-Stokes Equation

NWP Non-wetting Phase

PFM Phase-field Method

PNM Pore Network Modelling

REV Representative Elementary Volume

SPH Smoothed Particle Hydrodynamics

VOF Volume of Fluid

WP Wetting Phase

Greek symbols

δ_t Simulation time step

δ_x Lattice distance between neighbouring lattice nodes

η Dynamic viscosity

γ Specific weight

λ Viscosity ratio; pore-size distribution index

ν Kinetic viscosity

ω_i Weight coefficient associated with the discrete velocity c_i

ϕ Order parameter

ρ Density

ρ^N Phase field

σ Interfacial tension

τ Relaxation time

θ Fluid-fluid contact angle with the solid surface

ξ Particle velocity

Latin symbols

$\vec{c_i}$ Discrete velocity (vector)

$\vec{n_c}$ Corrected unit normal vector

$\vec{u}$ Velocity (vector)

$\vec{x_s}$	Solid nodes position (vector)
c_0	A structure-dependant constant
c_s	Lattice speed of sound
Ca	Capillary number
D	Euclidean distance
K	Intrinsic permeability
K_{rnw}	Nonwetting fluid relative permeability
K_{rw}	Wetting fluid relative permeability
Kn	Knudsen number
l_0	Length scale for lattice unit conversion
l_h	Characteristic physical length
l_m	Molecular mean free path
m_0	Mass scale for lattice unit conversion
n	Porosity
p	Pressure
P_b	Entry capillary pressure
P_c	Capillary pressure
Re	Reynolds number
S	Specific surface area of the medium; Saturation
S_e	Effective wetting fluid saturation
S_r	Residual wetting fluid saturation
t_0	Time scale for lattice unit conversion
x_e	Effective length
$\vec{a}$	Acceleration caused by external force
$\vec{C}$	Particular velocity

F Body force

k_B Boltzmann constant

m Molecular mass

R Gas constant

T Temperature

Mathematical Operators

∂ Partial derivative

Superscripts

eq Equilibrium

phy Physical unit

Subscripts

$displaced$ The displaced fluid during displacement process

i Discrete velocity index

inj Injection

$invading$ The advancing fluid during displacement process

nw Nonwetting fluid

oil Oil

w Wetting fluid

$water$ Water

Other symbols

∇ Differential operator

∇^2 or $\nabla \cdot \nabla$ Laplace operator

Chapter 1

Introduction

1.1 Background

The simultaneous flow of two immiscible fluids in porous media is of great interest in nature and many industrial processes such as non-aqueous phase liquid (NAPL) contamination of groundwater, carbon dioxide injection and storage, and enhanced oil recovery (EOR) operations. The fluid flow in porous media is complicated mainly due to the highly heterogeneous and complex geometry of the porous structure and the usually nonlinear and coupled transport phenomena of the two immiscible fluids inside. In petroleum engineering, the porous media refers to the hydrocarbon reservoirs with a porous geologic formation that contains hydrocarbon (oil or gas) in its pore space as well as connate water. Within this thesis, we consider the oil recovery from reservoirs. We focus on the immiscible displacements with both capillary and viscous effects (the inertial effect is taken into consideration but its effect is negligible at low Mach number, the gravitational effect is neglected since the ratio of gravity to capillary force is very small [10], i.e., low Bond number). The physics of fluid displacement at the pore scale plays a key role in determining the overall movement of the fluids, consequently deciding how much oil can be recovered. However, many difficulties remain for the transport properties within the rocks to be properly understood. One way is to determine the transport properties of porous media by experiment in laboratories, however, it is usually costly in terms of time and resources and requires highly-skillful technical operation. Moreover, one can measure only a limited amount of physical variables. Apart from the experimental efforts, theoretical analysis can be a useful tool, but it is usually limited for simplified pore geometries which admit theoretical solutions to the microscopic flow patterns [9].

With the continuing and rapid development of the computational power, computational simulation provides an increasingly reliable alternative tool for this problem. Moreover, numerical simulations can be performed when laboratory experiments are impossible due to technical limitations. As a complementary method to the experimental and theoretical approaches, accurate and reliable numerical tools are needed to understand the underlying mechanisms of multiphase displacement. Conventional macro-scale simulations have achieved great success in solving the continuity, momentum, and species balance equations which require some inputs for semi-empirical parameters such as relative permeabilities. This approach, however, may not be able to capture effects related to microscale structure in multiphase flows. For example, the capillary trapping mechanism has a huge impact on the evaluated relative permeability for predicting the distribution and mobility of the immobilised fluid in the reservoir [11]. On the contrary, pore-scale simulation provides an important means to improve our understanding of the underlying physical processes and to determine macroscale constitutive relationships, for example the capillary pressure-saturation relation.

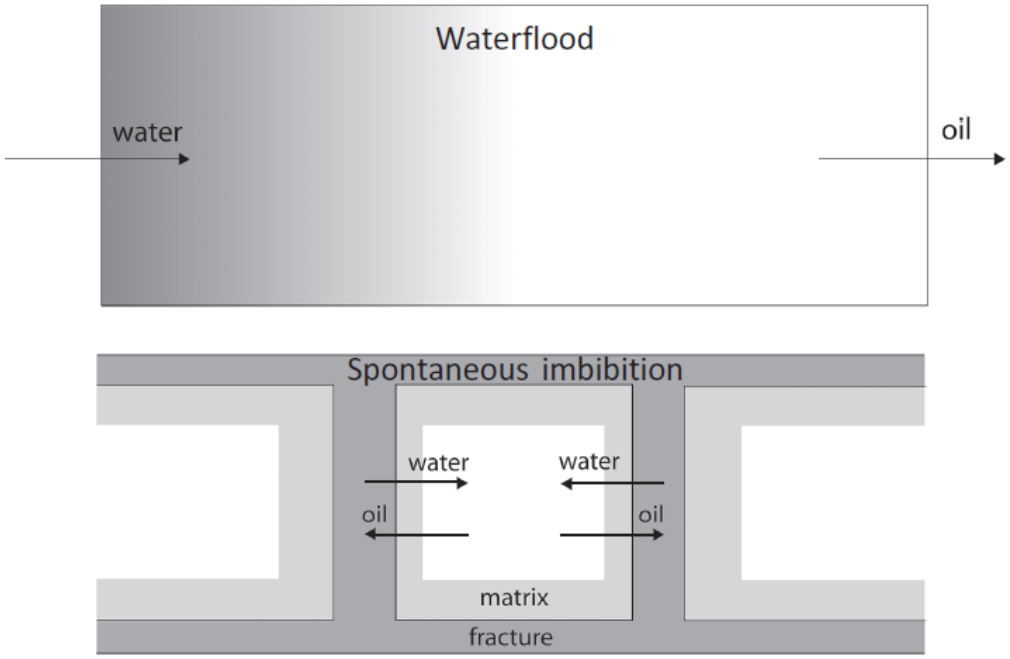

Figure 1.1: Schematic of the viscous displacement or waterflooding (top) and spontaneous imbibition (bottom) process of oil recovery. In waterflooding, the capillary pressure term in the governing flow equations is relatively small compared to viscous forces, and mainly affects the fluid front; while in spontaneous imbibition, the displacement process is entirely caused by capillary forces, it often occurs when we can not exert a significant viscous pressure drop across a region of rock [1].

As a mesoscopic method, the lattice Boltzmann method (LBM) has been widely accepted as a useful alternative for simulating multiphase flows, in particular, with the advantage of dealing with complex geometries such as porous media [12]. In other pore scale modelling methods such as pore-network modelling, the porous medium is idealised as some simple geometries which could lead to loss of geometrical and topological information. However, the LBM can be used to solve equations in an arbitrary pore space geometry and topology without simplification. Nevertheless, the high computational cost and memory demand restrict our study in two dimensional even with high performance computer (HPC). As will be introduced in detail in Chapter 2, the LBM is easy to implement compared with other CFD algorithms and with good locality which is ideal for parallel computing. In this thesis, the state-of-the-art lattice Boltzmann colour-gradient method is first utilised for dynamic displacement of immiscible fluids in a complex porous flow structure extracted from a realistic Berea sandstone sample, and study the effects of the viscosity ratio, interfacial tension, and contact angle on the displacement process. Then it is used to understand and quantify the dynamic imbibition process and oil recovery within the low permeability fractured rocks.

1.2 Literature review

As shown in Fig. 1.1, there are two generic recovery processes in oil reservoirs when water is injected: direct **viscous displacement** (simply termed as **waterflooding**) and **spontaneous imbibition** [1]. In the waterflooding process, water pushes out oil in a process controlled by the imposed injection rate or pressure difference between water and oil. The pressure difference between the injection and production wells is typically much larger than the capillary pressure, thus the displacement process is dominated by viscous forces while the capillary forces control the local distribution of fluids. While in fractured media, or reservoirs with large permeability contrast, the other recovery process – spontaneous imbibition is observed. In a fracture-matrix system as shown in bottom of Fig. 1.1, the interconnected fractures form a short-circuit for flow, where it is not possible to impose a significant viscous pressure drop across a single region of rock surrounded by the fractures. In this case oil can only be recovered providing that water imbibes into the matrix. This process of the wetting fluid – typically water – being imbibed into the porous rock matrix due to the capillary pressure without any external driving force is called the spontaneous imbibition. The spontaneous imbibition can be co-current or counter-current, depending on whether the water and oil transport in the same (co-current) or opposite (counter-current) directions [13], as illustrated in

Fig. 1.2.

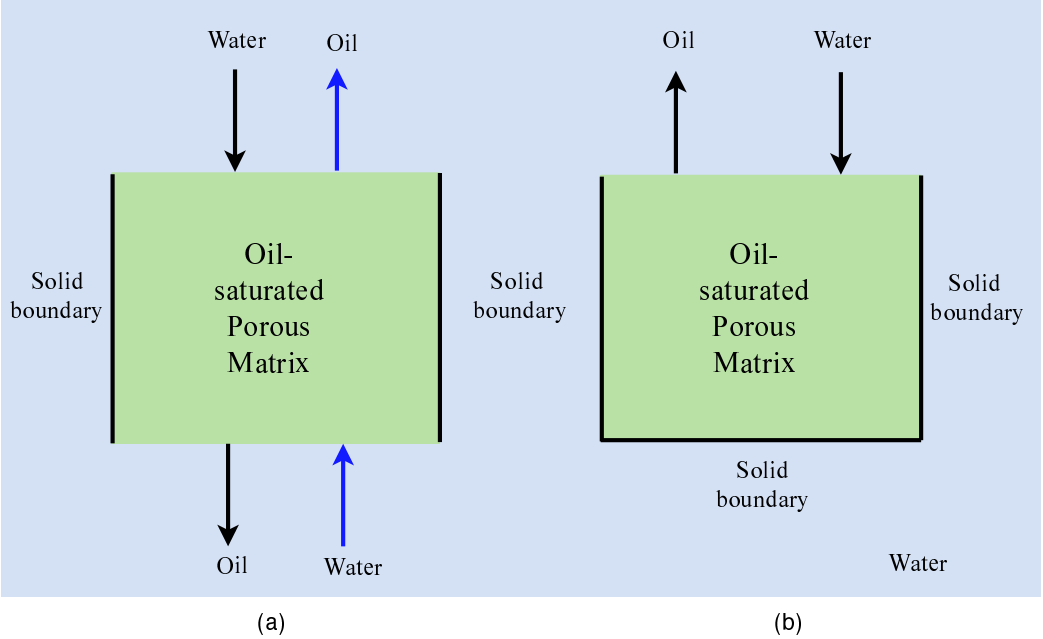

Figure 1.2: Schematic of the (a) co-current imbibition: the expelled oil and the imbibing water (see arrows in the same colour) flow in the same direction, and (b) counter-current imbibition: the expelled oil and the imbibing water (black arrows) flow in the opposite directions.

1.2.1 Viscous displacement (Waterflooding)

Many experimental efforts have been made to understand interactions between fluids and rock during fluid displacement. They mainly used two categories of porous media, either natural media such as rock cores or transparent network models known as micromodels. Rock cores are advantageous for characterizing individual formations, however, they rely on sophisticated and bespoke laboratory facilities such as micro-CT or synchrotron scanner to image the rock samples and visualize the internal fluids distribution within the rock cores. While for micromodels, which are two-dimensional pore network patterns etched into materials such as silicon, glass, polyester resin, and most recently, polydimethylsiloxane (PDMS) [14], visualization of fluid distribution can be done using cameras with or without fluorescent microscopy. Fluid saturation and interfacial area can be quantified and may provide a better understanding of physical displacement processes at the microscopic level. Moreover, the micromodels are ideal for parametric investigation with porosity, pore size, connectivity, and wetting properties can be independently manipulated. For example, an early study of Lenormand et al. [15] conducted

experiments with a micromodel using transparent polyester resin. They observed several different mechanisms by which one fluid can be displaced by another, for example the basic 'piston-type' motion and 'snap-off' for the displacement of the meniscus in a duct and two types of imbibition pattern (imbibition I1 and I2) at the intersection of four ducts. As a pioneering work, a phase-diagram for immiscible displacement of wetting fluid by injection of the non-wetting fluid (known as drainage) characterized by two dimensionless numbers, i.e., the capillary number $Ca = (\eta_n u_n)/(\sigma_{nw} \cos\theta)$, which represents the ratio of viscous forces to capillary forces experienced by a nonwetting fluid during displacement, and the viscosity ratio $\lambda = \eta_n/\eta_w$, was proposed by Lenormand et al. [3] with a oil-wet micromodel. Herein, η_n and u_n are the viscosity and velocity of the advancing nonwetting fluid (subscript n), σ_{nw} is the interfacial tension between the wetting (subscript w) and nonwetting fluid, θ is the fluid-fluid contact angle with the solid surface. They identified three different displacement regimes: (a)

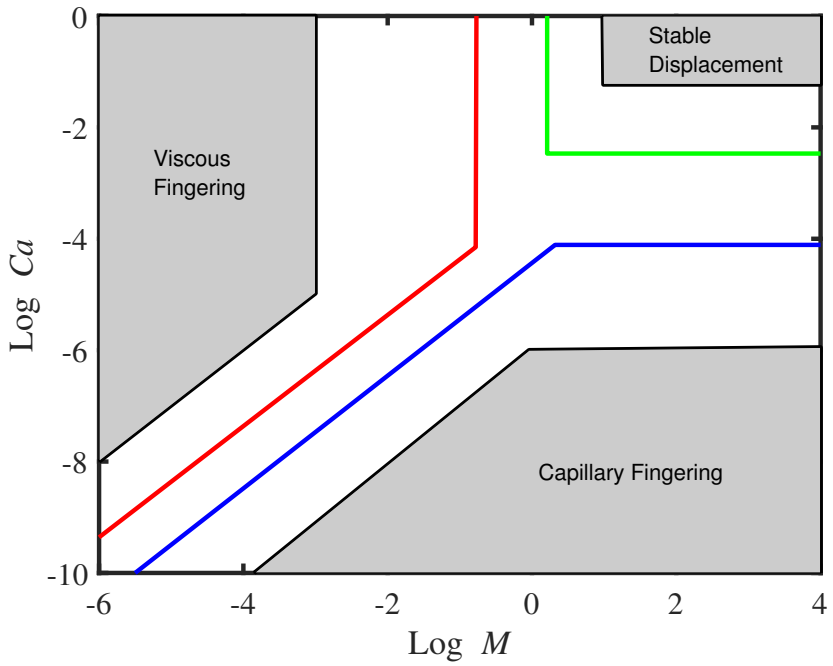

Figure 1.3: log M - log Ca phase diagram showing the three displacement zones bounded by solid lines obtained by Zhang et al. [2] and the gray zones denoted the zones obtained by Lenormand et al. [3].

viscous fingering, (b) capillary fingering, and (c) stable displacement. They also presented the existence of a crossover zone, for example, when the nonwetting phase is less viscous than the wetting fluid ($\lambda < 1$), the invasion pattern varies from capillary fingering ($log_{10}Ca \sim -8.0$) to viscous fingering ($log_{10}Ca \sim -3.0$) [3] as can be seen from Fig. 1.3. Great efforts have been made to investigate this crossover zone using

both experiments [16, 17, 18, 19] and numerical simulations [20]. With the considerable improvement of techniques such as precise microfabrication, fluid saturation visualization and image analysis, a series of displacement experiments were conducted by Zhang et al. [2] in a homogeneous water-wet pore network micromodel which extend the fundamental contributions by Lenormand et al. [3]. They found that the boundaries that divide the different regimes are strongly dependent on the pore network. Worse still, micromodels are often criticized for the lack of the complex geometry of real media, which often ignores the multiscale and random characteristics that may dominate the fluid and solute transport.

In addition to experimental studies, pore-scale modelling has developed rapidly as a predictive tool used in the oil industry. Pore-scale simulations are important because pore-scale phenomena have an important impact on larger-scale phenomena, e.g., field scale displacement. Unlike experiments, it is easy to change fluid properties, pore space geometries and boundary conditions systematically in computational simulations [21]. To the best of my knowledge, there are mainly two ways to compute properties in the pore space. The first one is the direct simulation approach, where the governing equations of fluid transport are computed on the image itself. This could be computationally demanding and the computational accuracy is subject to the resolution of the image. The other approach is pore network modelling (PNM), which is first to extract a topologically representative network with idealised properties derived from the image, then to compute the fluid flow through this network composed of pores and throats in a usually semi-analytical way [22]. This approach is well-tailored for the study of capillary-controlled displacement, providing infinite resolution in the network elements. However, apparently a number of approximations are made concerning the pore space geometry in this approach. And it is challenging to extract topologically and geometrically equivalent pore networks that are representative for certain classes of rocks [23].

The most popular way to directly compute multiphase flow from pore-scale images is the lattice Boltzmann method [24]. The most appealing features of LBM lie in easy handling of complex boundary conditions and amenability to parallel computing. As a mesoscopic model, it is able to correctly reproduce macroscopic behaviour while capturing local microscopic effects. The kinetic nature enables the LBM to automatically maintain fluid interfaces that do not need to be tracked. In comparison, conventional numerical methods for multiphase flow simulations include level set (LS) [25], volume of fluid (VOF) [26, 27, 28, 29], phase-field (PF) model [30] and smoothed particle hydrodynamics (SPH) [31] rely on auxiliary algorithms to track the fluid interfaces in

addition to solving the macroscopic flow equations [23].

In addition, LBM offers a convenient way to simulate the true pore geometry of a porous medium system for both the single phase and multiphase flows. It is based on a complete description of the pore structure and hence can only be applied to porous media when the representative elementary volume (REV) (see in Section 3.2.2) is big enough to allow an appropriate resolution of the smallest single pores, e.g., by high-resolution X-ray tomography. A number of multiphase and multicomponent LB models are readily available to simulate flows in complex geometries on a pore scale level, which will be introduced in section 2.4.

Early in 1995, Ferréol and Rothman [32] have successfully applied the lattice Boltzmann method to simulate single-phase and two-phase flow through a 3D tomographically-reconstructed image of Fontainebleau sandstone. They have found that the permeability strongly depends on the viscosity when the grid resolution is not enough, and the effect of grid resolution decreases as the viscosity decreases. They also presented preliminary qualitative results for simulations of drainage and imbibition in the early displacement stage (before reaching steady state), and the behaviours of the invading fluids are roughly within expectation. Martys and Chen [33] used the three-dimensional Shan-Chen model to simulate the wetting and non-wetting fluids in a porous geometry generated by a microtomography image of Fontainebleau sandstone. However, the numerical method adopted was primitive and the computational resolution might be too low for obtaining meaningful results.

Tölke et al. [34] introduced an improved three dimensional colour gradient LB model for immiscible binary fluids with variable viscosity and density ratio by reducing the spurious currents in the interface regions. The interface is less sharp than the original model by Gunstensen et al. [35] but the stability is improved. Still, the convergence study with respect to grid refinement was absent and for simulations of large-scale problems in reality, the stability constraints pose a major limitation with the Bhatnagar-Gross-Krook (BGK) collision operator (see section 2.2). A synthetic packing with a relatively uniform distribution of spheres was simulated by Pan et al. [36] with three-dimensional Shan-Chen model, although encouraging agreement between the simulated hysteretic P-S (capillary pressure–saturation) relations and experimental data was obtained, the simulated cubic domain is not large enough to be a representative elementary volume (REV) (see section 3.2.2).

Manwart et al. [37] compared the lattice Boltzmann method (LBM) and the conventional finite difference (FD) method by performing numerical tests of permeability for four samples, i.e., one microtomographic image of Fontainebleau sandstone, two

stochastic reconstructions and one physical model for the Fontainebleau sample. They concluded that both the LB and FD methods are applicable to solve equations within the three-dimensional porous medium. However the numerically determined fluid permeability should be taken with caution as it may depend on the boundary conditions, size of the sample, and the resolution of the microstructure. Comparison of the lattice Boltzmann model (three dimensional colour gradient model) and the pore network model has also been done by Vogel et al. [38], they reported consistent results for predicting the primary drainage curve. Their work is based on detailed representations of the complex porous structures as measured by X-ray tomography, and concluded that the LB model is advantageous to provide a detailed analysis of multiphase dynamics despite the limitation of insufficient resolution of thin water films with uniform grids.

Li et al. [39] investigated the effect of capillary number, wettability and viscosity ratio on the conventional relative permeabilities in co-current two-phase flow through a sphere pack porous medium with the D3Q19 Shan-Chen multicomponent LB model. The dependence of the permeability-saturation curve on the capillary number, wettability, and viscosity ratio evidenced that the permeability is not only dependant on the fluid saturation, but also the fluid-fluid interfacial area. There are also studies that compare the LBM with the experimental data. For example, Schaap et al. [40] compared the pressure-saturation curve from experimental and LBM results using D3Q19 Shan-Chen multiple-relaxation-time model, however a good match is observed only for the liquid-air system, large differences exists for the liquid-liquid system. This might be the result of unreasonable assumption that the contact angle is zero in both the liquid-air and liquid-liquid systems. Ahrenholz et al. [41] compared the D3Q19 colour gradient multiple-relaxation-time model with the experimental data and suggested that for the air-water drainage process, the air-entry pressure and the slope of the drainage curve can be predicted very well while the residual water saturation is more difficult to be accurately estimated by the LB approach due to the limited resolution of the thin-film flow. Ramstad et al. [23] reproduced the unsteady and steady-state displacements for measuring relative permeability with LB simulations on pore images of water-wet Bentheimer and Berea sandstone, and compared the computed relative permeabilities with available experimental data. It is demonstrated that the LB model is able to produce the drainage and imbibition permeability curves that are comparable to the experimental data with steady-state setups, although the nonwetting fluid relative permeability for unsteady-state drainage simulations is over-predicted. Other previous works on pore-scale simulation of immiscible two-phase flows in porous media [42, 43, 44, 45, 46, 47] have been shown to be capable of capturing the effects of various factors, e.g., capillary number, viscosity ratio, surface wettability, and media

heterogeneity. However, due to the inherent complexity related to interface evolution, heterogeneous geometry, dominant capillarity, and moving contact line, the computational simulation of multiphase displacement in realistic porous media still remains a research challenge.

1.2.2 Spontaneous imbibition

Fractured petroleum reservoirs typically represent over 20% of the world's oil reserves [48]. Such reservoirs are poorly understood and oil recovery from fractured reservoirs is typically lower than that from conventional reservoirs. For conventional reservoirs, water flooding is one of the primary techniques to enhance oil recovery (EOR), in which water is injected to displace oil from the porous matrix under the pressure difference. However, for the low permeable fractured reservoirs, the water-flooding displacement is often not productive because the limited connectivity among the pores cannot guide effectively the flow of the expelled oil along the pressure gradient [49].

Yet still, in many naturally fractured reservoirs, the spontaneous imbibition (also known as capillary imbibition) provides a special mechanism for oil recovery from the matrix which does not rely on the imposed pressure gradient. In the spontaneous imbibition, the wetting fluid is imbibed into the porous rock matrix due to the capillary pressure without any external driving force. The oil in the rock matrix is expelled and flows into the fractures due to the spontaneous imbibition of water into the matrix from the fractures. In this work, we focus on the **counter-current imbibition** [Fig. 1.2(b)], where the wetting phase and non-wetting phase flow in/out of the matrix at the same side, and enclosed (by wall) matrix is necessary for such flow to occur. The counter-current imbibition occurs more often although it is less effective in terms of oil recovery. The spontaneous imbibition is known to be affected by many factors including the wettability [50], the porosity, permeability and heterogeneity of the matrix [51, 52, 53, 54, 55, 56, 57], the viscosity ratio of the wetting to non-wetting fluids [58, 59] and their interfacial tension [60, 61], as well as initial saturation and boundary conditions [56, 60, 62], etc.

The spontaneous imbibition in conventional porous media has been extensively studied [15, 63, 64, 65] due to its wide existence in various disciplines such as oil recovery, polymer composite manufacturing, soil science and subsurface hydrology. For the fractured porous medium, however, it has not been fully understood and starts to attract research attention. Rangel-German and Kovscek [66] experimentally investigated the underlying flow physics of the counter-current imbibition in various fracture apertures

using an X-ray computerized tomography (CT) scanner. By changing the water injection rates through the fractures, they have identified two spontaneous imbibition regimes, i.e., the "filling fracture" and the "instantly filled fracture" regimes which correspond to significantly different imbibition behaviors. Later, they further verified such a finding by micromodel experiments with the aid of pore-scale imaging techniques. Jafari et al. [67] studied the effect of fracture network topology, pore sizes distribution and structure of matrix and injection rate on the spontaneous imbibition using a glass micromodel.

In addition to experimental studies, pore-scale numerical simulations have also been exploited to understand spontaneous imbibition. Pore-scale simulations allow easy access to a wide range of parameters and the imbibition process can be readily visualised so that its underlying mechanism can be analyzed accordingly in a more controllable manner. Moreover, numerical simulations are superior to theoretical analysis when it comes to geometrically complex problems with nonlinearity [55]. Rokhforouz and Amiri [50] used the phase-field method to study the effect of wettability, interfacial tension, and viscosity ratio during counter-current imbibition process. Jafari et al. [55] also used the phase-field method to investigate the effects of water injection velocity, fracture aperture, and grain shape during counter-current spontaneous imbibition. In these pore-scale simulations, the solid grains in the matrix are generally idealized as simple circular [50, 55] or square cylinders [68]. However, the pore structures in natural rock matrix are extremely complex and irregular. In this work, we conduct the pore-scale study of the counter-current imbibition in a matrix-fracture system using a recently improved lattice Boltzmann (LB) colour-gradient model [69]. Among various multiphase LB models (see the reviews by Huang et al. [70] and Liu et al. [71]), the colour-gradient model has its own advantages such as high numerical accuracy, strict mass conservation for each fluid and numerical stability for a broad range of viscosity ratios [69]. Especially, it produces relatively thin interface and is able to control the interfacial diffusion and adjust the interfacial tension and viscosity independently to facilitate the numerical investigation [72]. Therefore, the colour-gradient model has been extensively used for modeling immiscible two phase flow in porous media, e.g. Tolke et al. [34], Huang et al. [73], Chen et al. [74], Gu et al. [72] and Xu et al. [75].

1.2.3 Summary

Although significant efforts have been made by a large number of researchers, it is still challenging to accurately and reliably simulate multiphase fluid dynamics for the full range of density ratios, viscosity ratios and wetting behaviours in oil reservoir. Con-

sidering that the viscosity contrast is large while the density difference is small for the water or carbon dioxide involved oil recovery process, the colour gradient model is the perfect candidate for simulations in this context. Previous pore-scale numerical simulations are either limited to simplified flow physics and/or simple geometry configuration/size.

The computational challenge for multiphase flow in porous media simulation is a direct consequence of the microscopic porous structure and the physicochemical properties of interfaces. The most important parameters for two-phase immiscible flow in porous media without considering gravity are:

- Capillary number: $Ca = (\eta_n u_n)/(\sigma_{nw} \cos\theta)$, which represents the ratio of viscous forces to capillary forces experienced by a nonwetting fluid during displacement. Herein, η_n and u_n are the viscosity and velocity of the advancing nonwetting fluid (subscript n), σ_{nw} is the interfacial tension between the wetting (subscript w) and nonwetting fluid. Concerning the practice in the field of subsurface multiphase flow, the Ca is usually less than 10^{-6} where the capillary force is playing a dominant role.
- Ratio of the dynamic viscosities: e.g. $\lambda = \eta_n/\eta_w$.
- Contact angle: θ is the fluid-fluid contact angle with the solid surface. The contact angle changes the geometric shape of the interface and can impact the development of dynamic process.

To improve the numerical stability of the LB simulation, a multiple-relaxation-time (MRT) LB model is adopted, which is more stable than the BGK LB model. In addition, a more accurate treatment of boundary conditions at solid-fluid interfaces (see Section 2.5.2.2) is incorporated for further improvement of numerical accuracy of the contact angle.

The aim of this research is to advance the fundamental understanding of a) two immiscible phase flow in a complex two-dimensional (2D) porous media through a systematic investigation of the interfacial tension, contact angle and viscosity ratio and b) countercurrent imbibition process in a fracture-matrix system using lattice Boltzmann (LB) modelling.

The implementation of the algorithm are based on the framework inherited from Professor Haihu Liu with the wetting boundary condition and Message passing interface available(Website: http://gr.xjtu.edu.cn/web/haihu.liu). The capability of reading binary data for complex porous geometry and the inlet and outlet boundary conditions

are modified by the author.

1.3 Thesis outline

In Chapter 2, the lattice Boltzmann method (LBM) will be first reviewed, and a couple of commonly used boundary conditions are emphasized. Then four main multiphase multicomponent lattice Boltzmann (LB) models will be briefly introduced and we explain the reason why the colour gradient model is implemented instead of other LB models. Also, the algorithm of the colour gradient model will be described in detail, focusing on the comparison study of two way of imposing the interfacial tension (perturbation step). Finally, two representative approach of implementing the wetting boundary condition will be discussed, with a distinct advantage shown for the 'direct approach' over the 'standard approach' in terms of computational accuracy for wetting phenomena on a flat surface. Meanwhile, for the curved boundaries as we will encounter in the modelling of realistic porous geometry, the algorithm proposed by Xu et al. [69] will be introduced in detail.

Chapter 3 will first describe the properties of porous media, along with the three scales involved in the oil and gas extraction. Especially, the definition of the representative volumes, porosity and saturation of the media will be given. Important processes such as imbibition, drainage are introduced. This chapter will conclude with the extended Darcy's law for two phases, the concept of relative permeability and the theoretical relationship between the capillary pressure P_c, effective saturation S_e and the relative permeability K_{rw} (K_{rnw}).

Chapter 4 provides a systematic investigation of the colour gradient two-phase LBM for simulating the oil and water dynamics within a realistic 2D porous geometry. The implementation will be extensively validated by the benchmark cases including capillary filling for the moving contact line, and cocurrent flow in a 2D channel for the relative permeability validation. The effect of the viscosity ratio, interfacial tension, and contact angle on the fluid distributions will be unravelled.

Chapter 5 deals with spontaneous imbibition, a key oil recovery mechanism in the fractured reservoir rocks. A 2D pore-scale computational study will be performed to understand the water imbibition into an artificially generated porous matrix with a fracture attached on top using a recently improved lattice Boltzmann colour gradient model. Several factors affecting the dynamic imbibition processes and oil recovery will be analyzed, including the water injection velocity, the geometry configuration of the

dual permeability zones, interfacial tension, viscosity ratio of water to oil phases, and fracture spacing if there are multiple fractures. Three distinctively different imbibition regimes will be identified, each with a special morphology in the fracture.

Chapter 6 will conclude this thesis with summary and discussions for future research.

1.4 Contributions of the thesis

In this thesis, the two generic recovery processes in oil reservoirs (**waterflooding** and **spontaneous imbibition**) have been investigated with the state-of-the-art lattice Boltzmann colour-gradient method, in order to deepen the understanding of the pore scale dynamics of immiscible two-phase transport mechanism within the porous and fractured media.

Waterflooding

- By investigating the dynamic displacement of immiscible fluids through waterflooding in a complex flow structure extracted from a realistic Berea sandstone sample, the colour gradient LBM has been shown as a reliable tool for numerical modelling of complex geometry.

- The numerical resolution of the computed geometry is higher than in previous studies.

- The effects of the viscosity ratio, interfacial tension and contact angle on the displacement process have been thoroughly studied. Through invasion of the wetting phase into the porous matrix, it is observed that the viscosity ratio plays an important role in the nonwetting phase recovery. At the viscosity ratio (λ) of unity, the saturation of the wetting fluid is highest, and it linearly increases with time. The displacing fluid saturation reduces drastically when λ increases to 20; however, when λ is beyond 20, the reduction becomes less significant for both imbibition and drainage. The front of the bottom fingers is finally halted at a position near the inlet as the viscosity ratio increases to 10. Increasing the interfacial tension generally results in higher saturation of the wetting fluid. Finally, the contact angle is found to have a limited effect on the efficiency of displacement in the 2D Berea sandstone.

Spontaneous imbibition

- Unlike many previous works which were done based on simple circular or square

cylinders of the solid grains in the matrix, the studied matrix is constructed using a Voronoi tessellation technique where the pore structure is modeled as randomly connected throats. The throat widths obey a log-normal distribution, which often serves as a good geometric approximation to natural porous media in statistics.

- By changing the water injection velocity and interfacial tension, three distinct imbibition regimes are identified for the first time, and they are the squeezing, jetting and dripping regimes, characterized with distinctively different morphologies of expelled oil in the fracture.

- In the dripping regime, a linear relationship between the oil recovery factor and the square root of time is observed, consistent with the available experimental finding. The effect of the geometry configuration of the dual permeability zones is explored and it is interestingly found that the build-up of the squeezing pressure upstream is able to facilitate water into the permeability zone closer to the fracture inlet thus increasing the oil recovery factor.

- Increasing water-to-oil viscosity ratio leads to a higher water imbibition rate and the highest oil recovery factor is achieved at the viscosity ratio of 0.5. In addition, introducing a second horizontal fracture is shown to significantly enhance oil recovery factor, and the fracture spacing that maximizes oil recovery is found. These findings can provide valuable information for the optimal design of water-injecting oil extraction in fractured rocks in reservoirs like oil-bearing shale or tight sandstone.

Chapter 2

Lattice Boltzmann Models

Theoretically, the motion of a fluid can be described by three types of mathematical models according to the observed scales. They are microscopic models at the molecular scale, the mesoscopic scale models including gas kinetic theories and continuum models at the macroscopic scale [76]. However, there are problems which can not be well described by any of these methods. For example, for fluid flows in porous media, it is very difficult to deal with the complex boundaries when solving the Navier-Stokes equations (NSEs), due to the pore size, orientation and their extremely complicated distribution. The lattice Boltzmann method (LBM) used in this thesis is based on mesoscopic kinetic equations, which can mimick molecular-scale interactions and describe macroscopic flow dynamics.

In this *Chapter*, the concept of the lattice Boltzmann method and its multiphase extensions will be introduced.

2.1 From Boltzmann equation to lattice Boltzmann method

Historically, the lattice Boltzmann method is derived from the lattice gas automata (LGA) method proposed in the 1970s. LGA is constructed as simple particle dynamics represented by boolean variables in the discretised space and time. The lattice Boltzmann method replaces the boolean variables of LGA with the discretised probability distribution function f which eliminates the need for ensemble averaging. Later it was shown that lattice Boltzmann equation (LBE) could also be derived from the Boltzmann equation. From this point of view, LBE is a mesoscopic numerical method.

The Boltzmann equation describes the evolution of non-equilibrium distribution function from statistical mechanics point of view, the cornerstone of gas kinetic theory. For

single component gases, we take f as the single-particle distribution function, which describes the probability of having a particle at time t at position $\boldsymbol{r}(x, y, z)$ with velocity $\boldsymbol{\xi}(\xi_x, \xi_y, \xi_z)$. The nonlinear, integral-differential Boltzmann equation can be defined as

$$\frac{\partial f}{\partial t} + \boldsymbol{\xi} \cdot \frac{\partial f}{\partial \boldsymbol{r}} + \boldsymbol{a} \cdot \frac{\partial f}{\partial \boldsymbol{\xi}} = J, \tag{2.1}$$

where $\boldsymbol{a}$ is the acceleration caused by body force $\boldsymbol{F}$ (either external or internal forces, such as gravity or intermolecular interactions) with $\boldsymbol{F} = \rho \boldsymbol{a}$, the right-hand side (RHS) J stands for the multi-dimensional integral collision term which leads to extreme difficulties in solution of the Boltzmann equation. To simplify this, the popular Bhatnagar-Gross-Krook (BGK) collision operator [77] was used to replace the collision term J in Eq. (2.1). Then the BGK-approximation Boltzmann equation is written as

$$\frac{\partial f}{\partial t} + \boldsymbol{\xi} \cdot \frac{\partial f}{\partial \boldsymbol{r}} + \boldsymbol{a} \cdot \frac{\partial f}{\partial \boldsymbol{\xi}} = -\frac{1}{\tau_c} \left[f - f^{(eq)} \right], \tag{2.2}$$

where τ_c is relaxation time, $f^{(eq)}$ is the Maxwellian distribution function

$$f^{(eq)} = \frac{\rho}{(2\pi RT)^{D/2}} \exp\left(-\frac{C^2}{2RT} \right), \tag{2.3}$$

where D is the dimensionality, $c_s = \sqrt{RT}$ is known as the speed of sound at temperature T, $R = k_B/m$ is the gas constant with k_B is the Boltzmann constant and m the molecular mass. $\boldsymbol{C}$ is the particular velocity defined by $\boldsymbol{C} = \boldsymbol{\xi} - \boldsymbol{u}$ where $\boldsymbol{\xi}$ symbolises the particle velocity and $\boldsymbol{u}$ the macroscopic fluid velocity. For simplicity, here we consider the single phase without external forces. The macroscopic density and velocity are defined as

$$\rho = \int f d\boldsymbol{\xi}, \ \rho \boldsymbol{u} = \int \boldsymbol{\xi} f d\boldsymbol{\xi}. \tag{2.4}$$

The first step is to discretise the velocity space of $\boldsymbol{\xi}$ into a finite set of velocities $\boldsymbol{c}_i$ without affecting the conservation laws. To do so, $f^{(eq)}$ is first expanded into a second-order Taylor series in terms of a very small fluid velocity $\boldsymbol{u}$

$$\begin{aligned} f^{(eq)} &= \frac{\rho}{(2\pi RT)^{D/2}} \exp\left(-\frac{\boldsymbol{\xi}^2}{2RT} + \frac{\boldsymbol{\xi}\boldsymbol{u}}{RT} - \frac{\boldsymbol{u}^2}{2RT} \right) \\ &= \exp\left(-\frac{\boldsymbol{\xi}^2}{2RT} \right) \frac{\rho}{(2\pi RT)^{D/2}} \exp\left(\frac{\boldsymbol{\xi}\boldsymbol{u}}{RT} - \frac{\boldsymbol{u}^2}{2RT} \right) \\ &= \frac{\rho}{(2\pi RT)^{D/2}} \exp\left(-\frac{\boldsymbol{\xi}^2}{2RT} \right) \left[1 + \frac{\boldsymbol{\xi} \cdot \boldsymbol{u}}{RT} + \frac{(\boldsymbol{\xi} \cdot \boldsymbol{u})^2}{2RT^2} - \frac{\boldsymbol{u}^2}{2RT} \right] + \mathcal{O}(\boldsymbol{u}^3). \end{aligned} \tag{2.5}$$

In order to obtain the correct Navier-Stokes equations in the limit of low Mach number,

i.e. $|\boldsymbol{u}|/\sqrt{RT} \ll 1$, the discrete velocity set should be chosen so that the following quadratures of the expanded equilibrium distribution function (EDF) hold exactly

$$\int \boldsymbol{\xi}^k f^{(eq)} d\boldsymbol{\xi} = \sum_i \omega_i \boldsymbol{c}_i^k f^{(eq)}(\boldsymbol{c}_i), 0 \leq k \leq 3, \tag{2.6}$$

where ω_i and $\boldsymbol{c}_i$ are the weights and integral points of the numerical quadrature rule. Based on the formulation of the expanded EDF given by Eq. (2.5), it is natural to choose a Gaussian quadrature. For the purpose of accuracy, at least fifth-order Gaussian quadrature should be chosen as can be seen from Eq. (2.6). In this way, the weights and integral points (i.e. discrete velocities) with different integral accuracy can be defined. And here we introduce a new distribution function $f_i(\boldsymbol{x}, t) = \omega_i f(\boldsymbol{x}, \boldsymbol{c}_i, t)$. Its evolution equation

$$\frac{\partial f_i}{\partial t} + \boldsymbol{c}_i \cdot \frac{\partial f_i}{\partial \boldsymbol{r}} = -\frac{1}{\tau_c}\left[f_i - f_i^{(eq)}\right], \tag{2.7}$$

where $f_i^{(eq)}(\boldsymbol{x}, t) = \omega_i f_i^{(eq)}(\boldsymbol{x}, \boldsymbol{c}_i, t)$. For this equation, the time and space are all continous except the velocity is discretised. Thus it is also called Discrete Velocity Boltzmann equation (DVBE). Accordingly, the macroscopic velocity and velocity can be defined as

$$\rho = \sum_i f_i, \ \rho \boldsymbol{u} = \sum_i \boldsymbol{c}_i f_i. \tag{2.8}$$

Now if we integrate Eq. (2.7) from t to $t + \delta_t$ along the characteristic line and assume that the collision term is constant during this interval, we can get

$$f_i(\boldsymbol{x} + \boldsymbol{c}_i\delta_t, t + \delta_t) - f_i(\boldsymbol{x}, t) = -\frac{1}{\tau}\left[f_i(\boldsymbol{x}, t) - f_i^{(eq)}(\boldsymbol{x}, t)\right], \tag{2.9}$$

where $\tau = \tau_c/\delta_t$ is the dimensionless relaxation time. This is the LBGK model. As a first-order finite-difference scheme for the discrete velocity Boltzmann eqation (2.7), the accuracy in terms of time and space are both fisrt order in Eq. (2.9). However, if the numerical viscosity is incorporated into the physical viscosity, the LBGK model will be second-order accurate in time and space. In addition, the discretization of time and space are not independent, instead related by the discretized velocity of particles, for example, $\delta_x = c_i\delta_t$. This feature enables us to divide the motion of particles into two relative process, streaming and collision in the physical space. In detail, the particle moves to its neighbouring node from the current node between two time steps and collides with other particles while streaming to the neighbouring node. This equips the lattice Boltzmann method with good capability of parallel computing and quite good adaptivity with complex boundary conditions.

2.2 Single-phase LBGK models

The LBGK models are the most widely used (LBE) model[1] and have been widely applied for a variety of complex flows. Among those available models, the most representative ones are those proposed by Qian et al. [78], i.e. the group of $DnQb$ (n-dimensional b-velocity) models. In the $DnQb$ model, the discrete EDF is written as

$$f_i^{(eq)} = \omega_i \rho \left[1 + \frac{\boldsymbol{c}_i \cdot \boldsymbol{u}}{c_s^2} + \frac{(\boldsymbol{c}_i \cdot \boldsymbol{u})^2}{2c_s^4} - \frac{u^2}{2c_s^2} \right], \tag{2.10}$$

where ω_i is the weight coefficient associated with the discrete velocity $\boldsymbol{c}_i$, and the sound speed $\boldsymbol{c}_s$ (a model constant that indicates the speed of information propagation in the LBE model) is model dependent as it is determined by the Hermite quadratures [79]. As we are dealing with nearly incompressible flow, the physical speed of sound is not important as long as the Mach number is small enough (e.g. $Ma < 0.3$). Also the speed of sound in the LBE indicates it is a method of artificial compressibility. Two popular $DnQb$ models $D2Q9$ and $D3Q19$ are presented in Table 2.1[2]. In these two models, the relationship between the lattice speed and the lattice sound speed is written as $c_s = c/\sqrt{3}$. For the $DnQb$ model, it is easy to validate that the discrete EDF f_i^{eq}has

Table 2.1: Parameters of two $DnQb$ models

Model	Lattice vector $\boldsymbol{c}_i$	Weight ω_i	c_s^2
$D2Q9$	c(0,0), c$(\pm1, 0)$,c$(0, \pm1)$, c$(\pm1, \pm1)$	4/9, 1/9, 1/36	$1/3c^2$
$D3Q19$	c(0,0,0), c$(\pm1, 0, 0)$,c$(0, \pm1, 0)$,c$(0, 0, \pm1)$ c$(\pm1, \pm1, 0)$,c$(\pm1, 0, \pm1)$,c$(0, \pm1, \pm1)$	1/3, 1/18, 1/36	$1/3c^2$

the following characteristics

$$\begin{aligned} &\sum_i f_i^{eq} = \rho,\ \sum_i \boldsymbol{c}_i f_i^{eq} = \rho \boldsymbol{u},\ \sum_i \boldsymbol{c}_i \boldsymbol{c}_i f_i^{eq} = \rho \boldsymbol{u}\boldsymbol{u} + p\boldsymbol{I}, \\ &\sum_i \boldsymbol{c}_{i\alpha} \boldsymbol{c}_{i\beta} \boldsymbol{c}_{i\gamma} f_i^{eq} = c_s^2 \rho [u\delta]_{\alpha\beta\gamma} = c_s^2 \rho (u_\alpha \delta_{\gamma\beta} + u_\beta \delta_{\gamma\alpha} + u_\gamma \delta_{\alpha\beta}), \end{aligned} \tag{2.11}$$

where $p = c_s^2 \rho$, these relations are necessary for the derivation of the correct hydrodynamic equations given in Appendix A.

Considering the presence of a body force (when the forcing term $\boldsymbol{a} \cdot \partial f / \partial \boldsymbol{\xi}$ can not be

[1] These model discussed here are all for isothermal flows unless otherwise stated

[2] Here the lattice speed c is taken as 1

neglected), the most straightforward approach is to add a forcing term to Eqn. 2.9,

$$f_i(\boldsymbol{x} + \boldsymbol{c}_i\delta_t, t + \delta_t) - f_i(\boldsymbol{x}, t) = -\frac{1}{\tau}\left[f_i(\boldsymbol{x}, t) - f_i^{(eq)}(\boldsymbol{x}, t)\right] + \delta_t F_i, \tag{2.12}$$

where F_i depends on the body force $\boldsymbol{F}$, given by the modified moment-expansion scheme [80, 81]

$$F_i = (1 - \frac{1}{2\tau})\omega_i\left[\frac{\boldsymbol{c}_i - \boldsymbol{u}}{c_s^2} + \frac{(\boldsymbol{c}_i \cdot \boldsymbol{u})\boldsymbol{c}_i}{c_s^4}\right] \cdot \boldsymbol{F}. \tag{2.13}$$

And the fluid velocity is corrected as the average of the velocity before and after the collision, given as

$$\rho\boldsymbol{u} = \sum_i \boldsymbol{c}_i f_i + \frac{1}{2}\boldsymbol{F}\delta_t. \tag{2.14}$$

2.3 Boundary conditions

Boundary conditions are to prescribe adequate values for those populations propagating from the solid object into the fluid region. They play an important role in fluid dynamics since they are essential in the determination of the solution of the flow. For the LBM, the mesoscopic populations on the boundary have to be constructed to reflect specific boundary conditions for fluid variables (e.g. pressure, velocity, or temperature) during each time step. This may take place either within the collision process or the propagation stage. Because of the fact that the system of mesoscopic variables have more degrees of freedom than the corresponding macroscopic system, a variety of boundary schemes have been introduced for LBM.

2.3.1 Bounce-back Scheme

First of all, the most widely-used rule for stationary no-slip walls is the bounce-back scheme. The bounce-back scheme includes two different strategies, i.e. *standard bounce-back* and *halfway bounce-back*. The standard bounce-back places the wall on the lattice nodes, while the halfway bounce-back places the wall at the middle of the lattice link. Figure 2.1 (a) and (b) illustrate the sketch for both the standard bounce-back and halfway bounce-back boundary condition.

The standard bounce-back is advantageous for its simplicity and capability of dealing with complex boundaries. This scheme assumes that a particle just reverses its velocity after colliding with the wall, which means that the post-collision distribution function

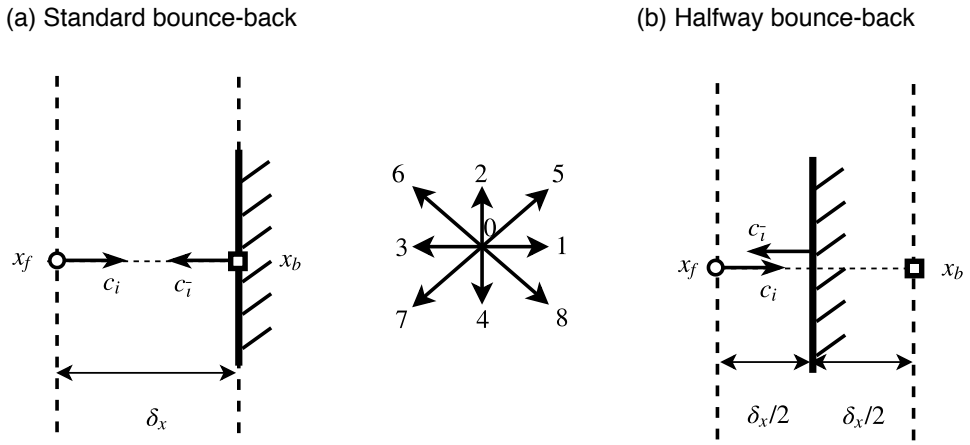

Figure 2.1: Sketch for (**a**) standard bounce-back and (**b**) halfway bounce-back boundary condition

at a boundary node $\boldsymbol{x}_b$ is

$$f_{\bar{i}}^{'}(\boldsymbol{x}_b, t) = f_i^{'}(\boldsymbol{x}_f, t), \tag{2.15}$$

where $\boldsymbol{c}_{\bar{i}}$ points to the fluid and denotes the opposite direction of $\boldsymbol{c}_i$, $\boldsymbol{x}_f$ is the boundary fluid node and $\boldsymbol{x}_b$ is the wall node neighbouring to the fluid node. Consider the collision-streaming process, it can also be written in the following formulation without the wall node

$$f_{\bar{i}}(\boldsymbol{x}_f, t + \delta_t) = f_i^{'}(\boldsymbol{x}_f, t). \tag{2.16}$$

This formation is extremely useful since the computation is completely local. Note that the collision process is not carried out on the boundary nodes for the standard bounce-back. Equation (2.16) is also used for the halfway bounce-back except for the different location of the wall. The halfway bounce-back scheme is very straightforward to understand from a physical point of view: The post-collision particles with velocity $\boldsymbol{c}_i$ at node $\boldsymbol{x}_f$ will arrive at the wall after time $\delta_t/2$, and are then reflected back to $\boldsymbol{x}_f$ with a reversed velocity $\boldsymbol{c}_{\bar{i}}$ after another $\delta_t/2$, and so $f_{\bar{i}}(\boldsymbol{x}_f, t + \delta_t) = f_i^{'}(\boldsymbol{x}_f, t)$, which is the same as the standard bounce-back scheme.

The standard bounce-back condition is shown to be first-order in accuracy, while the conventional LBM has the second order of accuracy in space inside of the flow domain [78]. Inamuro [82] showed that when the relaxation time is chosen in the range $(0.7, 2)$, the error of the single relaxation time LBM with the standard bounce-back condition is sufficiently small and of second order, so that the standard bounce-back can be used without degrading the entire simulation accuracy. For the multiple relaxation time (MRT) LBM, the standard bounce-back is always of second order and not

dependent on the selection of relaxation parameters [83]. The halfway bounce-back scheme is of second-order accuracy [84] and it will be implemented in the following chapters.

2.3.2 Periodic Boundary Condition

The periodic boundary condition may be the simplest LBM boundary condition. It applies only to the situations where the flow solution is periodic. In less physically oriented occasions, it can also be used to solve 2D flow problems with an existing 3D code by adopting the periodic flow condition along one of the Cartesian axis. In the periodic system, the fluid leaving the domain on one side will re-enter from the opposite side of the domain thus the mass and momentum are always conserved. Figure 2.2 illustrates periodic boundary condition for the 2D flow problem.

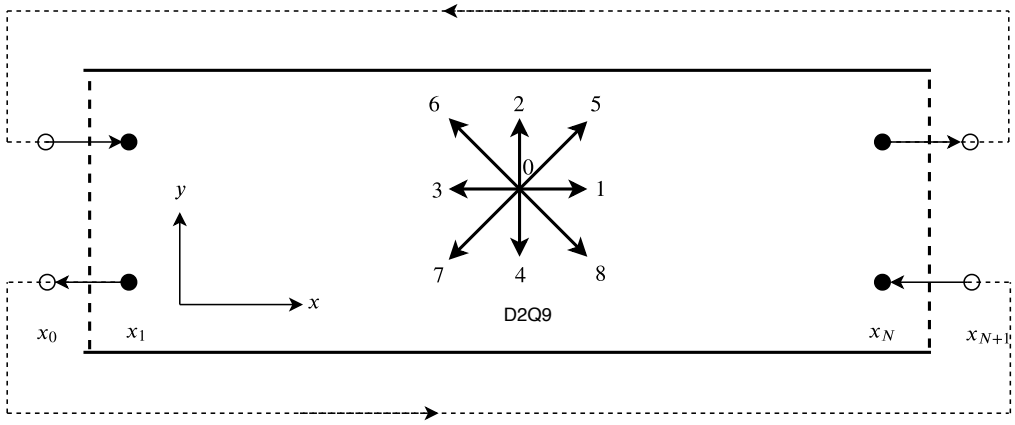

Figure 2.2: Periodic boundary condition with two layers of ghost nodes added at $x_0 = x_1 - \delta_x$ and $x_{N+1} = x_N + \delta_x$. The solid circle denotes fluid node and the open circle represents the added ghost nodes.

Assuming that $\boldsymbol{L}$ represents the periodic direction and length of the computational domain, the unknown incoming populations f_i on one side are given by those leaving the domain at the opposite side during propagation (taking the x direction as an example):

$$f_i'(\boldsymbol{x}, t) = f_i'(\boldsymbol{x} + \boldsymbol{L}, t), \tag{2.17a}$$

$$f_{\bar{i}}'(\boldsymbol{x} + L, t) = f_{\bar{i}}'(\boldsymbol{x}, t), \tag{2.17b}$$

where $i = 1, 5, 8$. Alternatively, it can be considered that the edges of the simulation domain are attached together without ghost nodes. In this way, the periodic boundary

conditions are implemented through a completion step in the streaming process. It can be formulated as:

$$f_i(x_1, y, t + \delta_t) = f_i^{'}(x_{N+1}, y - c_{iy}\delta_t, t), \quad i = 1, 5, 8, \tag{2.18a}$$

$$f_i(x_N, y, t + \delta_t) = f_i^{'}(x_0, y - c_{iy}\delta_t, t), \quad i = 3, 6, 7. \tag{2.18b}$$

2.3.3 Periodic Boundary Condition with Pressure Gradient

Although the periodic condition is exact in flows without mean pressure gradient, it is not generally valid in the presence of the pressure gradient [85]. It is a widely used approach to simulate pressure driven flow with an effective body force to replace the pressure gradient. However, the body force approach is argued to perform well only for a flow with a constant cross section-area such as Poiseuille flow, and the validity of the body force approach has not been fully evaluated for flows in complex geometries, e.g. flows in corrugated channels or porous media. Moreover, numerical errors can be accumulated since the currently available wall boundary conditions usually do not consider the body force effects on the wall.

To overcome the limitation mentioned above, the incompressible lattice Boltzmann [86, 87] with the generalized periodic boundary condition (GPBC) may be used since its accuracy is not diminished by the boundary closure as in the conventional periodic boundary closure. In pressure driven incompressible flows, the generalized periodic conditions of the flow are:

$$p(\boldsymbol{x}, t) = p(\boldsymbol{x} + \boldsymbol{L}, t) + \Delta p, \tag{2.19a}$$

$$\boldsymbol{u}(\boldsymbol{x}, t) = \boldsymbol{u}(\boldsymbol{x} + \boldsymbol{L}, t). \tag{2.19b}$$

where Δp denotes a prescribed pressure drop. A simple and robust procedure of GPBC developed for LBM proposed by Kim and Pitsch [85] will be discussed here (here we consider the presence of two layers of virtual nodes at the inlet and outlet). The equilibrium distributions and the nonequilibrium distributions are specified separately, following Figure 2.2, for the equilibrium part, it is written as:

$$f_i^{eq}(x_0, y, t) = f_i^{eq}(p_{in}, \boldsymbol{u}_N), \tag{2.20a}$$

$$f_i^{eq}(x_{N+1}, y, t) = f_i^{eq}(p_{out}, \boldsymbol{u}_1), \tag{2.20b}$$

where $\boldsymbol{u}_N$ and $\boldsymbol{u}_1$ represents the velocity at nodes x_N and x_1, respectively. And p_{in} and p_{out} denote the pressure at the inlet and outlet, respectively. The non-equilibrium part is set to the same value as the nodes inside the real domain:

$$f_i^{neq}(x_0, y, t) = f_i^{neq}(x_N, y, t), \tag{2.21a}$$

$$f_i^{neq}(x_{N+1}, y, t) = f_i^{neq}(x_1, y, t), \tag{2.21b}$$

where the non-equilibrium populations at the nodes x_N and x_1 are acquired after collision, i.e., $f_i^{neq} = f_i^{'} - f_i^{eq}$. Then just before streaming, with the equilibrium and non-equilibrium part at the nodes x_0 and x_{N+1}, we have

$$f_i^{'}(x_0, y, t) = f_i^{eq}(p_{in}, \boldsymbol{u}_N) + \left[f_i^{'}(x_N, y, t) - f_i^{eq}(x_N, y, t)\right], \quad i = 1, 5, 8, \tag{2.22a}$$

$$f_i^{'}(x_{N+1}, y, t) = f_i^{eq}(p_{out}, \boldsymbol{u}_1) + \left[f_i^{'}(x_1, y, t) - f_i^{eq}(x_1, y, t)\right], \quad i = 3, 6, 7. \tag{2.22b}$$

2.3.4 Constant pressure or velocity boundary condition

Using the bounceback rule for the non-equilibrium part of the particle distribution, Zou and He [4] proposed a hydrodynamic scheme, which utilises the relation between the macroscopic fluid variables and the distribution functions, to realise the exact boundary condition.

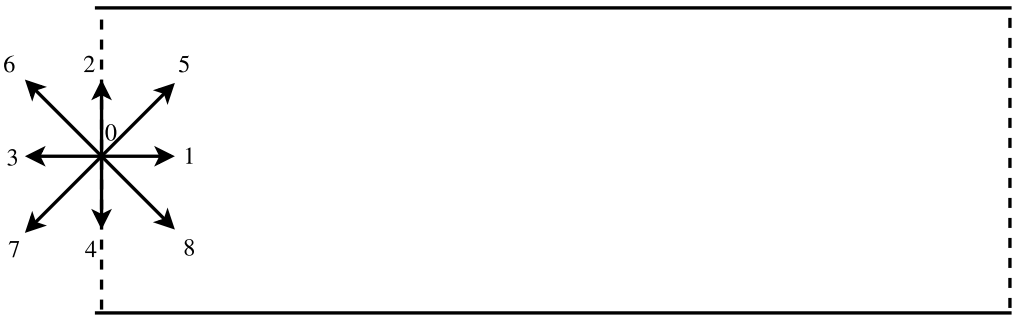

Figure 2.3: Pressure boundary schematic for the D2Q9 model[4] in a channel

For the constant pressure boundary condition, the inlet pressure $p_{in} = c_s^2 \rho_{in}$ is specified, and the inlet velocity $\boldsymbol{u}_{in} = (u_{in}, v_{in})$ is unknown. In this approach, it is also assumed

that v_{in} is zero. From Fig. 2.3, the following equations can be written as

$$f_1 + f_5 + f_8 = \rho_{in} - (f_0 + f_2 + f_3 + f_4 + f_6 + f_7), \tag{2.23a}$$

$$f_1 + f_5 + f_8 = \rho_{in} u_{in} + (f_3 + f_6 + f_7), \tag{2.23b}$$

$$f_5 - f_8 = -f_2 + f_4 - f_6 + f_7. \tag{2.23c}$$

The first two equations give

$$u_{in} = 1 - \frac{[f_0 + f_2 + f_4 + 2(f_3 + f_6 + f_7)]}{\rho_{in}}, \tag{2.24}$$

then the bounceback rule for the non-equilibrium part of the particle distribution which is normal to the inlet is applied,

$$f_1 - f_1^{(eq)} = f_3 - f_3^{(eq)}, \quad f_1 = f_3 + \frac{2}{3}\rho_{in} u_{in}. \tag{2.25}$$

Combining this relation with Eq. (2.23) (b) and (c), the remaining two distribution functions f_5 and f_8 are obtained,

$$f_5 = f_7 - \frac{1}{2}(f_2 - f_4) + \frac{1}{6}\rho_{in} u_{in}, \tag{2.26}$$

$$f_8 = f_6 + \frac{1}{2}(f_2 - f_4) + \frac{1}{6}\rho_{in} u_{in}. \tag{2.27}$$

Similarly, if the inlet velocity u_{in} is given as in the constant velocity boundary condition, the density can be obtained with

$$\rho_{in} = \frac{[f_0 + f_2 + f_4 + 2(f_3 + f_6 + f_7)]}{1 - u_{in}}, \tag{2.28}$$

The unknown distribution functions f_1, f_5 and f_8 are determined from Eq. (2.25), (2.26) and (2.27).

2.4 Multiphase lattice Boltzmann models

As a mesoscopic method, the lattice Boltzmann method (LBM) has been widely accepted as a useful alternative for simulating multiphase flows, in particular, with the advantage of dealing with complex geometries such as porous media [12]. A number of multiphase LBM models have been proposed, e.g., the colour gradient model [35, 88], the pseudo-potential model [89], the free energy model [90] and the mean-field model [91].

The colour gradient model developed by Gunstensen et al [35] is known to be the first multiphase model for simulating immiscible binary fluids. It is based on the two-component lattice gas model proposed by Rothman and Keller [88]. The colour gradient model incorporates the effect of interfacial tension by adding a perturbation operator to the original collision operator. A recolouring operator is used to limit the diffusion near the interface. This step guarantees the immiscibility of the two fluids. The model has high numerical accuracy, strict mass conservation for each fluid and numerical stability for a broad range of viscosity ratios. However, the limitation of this model lies in the limited density ratio, the medium spurious currents near the interfaces, and difficulty in considering thermodynamics of interfaces. While it should not be a problem as long as no major thermodynamical effects such as phase changes are concerned.

Later, a new multiphase LBM model was proposed by Shan and Chen [89], where the interparticle forces (whether attractive or repulsive) mimicking the molecular potentials are introduced by a modified equilibrium velocity in the equilibrium distribution functions. Its conceptual and computational simplicity has made Shan-Chen model a popular approach in the LB community. Recently, the limitations of the original Shan-Chen model have been alleviated and its performance is improved. These techniques include improving the forcing scheme [92, 93, 94] in order to achieve thermodynamic consistency and large density ratio. Through a higher-order analysis of a general forcing term, the scheme that is able to reproduce arbitrarily high density ratios independent of the surface tension is proposed by Lycett-Brown and Luo [95], and the interface width can also be varied independently of density ratio and surface tension. Most recently, based on a two-range pseudopotential lattice Boltzmann method, a scheme with tunable surface tension is proposed by Fei et al. [96].

The free energy model [90] is thermodynamically consistent, and it considers a generalised equilibrium distribution function that includes a non-ideal pressure tensor term. The BGK collision operator of the free energy model satisfies the local mass and momentum conservation. The original free energy model suffers from a lack of Galilean invariance in the vicinity of interfaces where large density gradient exists, which leads to some non-physical phenomenon. For example, it has been reported that a droplet or bubble that is initially spherical will become elliptical over time in a uniform flow field. Later works have mitigated this problem by modifying the equilibrium distribution function coefficients [97, 98]. However, with the free-energy model, the dissolution rate for small droplets/bubbles tends to be large.

The mean-field model was first developed by He, Shan and Doolen [91] for non-ideal gases (also known as HSD model). Later it is improved by He, Chen and Zhang [99]

for incompressible multiphase flows (also referred as HCZ model), which describes interfacial dynamics based on the mean-field theory [100], and uses a pressure distribution function instead of its density counterpart to 'capture' incompressible fluid's pressure and velocity fields. This approach greatly reduces the effect of discretization errors in the calculation of density gradient and improves the numerical stability for varied density. The HCZ model is a numerical-diffuse-interface approach which involves a numerical scheme to 'capture' the interface. Thus an index function is also used to track interfaces between different phases. The serious limitation of the mean-field theory model is its numerical instability, associated with the 'stiffness' of the collision operator, when the 'complex fluid' effects are introduced through the forcing term [101]. Extensive reviews of these LBM multiphase models are available in the literature, e.g. [24, 70, 71, 101].

In summary, each model has its own advantages and disadvantages. It is not possible to state that one model is definitely preferred to another, and the choice depends on the application of interest. In porous media applications, the flow is characterised by small capillary number, thus it is necessary to choose a suitable model with good numerical stability and small spurious currents at the interface. Among the models mentioned above, the pseudo-potential model produces the largest spurious velocities. And the small droplets/bubbles are expected to dissolve for the free-energy and mean-field model. Considering that the interfacial tension in the modelling can be given directly and the colour gradient model is most suitable to simulate flows with moderate/high viscosity ratio, we choose to use the colour gradient model in this thesis. Apart from the merits mentioned above, the colour gradient model produces relatively thin interface and is able to control the interfacial diffusion and adjust the interfacial tension and viscosity independently to facilitate the numerical investigation. Also, since we are dealing with completely immiscible fluids in this work, the colour gradient method is implemented.

2.5 Colour gradient lattice Boltzmann method

2.5.1 Numerical algorithm

The *multiphase colour gradient LBM* will be discussed in detail here which will be used in Chapters 4 and 5. In this model, the "Red" and "Blue" distribution functions (f_i^R and f_i^B) are used to represent two different fluids. The total distribution function is defined as $f_i = f_i^R + f_i^B$. Each coloured distribution function undergoes the collision

and streaming steps expressed by the following equation:

$$f_i^k(\boldsymbol{x} + \boldsymbol{c}_i\delta_t, t + \delta_t) = f_i^k(\boldsymbol{x}, t) + \Omega_i^k(f_i^k(\boldsymbol{x}, t)), \tag{2.29}$$

where $\boldsymbol{x}$ and t are the position and time, $k = R$ or B, i represents the discrete velocity directions for the two-dimensional 9-velocity (D2Q9) model, δ_t is the time step, and $\boldsymbol{c}_i$ denotes the lattice velocity vectors in the i-th discrete velocity direction. For the two-dimensional 9-velocity (D2Q9) model used in this work, the lattice velocity vector is given in Table 2.1.

The collision step includes self- and cross-interactions with the other type of particles which can be written as

$$\Omega_i^k = (\Omega_i^k)^{(3)} \left[(\Omega_i^k)^{(1)} + (\Omega_i^k)^{(2)} \right], \tag{2.30}$$

where $(\Omega_i^k)^{(1)}$ is the single-phase collision operator, $(\Omega_i^k)^{(2)}$ is the perturbation operator, and $(\Omega_i^k)^{(3)}$ is the recolouring operator.

2.5.1.1 Single-Phase Collision Operator

To achieve high accuracy and good stability, we implemented the collision step in accordance with the two-relaxation-time (TRT) model [102, 103, 104]—a special multiple relaxation time (MRT) model with only two relaxation rates [105]. With the TRT model, the single-phase collision operator is expressed as

$$(\Omega_i^k)^{(1)} = -(\boldsymbol{M}^{-1}\boldsymbol{S}\boldsymbol{M})_{ij}(f_j^k - f_j^{k,eq}), \tag{2.31}$$

where $\boldsymbol{M}$ is the transformation matrix and is given by

$$\boldsymbol{M} = \begin{pmatrix} 1 & 1 & 1 & 1 & 1 & 1 & 1 & 1 & 1 \\ -4 & -1 & -1 & -1 & -1 & 2 & 2 & 2 & 2 \\ 4 & -2 & -2 & -2 & -2 & 1 & 1 & 1 & 1 \\ 0 & 1 & 0 & -1 & 0 & 1 & -1 & -1 & 1 \\ 0 & -2 & 0 & 2 & 0 & 1 & -1 & -1 & 1 \\ 0 & 0 & 1 & 0 & -1 & 1 & 1 & -1 & -1 \\ 0 & 0 & -2 & 0 & 2 & 1 & 1 & -1 & -1 \\ 0 & 1 & -1 & 1 & -1 & 0 & 0 & 0 & 0 \\ 0 & 0 & 0 & 0 & 0 & 1 & -1 & 1 & -1 \end{pmatrix}. \tag{2.32}$$

The diagonal relaxation matrix $\boldsymbol{S}$ is defined as

$$\boldsymbol{S} = (1, s_e, s_\varepsilon, 1, s_q, 1, s_q, s_\nu, s_\nu). \tag{2.33}$$

For the conserved moments of density and momentum, the relaxation rates are set to 1. s_e and s_ν are related to the bulk and shear viscosities, and s_ε and s_q are free parameters. Following the recommendations of Ginzburg et al. [106], these relaxation rates are taken as

$$s_e = s_\varepsilon = s_\nu = \frac{1}{\tau}, \quad s_q = 8\frac{(2 - s_\nu)}{(8 - s_\nu)}, \tag{2.34}$$

where τ is the dimensionless relaxation time. It is noted that as $s_i = 1/\tau$, the MRT reduces to the LBGK models. The mass conservation for each fluid distribution function and the total momentum conservation require

$$\rho_k = \sum_i f_i^k = \sum_i f_i^{k,eq}, \quad \rho\boldsymbol{u} = \sum_i \sum_k f_i^k \boldsymbol{c}_i = \sum_i \sum_k f_i^{k,eq} \boldsymbol{c}_i, \tag{2.35}$$

where ρ is the total density, and ρ_k is the density of fluid k, and $\boldsymbol{u}$ is the local fluid velocity.

The equilibrium distribution function ($f_i^{k,eq}(\boldsymbol{x}, t)$) is a truncated Taylor series expansion up to the second order in Mach number of the Maxwell–Boltzmann equilibrium distribution function, which is chosen to satisfy Equation (2.35):

$$f_i^{k,eq}(\rho_k, \boldsymbol{u}) = \rho_k W_i \left[1 + \frac{\boldsymbol{c}_i \cdot \boldsymbol{u}}{c_s^2} + \frac{(\boldsymbol{c}_i \cdot \boldsymbol{u})^2}{2c_s^4} - \frac{\boldsymbol{u}^2}{2c_s^2}\right], \tag{2.36}$$

in which, $c_s = 1/\sqrt{3}$ is the lattice sound speed, and the weight coefficients are $W_0 = 4/9$, $W_{1-4} = 1/9$ and $W_{5-8} = 1/36$ for the D2Q9 lattice model. As we focused on the oil-water two-phase systems, the density ratio of both fluids is set to be unity. (The density of petroleum is approximately 800 kg/m^3 [107], and 1000 kg/m^3 for water.)

To ensure a constant viscosity across the interface when both fluids are of different viscosities, the following harmonic mean [108] is employed to determine the viscosity of the fluid mixture:

$$\frac{1}{\eta} = \frac{1 + \rho^N}{2\eta_R} + \frac{1 - \rho^N}{2\eta_B}, \tag{2.37}$$

where η_k is the dynamic viscosity of fluid k, and η is the dynamic viscosity of the fluid mixture which is related to the dimensionless relaxation time τ by $\eta = c_s^2\rho(\tau - 0.5)\delta_t$;

ρ^N is the indicator function used to distinguish different fluids, and it is defined as

$$\rho^N(\boldsymbol{x},t) = \frac{\rho_R(\boldsymbol{x},t) - \rho_B(\boldsymbol{x},t)}{\rho_R(\boldsymbol{x},t) + \rho_B(\boldsymbol{x},t)}, \quad -1 \leq \rho^N \leq 1, \tag{2.38}$$

where ρ_R and ρ_B are the local densities of the red and blue fluids, respectively. They can be understood as the volume fraction of red and blue fluids, respectively. At a lattice node within the bulk phase, if ρ_R equals to 1, ρ_B will be zero. And the vice versa. With this definition, $\rho^N = 1$ and -1 represent the red fluid and the blue fluid, respectively, and $-1 < \rho^N < 1$ represents the diffuse interface where the mixture of red and blue fluids coexist.

2.5.1.2 Perturbation Operator

The second collision term $(\Omega_i^k)^{(2)}$ takes effect in the mixed interfacial region to generate an interfacial tension. Gunstensen et al. first introduced the perturbation operator with a 2D hexagonal lattice, it is given as [35, 109]

$$(\Omega_i^k)^{(2)} = \frac{A_k}{2}|\boldsymbol{G}|\left[\frac{(\boldsymbol{c}_i \cdot \boldsymbol{G})^2}{|\boldsymbol{G}|^2} - \frac{1}{2}\right], \tag{2.39}$$

where A_k is a free parameter which controls the interfacial tension, and $\boldsymbol{G}$ is the local colour gradient which is defined by $\boldsymbol{G}(x,t) = \sum_i [\rho_R(x + \boldsymbol{c}_i, t) - \rho_B(x + \boldsymbol{c}_i, t)]\boldsymbol{c}_i$. However, according to the study of Reis and Phillips [110], a direct extension of the above perturbation operator to the popular D2Q9 lattice would give

$$(\Omega_i^k)^{(2)} = \frac{A_k}{2}|\boldsymbol{G}|\left[\frac{(\boldsymbol{c}_i \cdot \boldsymbol{G})^2}{|\boldsymbol{G}|^2} - \frac{3}{4}\right], \tag{2.40}$$

which cannot recover the correct Navier-Stokes equations for two-phase flows. Further, they proposed that the correct collision operator should be

$$(\Omega_i^k)^{(2)} = \frac{A_k}{2}|\boldsymbol{G}|\left[W_i\frac{(\boldsymbol{c}_i \cdot \boldsymbol{G})^2}{|\boldsymbol{G}|^2} - B_i\right], \tag{2.41}$$

where $B_0 = -\frac{4}{27}$, $B_{1-4} = \frac{2}{27}$ and $B_{5-8} = \frac{5}{108}$. Using these parameters, the perturbation operator can recover the correct interfacial force term, i.e., the divergence of stress tensor, in the NSEs. This approach is later referred as 'Reis model'.

Another approach (later referred as 'CSF model') to apply the perturbation step is to add a direct forcing term at the interfacial region to recover the macroscopic effects of surface tension proposed by Lishchuk [111]. In this approach, Using the continuum

surface force (CSF) [112] model, a body force term is added to the macroscopic momentum equation, and it is calculated explicitly through the interfacial normal and macroscopic curvature

$$\boldsymbol{F}_s = \frac{1}{2}\sigma K \boldsymbol{\nabla}\rho^N, \tag{2.42}$$

where σ is the interfacial tension coefficient, and K is the local interface curvature calculated by [112]

$$K = -\boldsymbol{\nabla}_s \cdot \boldsymbol{n}, \tag{2.43}$$

where $\nabla_s = (\boldsymbol{I} - \boldsymbol{nn}) \cdot \boldsymbol{\nabla}$ is the surface gradient operator, $\boldsymbol{I}$ is the second-order identity tensor, and $\boldsymbol{n} = \boldsymbol{\nabla}\rho^N / \left|\boldsymbol{\nabla}\rho^N\right|$ is a unit vector normal to the interface. In 2D simulations, the interface curvature can be further written as

$$K = n_x n_y(\partial_x n_y + \partial_y n_x) - n_y^2 \partial_x n_x - n_x^2 \partial_y n_y. \tag{2.44}$$

A body force is then incorporated into LBM through the forcing scheme proposed by Guo et al. [81] which can significantly improve computation accuracy and reduce spurious velocities effectively [113]. The perturbation operator $(\Omega_i^k)^{(2)}$ is expressed as

$$(\Omega_i^k)^{(2)} = \boldsymbol{M}^{-1}\left(\boldsymbol{I} - \frac{1}{2}\boldsymbol{S}\right)\boldsymbol{F}^k, \tag{2.45}$$

with

$$\begin{aligned}\boldsymbol{F}^k(\boldsymbol{x},t) = \alpha_k[0,\ & 6(u_x F_{sx} + u_y F_{sy}),\\ & -6(u_x F_{sx} + u_y F_{sy}),\ F_{sx},\ -F_{sx},\ F_{sy},\ -F_{sy},\\ & 2(u_x F_{sx} - u_y F_{sy}),\ u_x F_{sy} + u_y F_{sx}]^T,\end{aligned} \tag{2.46}$$

where α_k is the fraction of interfacial tension contributed by fluid k and satisfies $\sum_k \alpha_k = 1$.

For single-relaxation collision operator, the perturbation operator $(\Omega_i^k)^{(2)}$ reduces to

$$(\Omega_i^k)^{(2)} = \alpha_k\left(1 - \frac{1}{2\tau_k}\right)W_i\left[\frac{\boldsymbol{c}_i - \boldsymbol{u}}{c_s^2} + \frac{\boldsymbol{c}_i \cdot \boldsymbol{u}}{c_s^4}\boldsymbol{c}_i\right] \cdot \boldsymbol{F}_s. \tag{2.47}$$

The fluid velocity is corrected to recover the Navier–Stokes (N-S) equations in the interfacial region where the two fluids coexist

$$\rho\boldsymbol{u} = \sum_i \sum_k f_i^k \boldsymbol{c}_i + \frac{1}{2}\boldsymbol{F}_s. \tag{2.48}$$

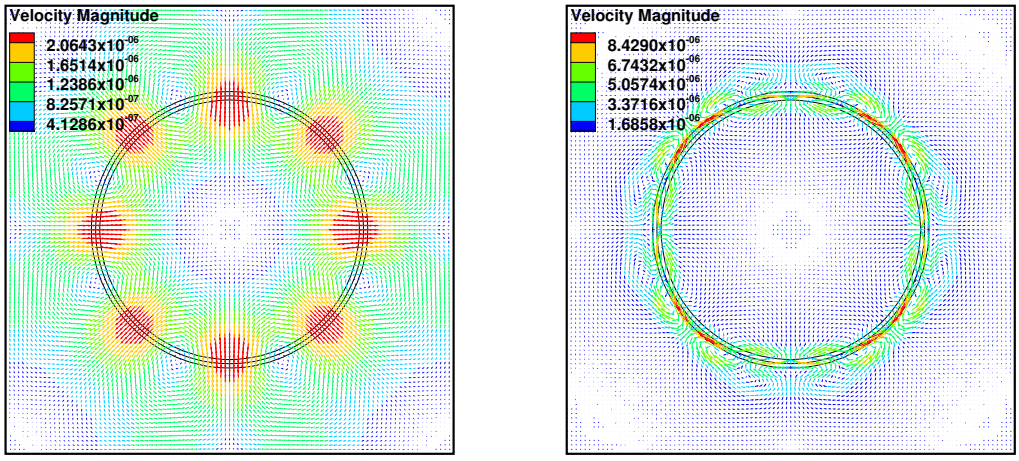

(a) (b)

Figure 2.4: Equilibrium droplet shape and velocity field for $\nu_R = \nu_B = 0.33$ at $\sigma = 0.001$ for (a)'CSF model' and (b)'Reis model'.

In order to compare the two way of imposing the interfacial tension, a comparison study has been done with a static bubble, when the viscosity ratio for the two fluids is set to unity.

The radius of the bubble is 30 lattices and the simulation domain is made up of 100×100 lattices. Figure 2.4 shows the equilibrium droplet shape and velocity field for $\nu_R = \nu_B = 0.33$ at $\sigma = 0.001$. We measured the maximum velocity magnitude of the bubble with respect to different fluid viscosities (i.e., $\tau = 0.51, 0.53, 0.8, 1, 1.5$) and different surface tension (i.e., $\sigma = 0.1, 0.01, 0.001$) using both the 'CSF model' and 'Reis model'. The results are shown in Fig. 2.5. It is seen that the magnitude of spurious currents in 'CSF model' is maintained at a significantly smaller value than 'Reis model' for a range of viscosity, especially when surface tension becomes relatively larger. Thus 'CSF model' is used in all of the simulations from now on.

It is worth mentioning that a generalised perturbation operator is derived by Liu et al. [114] for the D3Q19 lattice. This operator takes the form of the 'Reis model' collision operator as shown in Eq. (2.41) while using the concept of a continuum surface force to construct the perturbation operator, by setting the divergence of stress tensor equal to the macroscopic interfacial force. It is written as

$$(\Omega_i^k)^{(2)} = \frac{A_k}{2} |\boldsymbol{\nabla} \rho^N| \left[W_i \frac{(\boldsymbol{c}_i \cdot \boldsymbol{\nabla} \rho^N)^2}{|\boldsymbol{\nabla} \rho^N|^2} - B_i \right], \tag{2.49}$$

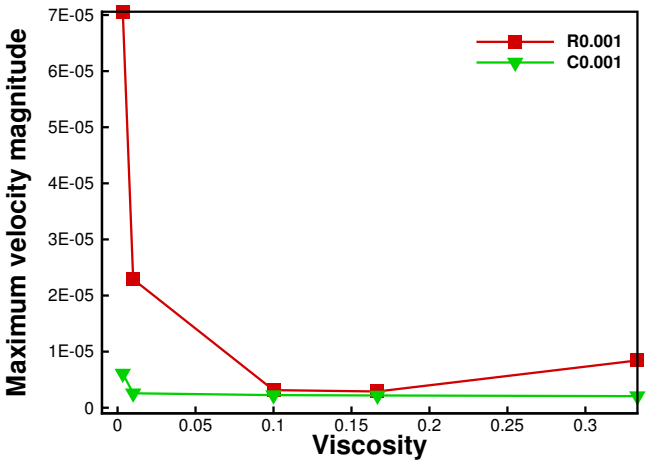

(a) $\sigma = 0.001$

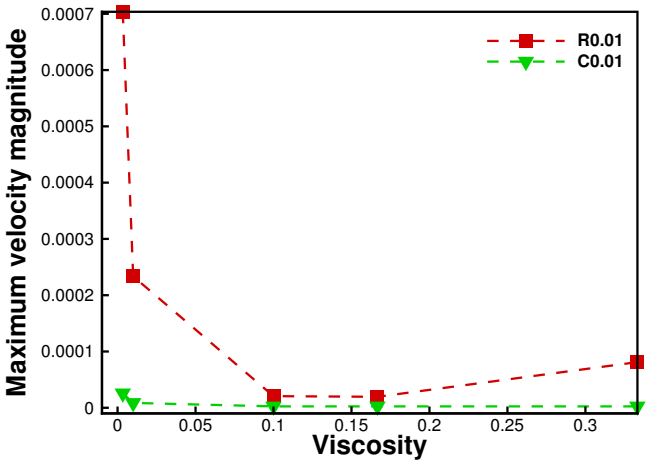

(b) $\sigma = 0.01$

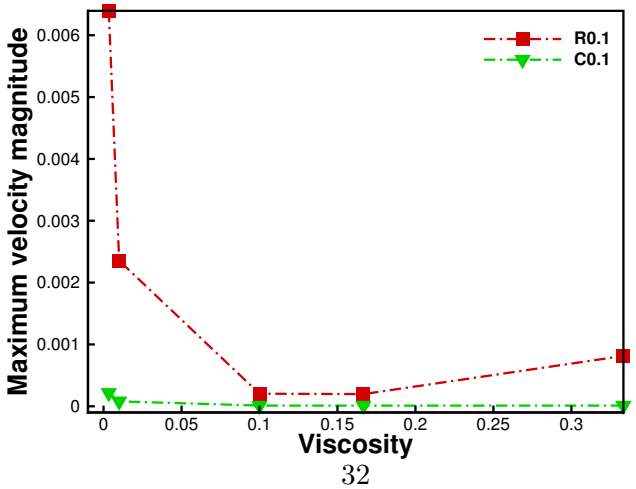

(c) $\sigma = 0.1$

Figure 2.5: The maximum spurious currents with different surface tension of $\sigma = 0.001,\ 0.01$ and 0.1 and viscosity of $\nu_R = \nu_B = 0.0033, 0.01, 0.1, 0.167$ and 0.33 (viscosity ratio equals to one). Note that 'R' refers to 'Reis model' and 'C' means 'CSF model'.

where $B_0 = -\frac{2+2\chi}{3\chi+12}c^2, B_{1-6} = \frac{\chi}{6\chi+24}c^2$, and $B_{7-18} = \frac{1}{6\chi+24}c^2$. χ is a free parameter. Moreover, the interfacial tension σ is analytically obtained without any additional analysis and assumptions[114]

$$\sigma = \frac{2}{9}(A_R + A_B)\tau, \tag{2.50}$$

where τ is the relaxation time of the fluid mixture. It is easily seen that the interfacial tension can be flexibly chosen by adjusting A_R and A_B.

2.5.1.3 Recolouring operator

The perturbation operator does not conserve each of the colour density. Another recolouring step is needed to promote phase segregation and maintain the interface between fluids. There are mainly two widely used recolouring algorithms. The first one is proposed by Gunstensen et al. [35], the colours are separated by maximizing the work W done by the colour flux $\boldsymbol{K}(\boldsymbol{x})$ against the colour gradient $\boldsymbol{G}$

$$\boldsymbol{K}(\boldsymbol{x}) = \sum_i \left[f_i^R(\boldsymbol{x}, t) - f_i^B(\boldsymbol{x}, t)\right] \boldsymbol{c}_i, \tag{2.51}$$

$$W = \boldsymbol{K} \cdot \boldsymbol{G} = \sum_i [f_i^{R*}(\boldsymbol{x}, t) - f_i^{B*}(\boldsymbol{x}, t)]\boldsymbol{c}_i \cdot \boldsymbol{G}, \tag{2.52}$$

subject to the constraints

$$\sum_i f_i^{R*} = \rho_R, \tag{2.53}$$

$$f_i^{R*} + f_i^{B*} = f_i^*, \tag{2.54}$$

which locally conserve individual densities of the red and blue fluids, and the total distribution function in each lattice direction. In this way, the maximum number of the red particles available are sent in the directions close to the colour gradient $\boldsymbol{G}$, i.e., perpendicular to the interface, while the blue particles are sent in the opposite direction, subject to constraints (2.53) and (2.54). However, this recolouring algorithm is reported to generate fluctuations in the pressure tensor and the velocity, even in the simple case of a non-inclined planar interface [34]. In addition, Latva-Kokko et al. [115] found the potential drawback of lattice pinning of this recolouring technique. It happens if the fluid velocity is low enough or if the bubble size is small enough, for example, if a lattice site is near or at the interface of blue and red fluids, but the flow is too weak to move many red particles from one site to another. The interface then becomes pinned to the lattice. To solve this problem, they suggested an alternative

recolouring scheme following the work of d'Ortona et al. [116], which slightly widens the interface but removes lattice pinning and minimises the spurious velocities:

$$\begin{aligned}(\Omega_i^R)^{(3)} &= \frac{\rho_R}{\rho} f_i^* + \beta \frac{\rho_R \rho_B}{\rho^2} f_i^{(eq)}(\rho, \boldsymbol{u} = 0) \cos(\varphi_i), \\ (\Omega_i^B)^{(3)} &= \frac{\rho_B}{\rho} f_i^* - \beta \frac{\rho_R \rho_B}{\rho^2} f_i^{(eq)}(\rho, \boldsymbol{u} = 0) \cos(\varphi_i).\end{aligned} \tag{2.55}$$

Based on the above work, Halliday et al. [117] later defined a slightly modified colour segregation as

$$\begin{aligned}(\Omega_i^R)^{(3)} &= \frac{\rho_R}{\rho} f_i^* + \beta \frac{\rho_R \rho_B}{\rho^2} f_i^{(eq)}(\rho, \boldsymbol{u} = 0) \cos(\varphi_i) \left|\boldsymbol{c}_i\right|, \\ (\Omega_i^B)^{(3)} &= \frac{\rho_B}{\rho} f_i^* - \beta \frac{\rho_R \rho_B}{\rho^2} f_i^{(eq)}(\rho, \boldsymbol{u} = 0) \cos(\varphi_i) \left|\boldsymbol{c}_i\right|,\end{aligned} \tag{2.56}$$

where $f_i^* = \sum_k f_i^{k*}$ denotes the post-perturbation, pre-segregation value of the total distribution function along the i-th discrete velocity direction, and $f_i^{eq} = \sum_k f_i^{k,eq}$ is the total equilibrium distribution function. β is the segregation parameter related to the interface thickness, and its value must be between 0 and 1 to ensure positive particle distributions. The interface becomes less diffuse as β increases. It is chosen to be 0.7 in all the simulations in this context to maintain a steady interface between the two fluids [117]. φ_i is the angle between the indicator function gradient $\boldsymbol{\nabla}\rho^N$ and the lattice vector $\boldsymbol{c}_i$, which is defined by

$$\cos(\varphi_i) = \frac{\boldsymbol{c}_i \cdot \boldsymbol{\nabla}\rho^N}{|\boldsymbol{c}_i||\boldsymbol{\nabla}\rho^N|}. \tag{2.57}$$

2.5.1.4 Calculation of partial derivatives

To generate isotropic interfacial tension and reduce the spurious currents as well as minimise the discretization error, a fourth-order isotropic finite difference is used to calculate the partial derivatives. The concept of isotropic finite difference was first introduced by Kumar [118] and it ensures that the error term of the finite difference discretization is isotropic. Later Shan [119] pointed it out that using higher order isotropic gradient operators can significantly reduce the spurious current. Following his work, Sbragaglia et al. [120] further generalized the 2D and 3D gradients of higher isotropic order. Leclaire et al. [121] integrated the isotropic colour gradient discretization into a two-phase flow simulation of steady bubble, it was found that the spurious current can be reduced by one order of magnitude and the accuracy of colour gradient LBM can be improved significantly. In brief, it takes the following form, for example,

for a variable ψ, the partial derivatives can be calculated by

$$\boldsymbol{\nabla}\psi(\boldsymbol{x},t) = \frac{1}{c_s^2}\sum_i W_i\psi(\boldsymbol{x}+\boldsymbol{c}_i\delta_t,t)\boldsymbol{c}_i. \tag{2.58}$$

2.5.1.5 Conversion of lattice units to physical units and choice of simulation parameters

All quantities used in the simulation are in lattice units with the LBM. Proper units must be chosen to represent the physics of an actually existing system. Bearing in mind that lattice Boltzmann method can act as a good approximation to solve the incompressible Navier-Stokes equations on the conditions that the mach number is low enough (e.g. $Ma < 0.3$). Therefore, discretization of the system is discussed in terms of macroscopic variables. In order to match the parameters in the lattice units toward their physical counterpart, three main physical quantities are chosen as the reference values according to the Buckingham π theorem [122]: the length scale (l_0), the time scale (t_0) and the mass scale (m_0). In the following, superscript phy denotes physical units:

$$\delta_x^{phy} = l_0\delta_x, \quad \delta_t^{phy} = t_0\delta_t, \quad \rho^{phy} = \rho\frac{m_0}{l_0^3} \tag{2.59}$$

We define the lattice spacing δ_x, the simulation time step δ_t and the lattice density ρ all as unity in the simulations. Thus we have

$$\delta_x^{phy} = l_0, \quad \delta_t^{phy} = t_0, \quad \rho^{phy} = \frac{m_0}{\left(\delta_x^{phy}\right)^3} \tag{2.60}$$

Generally, the lattice units for length, time and mass are defined as lu, ts, and mu, respectively. Then, the units for the scaling factors l_0, t_0 and m_0 are written as $m\cdot(lu)^{-1}$, $s\cdot(ts)^{-1}$ and $kg\cdot(mu)^{-1}$, respectively. In this way, a simulation parameter in the lattice system multipied by $[l_0]^{n1}[t_0]^{n2}[m_0]^{n3}$ gives its corresponding physical value. Other important parameters in a typical two phase problem can also be obtained in a similar manner. For example:

- the magnitude of flow velocity $u^{phy} = u\frac{l_0}{t_0}$.
- the dynamic viscosity $\eta_{displaced}^{phy} = \eta_{displaced}\frac{m_0}{l_0 t_0}$.
- the interfacial tension $\sigma^{physical} = \sigma\frac{m_0}{t_0^2}$.

Certain major constraints exists due to the intrinsic restrictions of the LB algorithm for the selection of proper values for l_0, t_0 and m_0. As mentioned above, the constraint

of small Mach number requires that

$$Ma = \frac{u}{c_s} = \frac{u^{phy}}{\frac{1}{\sqrt{3}}\frac{\delta_x^{phy}}{\delta_t^{phy}}} = \frac{u^{phy}}{\frac{1}{\sqrt{3}}\frac{l_0}{t_0}} < 0.3 \tag{2.61}$$

In addition, the parameters should be chosen in a way that the simulation accuracy, stability and efficiency are reasonably taken into consideration.

The value of τ affects the accuracy. $\tau \gg 1$ should be avoided because the Knudsen number, namely the ratio of molecular mean free path, l_m, to the representative physical length scale, l_h: $Kn = l_m/l_h$, scales with τ [123]. And the lattice Boltzmann model is valid only for small Knudsen numbers.

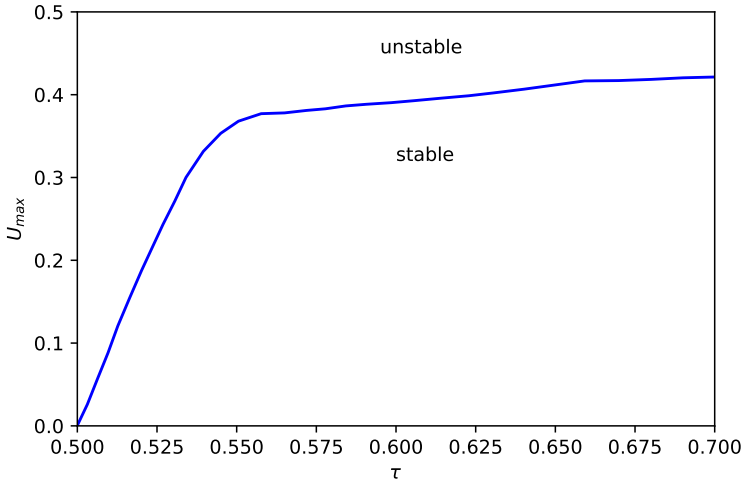

Figure 2.6: The neutral stability $U_{max} - \tau$ curve for LBE extracted from Niu et al. [5].

To achieve a high Reynolds number with the LBM, the usual approach is to decrease the viscosity as the velocity can not be increased without limit since the LBE recovers the NSE only in the low-Mach limit. However, the achievable maximum velocity is decreasing when τ approches 1/2 as shown in Fig. 2.6. Only when $\tau > 0.65$, one can have $U_{max} > 0.4$. It can also be seen that the simulation gets less stable as τ close to 1/2 [5]. In addition, more advanced collision operators, e.g. two-relaxation or multiple relaxation is more stable than single relaxation collision operator. As a rule of thumb, the range $(0.55, 1.5)$ is a good choice for relaxation time. And for τ close to 1/2, τ should obey

$$\tau > \frac{1}{2} + \frac{1}{8} U_{max}, \tag{2.62}$$

in order to get convergent solutions.

The number of lattice sites and iterations affects the efficiency of an LB simulation greatly. Generally the finer space and time are resolved, i.e. the smaller δ_x and δ_t are, the more memory and computing time the simulation requires. Hence the value of δ_x and δ_t should be as large as possible if the computational accuracy is not compromised.

2.5.2 Wetting boundary condition

Different fluids may have different affinities to the solid surfaces, which results in the formation of a certain contact angle involving two fluids and one solid phase. It is usually defined to quantify the wettability of a solid phase by a liquid via the Young's equation [100]

$$\sigma \cos\theta = \sigma_{wb} - \sigma_{wr}, \tag{2.63}$$

where σ is the red-blue fluid interfacial tension, θ is the contact angle, σ_{wb} is the

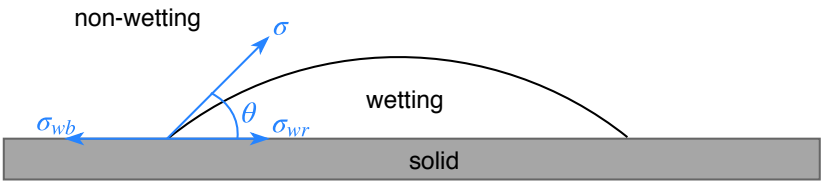

Figure 2.7: Schematic diagram of contact angle.

wall-blue fluid surface tension and σ_{wr} is the wall-red fluid surface tension as shown in Fig. 2.7.

2.5.2.1 Surface energy formulation - 'standard approach'

As a diffuse-interface method, the most widely-used wetting boundary condition for the colour gradient LBM is to set a virtual density at solid surfaces. This approach is originally proposed by Latva-Kokko et al. [124]. The prescribed virtual density is now used to calculate the phase field $\rho^N(\boldsymbol{x}_s)$ at the solid nodes $\boldsymbol{x}_s$. Then this $\rho^N(\boldsymbol{x}_s)$ is used for calculating the colour gradient $\boldsymbol{\nabla}\rho^N$ of the flow domain next to the solid

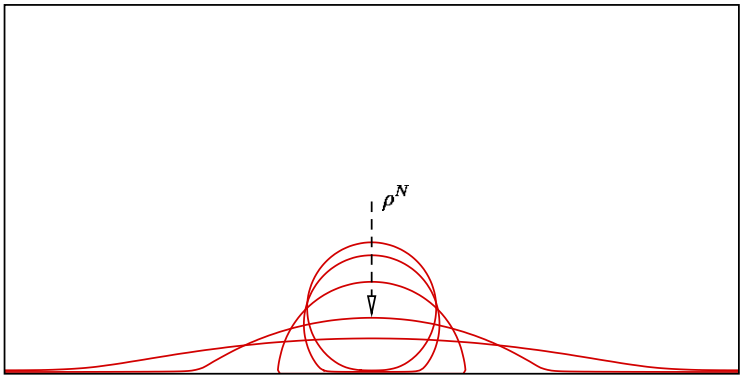

Figure 2.8: Different contact angles simulated by the 'standard approach'. The values of $\rho^N(\boldsymbol{x}_s)$ are taken as $\rho^N(\boldsymbol{x}_s) = \{-0.866, -0.5, 0, 0.5, 0.866\}$ along the direction of arrow. The computational domain is 200×100.

node. The contact angle is given as

$$\theta = \arccos \rho^N(\boldsymbol{x}_s). \tag{2.64}$$

This approach follows the assumption of Rowlinson and Widom [100] that the solid wall is a mixture of two fluids, thus having a certain value of the phase field $\rho^N(\boldsymbol{x}_s)$. Several studies adopted this 'standard approach' due to its ease in implementation [12, 23, 44, 68, 73]. Fig. 2.8 shows that different contact angles can be achieved by tuning the value of the phase field at the solid wall. The red fluid is initialized as a semicircular stationary droplet sitting on the centreline of the bottom wall, with a radius of $R = 25$. And the equilibrium state of the final droplet with different contact angles are shown in the figure.

However, it has been found in recent works [7, 125] that nonphysical mass transfer of the wetting phase appears along the boundary, and the numerical errors and spurious velocities may be accumulated during simulations, which potentially render meaningless results with the 'standard approach'. In addition, this problem becomes more apparent when the contact angle is less than 90°.

2.5.2.2 Geometric formulation - 'direct approach'

The 'direct approach' refers to modify the direction of the colour gradient at the boundary node $\boldsymbol{\nabla}\rho^N(\boldsymbol{x}_f)$ according to the prescribed contact angle.

Ba et al. [6] introduced an implementation of this wetting boundary condition using

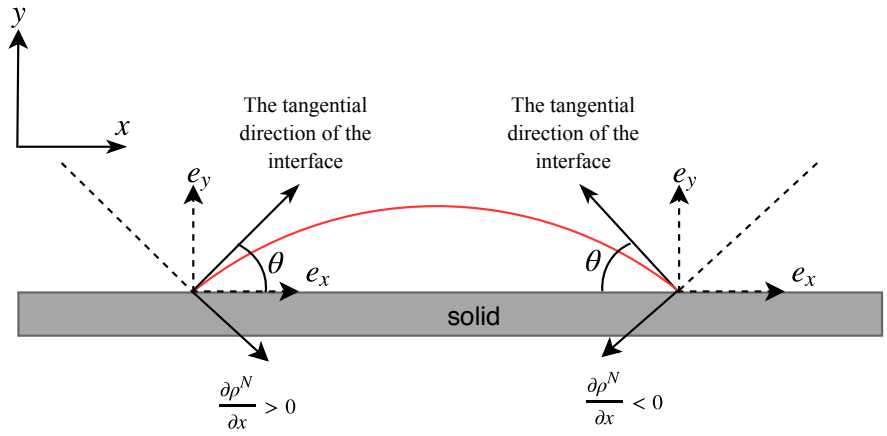

Figure 2.9: Schematic image of the wetting boundary condition implemented by Ba et al. [6].

$\theta_{prescribed}$	$\theta^{std}_{measure}$	θ^{std}_{error}	$\theta^{dir}_{measure}$	θ^{dir}_{error}
150	153.0	0.0200	148.0	-0.0133
120	133.6	0.1133	118.1	-0.0158
90	82.2	-0.0867	88.9	-0.0122
60	33.0	-0.4500	59.0	-0.0167
30	15.1	-0.4967	30.6	0.0200

Table 2.2: Comparison of the prescribed and simulated contact angle. The test case is a droplet sitting on a flat surface with the 'standard approach' and the 'direct approach' implemented by Ba et al. [6], respectively.

the strategy proposed by Ding and Spelt [126], using the geometrical properties of the indicator function $\boldsymbol{\nabla}\rho^N$ at the contact line. As shown in Fig. 2.9, for a prescribed contact angle θ, the colour gradient $\boldsymbol{\nabla}\rho^N$ at the boundary node should satisfy

$$\frac{\boldsymbol{\nabla}\rho^N}{|\boldsymbol{\nabla}\rho^N|} = \boldsymbol{n} = \begin{cases} -\sin\theta \boldsymbol{e}_x - \cos\theta \boldsymbol{e}_y, & \text{if} \quad \frac{\partial \rho^N}{\partial x} < 0, \\ \sin\theta \boldsymbol{e}_x - \cos\theta \boldsymbol{e}_y, & \text{if} \quad \frac{\partial \rho^N}{\partial x} > 0. \end{cases} \tag{2.65}$$

Thus a relationship between the two components of $\boldsymbol{\nabla}\rho^N$ at a boundary node is written as

$$\left(\frac{\partial \rho^N}{\partial y}\right)_{x,0} \sin\theta = -\left|\frac{\partial \rho^N}{\partial x}\right|_{x,0} \cos\theta. \tag{2.66}$$

And a central difference scheme is used to determine the $(\partial_x \rho^N)_{x,0}$

$$\left(\frac{\partial \rho^N}{\partial x}\right)_{x,0} = \frac{\left[(\rho^N)_{x+1,0} - (\rho^N)_{x-1,0}\right]}{2}. \tag{2.67}$$

This method has shown great accuracy compared to the 'standard approach' for simulation of wetting phenomena on a flat surface as can be seen in Table 2.2. However,

it is limited to straight flat boundaries.

For modelling contact angles at curved boundaries, Leclaire et al. [125] proposed to predict the colour gradient $\boldsymbol{\nabla}\rho^{N*}(\boldsymbol{x}_f)$ at the boundary fluid nodes, then correct its direction by linear least-square interpolating the interface normal at the interior fluid nodes and the theoretical orientation of the interface normal at the wall.

Later Leclaire et al. [127] extend this approach to three dimensions by using the secant method to find the vector that forms an angle θ with the wall normal n_s. This vector is then normalized before it is used as the corrected direction, i.e, to replace the orientation of $\boldsymbol{\nabla}\rho^{N*}(\boldsymbol{x}_f)$. However, this recurrence relation would in principle need to be carried out for many iterations to find an exact solution, which will inevitably increase the computational costs. As a result, it seems untenable that in the literature, the iteration step is limited to $n = 2$, in order to avoid high computational costs. However, it is argued that this approach works without extra treatment for problems with complex geometry, density and viscosity ratios.

Meanwhile, Xu et al. [69] proposed a way to find the proper direction of the colour gradient $\boldsymbol{\nabla}\rho^{N*}(\boldsymbol{x}_f)$ at the boundary fluid nodes by rotating the wall normal clockwise or counter-clockwise with the contact angle θ. In algorithm, this approach is easier to implement than Leclaire et al. [125, 127]. In terms of accuracy, Yu et al. [46] shows that Xu's approach has better accuracy than Leclaire's for moving contact line problem when simulating capillary filling. We will take a detailed look at this approach. To explain this wetting boundary condition, let us define

- R_F: the list of lattice sites that are considered as fluid but not in contact with any solid site;
- R_{Fs}: the list of lattice sites that are considered as fluid and are in contact with at least one solid site;
- R_{Sf}: the list of lattice sites that are considered as solid and are in contact with at least one fluid lattice site;
- R_S: the list of lattice sites that are considered as solid but are not in contact with any fluid lattice sites.

Figure 2.10 gives an example of various categories of lattice sites. For the lattice sites in R_F, ρ^N from all the neighbouring sites are known, while for the lattice sites in R_{Fs}, the value of ρ^N in R_{Sf} is unknown for calculating $\boldsymbol{\nabla}\rho^N$ using Eq. (2.58). Thus, these

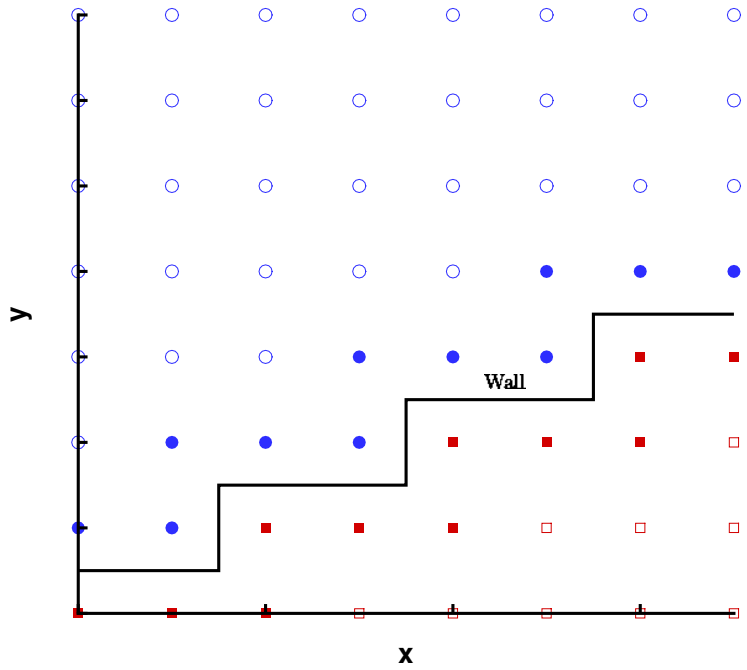

Figure 2.10: Illustration of four categories of lattice sites. The blue hollow circles represent interior fluid nodes in R_F, blue filled circles represent boundary fluid nodes in R_{Fs}, red filled squares represent boundary solid nodes in R_{Sf} and red empty squares represent interior solid nodes in R_S. The black solid line symbolizes the location of the wall in the simulation if use halfway bounce-back scheme.

values are extrapolated using the lattice link weighted average as following:

$$\rho^N(\boldsymbol{x} \in R_{Sf}) = \frac{\sum_{(i:\boldsymbol{x}+\boldsymbol{c}_i\delta_t \in R_{Fs})} W_i \rho^N(\boldsymbol{x}+\boldsymbol{c}_i\delta_t)}{\sum_{(i:\boldsymbol{x}+\boldsymbol{c}_i\delta_t \in R_{Fs})} W_i}. \tag{2.68}$$

Thus the colour gradient at the boundary fluid nodes (R_{Fs}) can be predicted, denoted as $\boldsymbol{\nabla}\rho^{N*}$. While its direction does not necessarily match the prescribed contact angle, the correction step is needed. It is to modify the direction of $\boldsymbol{\nabla}\rho^{N*}$ only and keep its modulus $\left|\boldsymbol{\nabla}\rho^{N*}\right|$ unchanged. The direction of the predicted $\boldsymbol{\nabla}\rho^{N*}$ is written as

$$\boldsymbol{n}^* = \frac{\boldsymbol{\nabla}\rho^{N*}}{|\boldsymbol{\nabla}\rho^{N*}|}. \tag{2.69}$$

It can be understood as the estimated unit normal vector for the fluid interface at the boundary fluid nodes near the wall. For a boundary fluid lattice node, two unit normal vectors can be defined. They are the wall normal $\boldsymbol{n}_s$ and the unit vector for the fluid interfaces $\boldsymbol{n}_1$ (or $\boldsymbol{n}_2$). Figure 2.11 gives a clear picture of these normal vectors. The basic idea is to evaluate the Euclidean distances D_1 (D_2) between $\boldsymbol{n}^*$ and $\boldsymbol{n}_1(\boldsymbol{n}_2)$, then replace $\boldsymbol{n}^*$ with either $\boldsymbol{n}_1$ or $\boldsymbol{n}_2$, whichever has the shorter Euclidean distance to $\boldsymbol{n}^*$. The Euclidean distance is defined by

$$D_1 = |\boldsymbol{n}^* - \boldsymbol{n}_1|, \quad D_2 = |\boldsymbol{n}^* - \boldsymbol{n}_2|. \tag{2.70}$$

The corrected unit normal vector for the fluid interface $\boldsymbol{n}_c$ is then selected by

$$\boldsymbol{n}_c = \begin{cases} \boldsymbol{n}_1, & D_1 \leq D_2, \\ \boldsymbol{n}_2, & D_1 > D_2. \end{cases} \tag{2.71}$$

Finally, the modified colour gradient $\boldsymbol{\nabla}\rho^N$ is obtained by

$$\boldsymbol{\nabla}\rho^N = \left|\boldsymbol{\nabla}\rho^N\right| \boldsymbol{n}_c. \tag{2.72}$$

To get $\boldsymbol{n}_s$ in the first place, an eighth-order isotropic discretization is used [69], given by

$$\boldsymbol{n}_s(\boldsymbol{x} \in R_{Fs}) = \frac{\sum_l W(|\boldsymbol{c}_l|^2) s(\boldsymbol{x}+\boldsymbol{c}_l\delta_t)\boldsymbol{c}_l}{\left|\sum_l W(|\boldsymbol{c}_l|^2) s(\boldsymbol{x}+\boldsymbol{c}_l\delta_t)\boldsymbol{c}_l\right|}, \tag{2.73}$$

where $\boldsymbol{c}_l$ is the lth mesoscopic velocity corresponding to the eighth-order isotropic

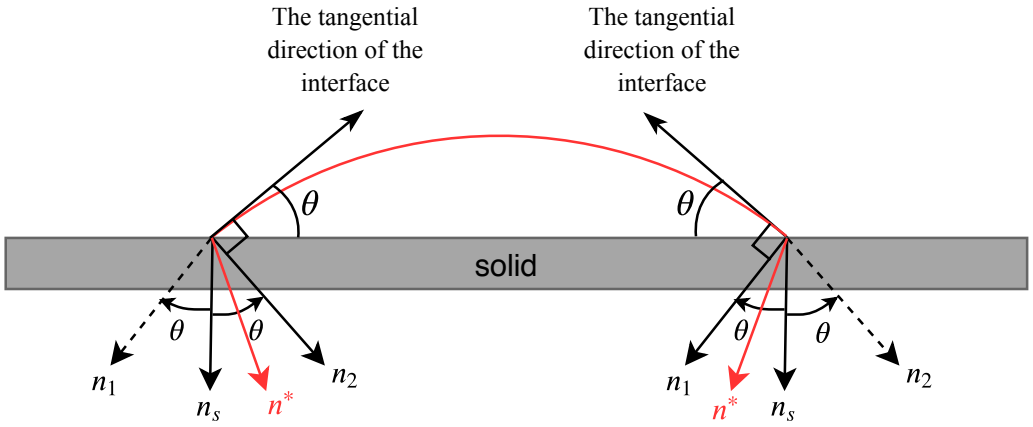

Figure 2.11: Illustration of the unit normal vector for the solid wall ($\boldsymbol{n}_s$) and two possible theoretical unit normal vectors ($\boldsymbol{n}_1$ and $\boldsymbol{n}_2$) for the fluid interface (figure inspired by [7]). $\boldsymbol{n}^*$ is the predicted unit normal vector to the fluids interface.

discretization, provided by Sbragaglia et al. [120]:

$$W(|\boldsymbol{c}_l|^2) = \begin{cases} \frac{4}{21} & |\boldsymbol{c}_l|^2 = 1, \\ \frac{4}{45} & |\boldsymbol{c}_l|^2 = 2, \\ \frac{1}{60} & |\boldsymbol{c}_l|^2 = 4, \\ \frac{2}{315} & |\boldsymbol{c}_l|^2 = 5, \\ \frac{1}{5040} & |\boldsymbol{c}_l|^2 = 8. \end{cases} \tag{2.74}$$

And $\boldsymbol{s}(x)$ is an indicator function which equals to 1 at the fluid nodes and 0 at the solid nodes. Then the two theoretical normal vectors for the fluid interface are obtained by rotating $\boldsymbol{n}_s$ clockwise or counter-clockwise with the prescribed contact angle θ, resulting in

$$\begin{aligned} \boldsymbol{n}_1 &= (n_{sx}\cos\theta - n_{sy}\sin\theta, n_{sy}\cos\theta + n_{sx}\sin\theta), \\ \boldsymbol{n}_2 &= (n_{sx}\cos\theta + n_{sy}\sin\theta, n_{sy}\cos\theta - n_{sx}\sin\theta). \end{aligned} \tag{2.75}$$

2.5.2.3 Summary

Aiming at dealing with water and oil displacement within complex geometry, the algorithm proposed by Xu et al. [69] is implemented in this thesis to impose the contact angle on solid surfaces. This algorithm is able to precisely control the contact angle for both static and dynamic problems which is essential for accurate simulations of two-phase displacement in porous media. It has been extensively validated against static droplet resting on a flat surface and on a cylindrical surface by Xu et al. [69]. Further

validations for simulating the moving contact line problem, i.e., capillary filling are shown in Chapter 4, along with the relative permeability vadilation, i.e., the cocurrent flow in a 2D channel.

Chapter 3

Properties of porous media and two immiscible fluids

3.1 Definition of porous media and porosity

Porous media is a solid material containing holes or voids, either connected or non-connected, dispersed within it in either a regular or random manner provided that such holes occur relatively frequently within the solid. A fluid can flow through a porous material only if at least some of the pores are interconnected. The interconnected pore space is called the effective pore space, while all the pore space is termed the total pore space [128]. One important parameter to characterize the porous medium is porosity. The porosity is defined as

$$n = \frac{V_{pores}}{V_{bulk}} = \frac{V_{pores}}{V_{pores} + V_{matrix}}, \tag{3.1}$$

where V_{pores} is the pore volume, and V_{matrix} is the volume of the solid matrix within the bulk volume V_{bulk}. The porosity varies between zero and unity, depending on its formation and the type of porous material.

3.2 Fluid flow in porous media

The fluid flow in porous media is commonly-found in nature and man-made devices, processes such as ground water hydrology, oil and gas deposit exploitation, chemical engineering, soil science, soil mechanics and new energy development, etc. The flow is also called percolation or "seepage flow" sometimes because of its generally low speed

of movement. It is a classical multi-scale problem, normally three scales are involved in the oil and gas extraction, i.e., pore scale, representative elementary volume (REV) scale and field scale [76].

3.2.1 Pore scale perspective

On the level of pore scale, the research object is to resolve fluid dynamical behaviour in single or several pores. It is to study the transportation process of the fluid within these pores that the information of the flow field will be obtained. Generally, the fluid flow in the pores obeys the Navier-Stokes equation. The solid surface of the porous medium is seen as the boundary of the flow field. And the interaction of the fluid and porous medium is implemented by the boundary condition which has been introduced in detail in Section 2.5.2. Due to the extremely irregular pore geometries in the porous media, it is very difficult to model this kind of flow with conventional computational method. Zhang et al. [129] showed that the continuum-scale two-phase flow modelling is only able to predict the general displacement pattern in a dual-permeability pore network micromodel with a 22% discrepancy, and unable to capture the unstable displacement by viscous fingering mechanism, hence do not accurately predict the increases in saturation. As an effective method, the lattice Boltzmann equation has been applied to the porous flow successfully. The particle nature of LBM makes it convenient to deal with the complex flow field with the simple bounce back rule. The locality and efficiency of the bounce back scheme brings LBM advantage when dealing with flows in the irregular pore throats. Despite the need to know the detailed structure of the porous media beforehand which can now be tackled with X-ray computed tomography (XCT), the detailed flow information in the porous media can be obtained and the underlying physics can be explored. However, the computational size is generally limited, i.e., varies from several micrometres to several millimetres, as the flow field in each pore needs to be resolved.

3.2.2 REV scale perspective

The REV scale is a scale much larger than the pore scale. The REV refers to a control volume in the porous media, which includes enough pores, and its size is much larger than a single pore, while at the same time much smaller than the field size of interest. At the REV scale, the porous medium can be seen as a continuum medium. The medium allows a meaningful average over the microscopic heterogeneities (can be considered homogeneous) at the pore scale when the sample size is large enough where

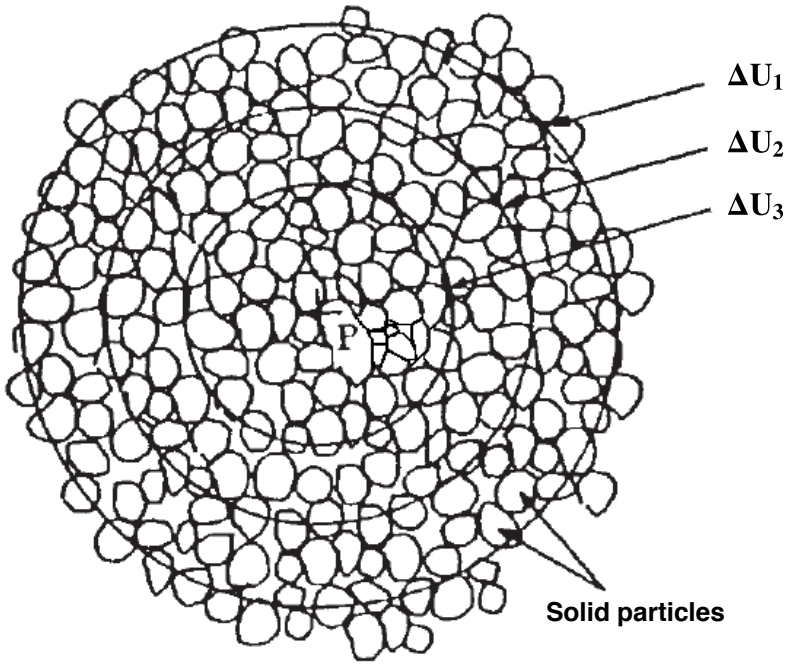

Figure 3.1: Schematic of the volume ΔU_i. Gradually shrinking the size of ΔU_i around P as a centreoid, we have: $\Delta U_1 > \Delta U_2 > \Delta U_3$ [8].

parameters of interest become independent of the size of the sample. This sample size is the so-called representative elementary volume. Upon further increase the sample size, parameters may become nonstationary [130].

For example, let P be a mathematical point inside the domain occupied by the porous medium, consider a volume ΔU_i (say, having the shape of a sphere as in Fig. 3.1) much larger than a single pore or grain, for which P is the centroid. For this volume, we may determine the ratio:

$$n_i = n_i(\Delta U_i) = \frac{(\Delta U_v)_i}{\Delta U_i}, \tag{3.2}$$

where $(\Delta U_v)_i$ is the volume of pores within ΔU_i. Repeating this procedure, a sequence of values $n_i(\Delta U_i), i = 1, 2, 3, ...$ can be obtained by gradually reducing the size of ΔU_i around P as a centroid: $\Delta U_1 > \Delta U_2 > \Delta U_3 \ldots$

For large values of ΔU_i, the ratio n_i may undergo gradual changes as ΔU_i is reduced, especially when the considered domain is inhomogeneous. Below a certain value of ΔU_i, depending on the distance of P from boundaries of inhomogeneity, these changes or fluctuations tend to decay, leaving only small-amplitude fluctuations that are due to the random distribution of pore sizes in the neighbourhood of P. However, below a certain value ΔU_0 we suddenly observe large fluctuations in the ratio n_i. This happens as the

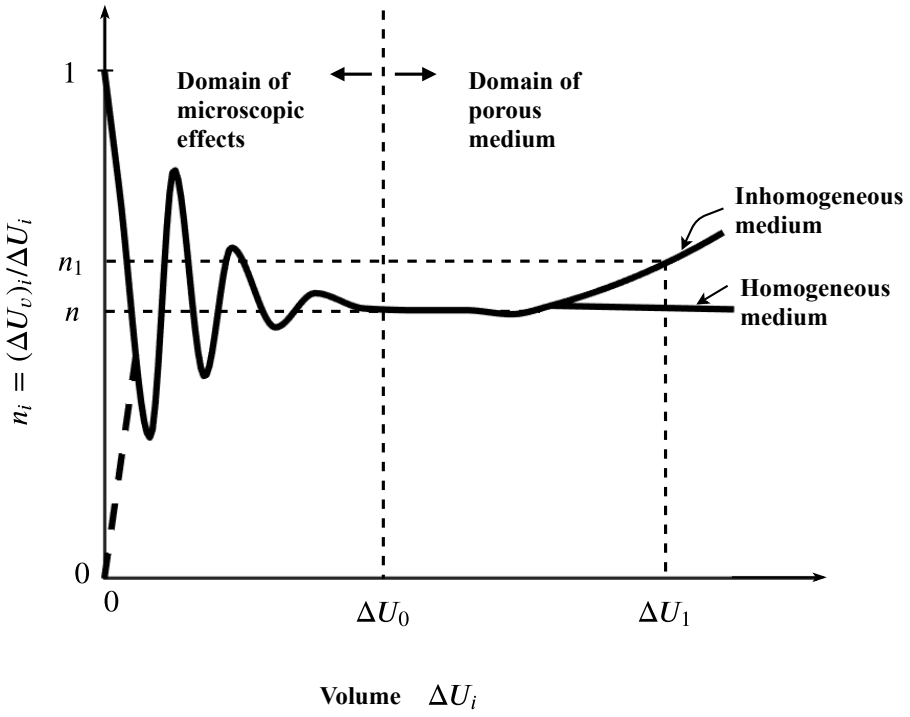

Figure 3.2: Porosity and representative elementary volume [9].

dimensions of ΔU_i approach those of a single pore. Finally, as $\Delta U_i \to 0$, converging on the mathematical point P, n_i will become either one or zero, depending on whether P is inside a pore or inside the solid matrix of the medium. Figure 3.2 shows the relationship between n_i and ΔU_i.

The medium's porosity $n(P)$ at point P is then defined as the limit of the ratio n_i as $\Delta U_i \to \Delta U_0$:

$$n(P) = \lim_{\Delta U_i \to \Delta U_0} n_i \{\Delta U_i(P)\} = \lim_{\Delta U_i \to \Delta U_0} \frac{(\Delta U_v)_i(P)}{\Delta U_i}. \tag{3.3}$$

For values of $\Delta U_i < \Delta U_0$, we must consider the actual presence of pores and solid particles; in this range there is no single value that can represent the porosity at P. The volume ΔU_0 is therefore the representative elementary volume (REV).

The LBE based on REV scale does not solve the flows in the pores, instead to solve the average flows at REV scale. In this approach, the interaction between the fluid and the medium is described by some empirical models such as the mostly widely used model Darcy's law,

$$q = -\frac{K}{\eta} \nabla P, \tag{3.4}$$

where q is the specific discharge (or flow rate per unit area of cross section or flux) corresponding to the pressure gradient ∇P (equivalent to $\Delta P/L$, L is the length of the porous medium). K is the intrinsic permeability related to the structure of the medium. **Permeability** represents the capacity for flow to go through the porous medium. The dimensions of permeability are length squared, often expressed as darcies (1 darcy $= 0.987 \times 10^{-8}\text{cm}^2$), millidarcies, or micrometers squared. One of the most widely accepted derivations of permeability and its relationship to porous medium properties is given by the Kozeny-Carman equation,

$$K = c_0 \frac{n^3}{S^2}, \tag{3.5}$$

where c_0 is a constant varies slightly according to the geometrical form of the individual channels in the model, and S is the specific surface area of the medium. The advantage of such LBE is that only a few statistical parameters are required rather than detailed pore structures, e.g., porosity and permeability, so the computational efficiency is much higher than the pore-scale approach. Consequently, REV scale LBE can be used for engineering purpose. However, the accuracy of such simulations relies on the empirical or semi-empirical model and the parameters used.

3.2.3 Field scale perspective

The field scale is the largest scale of all. It is used to describe phenomena of transport in geological formation which are typically highly heterogeneous. Usual distances of interest ranges from metres to kilometres. Details of analysis and experimental operation at this scale can be found in Ref [131].

3.2.4 Summary

Although there are many scales of interest concerning multiphase flow in the subsurface, of particular interest are macroscopic variables that can be associated with a representative elementary volume. In a REV, macroscopic variables are typically defined as the average of microscopic variables. Therefore, it is necessary to determine whether the sample size simulated is large enough to be a REV.

3.3 Phenomenology of flows in porous media

For a simultaneous flow of two immiscible fluids in the porous medium, the interfacial tension between the two fluids is nonzero, because of the difference between the inward attraction of the molecules in the interior of each fluid and those at the contact surface. There is a certain contact angle θ at the contact point for balancing the interfacial tensions between any pair of two fluids and the solid. When the angle $\theta < 90°$, the fluid is termed the wetting fluid; when $\theta > 90°$, the fluid is called the nonwetting fluid.

3.3.1 Drainage

For drainage, the porous media is initially filled with a wetting fluid, a nonwetting fluid is forced into the porous media to displace the wetting fluid. It is a fluid flow process in which the saturation of the nonwetting fluid increases.

3.3.2 Imbibition

In the case of imbibition, the porous media is initially filled with the nonwetting fluid, and it is displaced by a wetting fluid. In the process of imbibition, the saturation of the wetting fluid increases and the nonwetting fluid saturation decreases.

3.4 Two-phase governing equation

3.4.1 Conservation equation and the extended Darcy's law

In the absence of sources and wells, the mass conservation equation that describes a substance with density g_α and average velocity $\boldsymbol{V}_{G_\alpha}$ is [9]:

$$\frac{\partial(g_\alpha)}{\partial t} + \nabla \cdot (g_\alpha \boldsymbol{V}_{G_\alpha}) = 0. \tag{3.6}$$

Applying this equation to the flow of two immiscible fluids in porous media, the mass conservation equation for each fluid is written as:

$$\frac{\partial(nS_\alpha\rho_\alpha)}{\partial t} + \nabla \cdot (\rho_\alpha \boldsymbol{q}_\alpha) = 0, \quad \alpha = 1, 2, \tag{3.7}$$

where n is the porosity of porous medium, S_α is the saturation of phase α, defined as

$$S_\alpha = \frac{\text{volume of fluid } \alpha \text{ within an REV}}{\text{volume of voids within an REV}}, \quad \sum_{(\alpha)} S_\alpha = 1. \tag{3.8}$$

$g_\alpha = nS_\alpha\rho_\alpha$ is the mass of fluid α per unit volume of porous medium, and $g_\alpha \boldsymbol{V}_{G_\alpha} = nS_\alpha\rho_\alpha\boldsymbol{V}_\alpha = \rho_\alpha\boldsymbol{q}_\alpha$ is the mass flux (mass per unit area per unit time) of fluid α. For a homogenous incompressible fluid in the porous medium, Eqn. (3.7) becomes:

$$\frac{\partial(nS_\alpha)}{\partial t} + \nabla \cdot \boldsymbol{q}_\alpha = 0. \tag{3.9}$$

The Darcy's law may be extended to describe the two immiscible fluids specially without considering gravitational effects, it can be written as:

$$\boldsymbol{q}_\alpha = -\frac{K_\alpha}{\eta_\alpha}\nabla P_\alpha, \tag{3.10}$$

where K_α is the effective permeability of the fluid α. The relative permeability for each fluid is then defined as

$$K_{r\alpha} = \frac{K_\alpha}{K}. \tag{3.11}$$

The Relative permeability is a dimensionless function that usually varies from 0 to 1. Considering a wetting fluid (subscript w) and a nonwetting fluid (subscript nw), the relative permeability depends only on the saturation, which is expressed by

$$K_{r\alpha} = K_{r\alpha}(S_w). \tag{3.12}$$

The two fluids pressures are related by the **capillary pressure** P_c (pressure difference across the interface of the two immiscible fluids) through the expression

$$P_n - P_w = f(S_w) = P_c, \tag{3.13}$$

where the capillary pressure is a measure of a porous medium to suck in the wetting fluid phase or to expel the nonwetting phase. The above four equations including Eqn. (3.9), (3.10), (3.12),(3.13) are used together to describe the flow of the two phase immiscible fluids in porous media. It should be noted that Eqn. (3.13) is the traditional $P_c - S_w$ relationship based on the assumption that P_c is uniquely described by S_w at static conditions. Other studies [132, 133] argue a constitutive relationship between $P_c - S_w - a_{nw}$ where the specific interfacial area between the fluid phases are explicitly taken into consideration. Including the interfacial area results in a smooth functional form for capillary pressure however the interfacial area is often difficult to measure in

core analysis [1]. The use of constitutive relationship implies that the sample is large enough to be considered as a REV. The dynamics of fluids at the larger scale can be described using appropriate partial differential equations once the constitutive relations are known.

3.4.2 Relative permeability/Capillary pressure - Saturation relationship

3.4.2.1 Burdine's equation

The relative permeability can be estimated by assuming a particular model of the pore structure. The simplest model of a porous medium is to consider a bundle of parallel cylindrical tubes, whose radii r vary within the range of (r_1, r_2) with a distribution function $\alpha(r)$. Assuming that the bundle is cut into a large number of thin slices then the short tubes in each slice are rearranged randomly and the slices are reassembled also randomly, one example of the cross-section for the slice is shown in Fig. 3.3. After

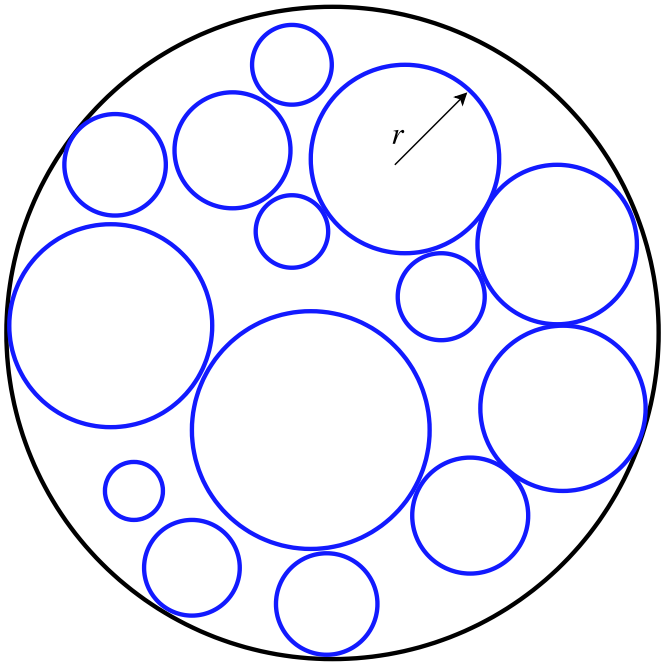

Figure 3.3: Schematic of the cross-section for one slice of the capillary tubes.

a series of analysis, the wetting fluid relative permeability is written as [9, 134]

$$K_{rw} = (\frac{S_w - S_r}{1 - S_r})^2 \frac{\int_{S_r}^{S_w} \frac{dS_w}{P_c{}^2}}{\int_{S_r}^{1} \frac{dS_w}{P_c{}^2}}, \tag{3.14}$$

where S_w is the fraction of the total pore space occupied by the wetting phase. S_r is the residual wetting phase which can be regarded as part of the solid structure. Corey [135] introduced the concept of effective saturation S_e by

$$S_e = (\frac{S_w - S_r}{1 - S_r}). \tag{3.15}$$

Replacing the variable S_w in Eqn.(3.14) by S_e, the wetting fluid relative permeability is rewritten as

$$K_{rw} = (S_e)^2 \frac{\int_0^{S_e} \frac{dS_e}{P_c{}^2}}{\int_0^1 \frac{dS_e}{P_c{}^2}}. \tag{3.16}$$

Similarly, for the nonwetting fluid

$$K_{rnw} = (1 - S_e)^2 \frac{\int_{S_e}^1 \frac{dS_e}{P_c{}^2}}{\int_0^1 \frac{dS_e}{P_c{}^2}}. \tag{3.17}$$

Equations (3.16) and (3.17) are also known as Burdine's equation [134] for relative permeability. The derivation can be seen in Appendix B.

3.4.2.2 Corey-type relationship for Relative permeability/Capillary pressure

The above Burdine's equation is said to be based on laboratory experiments carried out under stationary conditions, it can be extended using the following suggestions by Brooks and Corey [134] based on a large number of drainage experiments:

$$S_e = (\frac{P_b}{P_c})^\lambda \quad \text{for} \quad P_c \geq P_b, \tag{3.18}$$

where P_b is the entry capillary pressure and λ is the pore-size distribution index which must be determined experimentally. Then Eqns. (3.16) and (3.17) become:

$$K_{rw} = (S_e)^{\frac{2}{\lambda}+3} = (\frac{P_b}{P_c})^{(2+3\lambda)}, \quad P_c \geq P_b, \tag{3.19}$$

$$K_{rnw} = (1 - S_e)^2 (1 - S_e^{\frac{2+\lambda}{\lambda}}) = [1 - (\frac{P_b}{P_c})^\lambda]^2 [1 - (\frac{P_b}{P_c})^{2+\lambda}]. \tag{3.20}$$

Equations (3.19) and (3.20) present the theoretical relationship between the capillary pressure P_c, effective saturation S_e, wetting fluid relative permeability K_{rw} and the nonwetting fluid relative permeability K_{rnw}.

3.5 Summary

In this Chapter, we have introduced the representative characteristic parameters of porous medium - porosity, and briefly introduced the three perspectives to study porous medium. We have also looked at two relationships that related to the two-phase flow within the porous media from the theoretic perspective, including the capillary - saturation curve and the relative permeability - saturation curve. In summary, porous medium is with complex geometry in nature, the multiphase flow in these confined systems are even more complicated. In this thesis, we resort to numerical modelling to obtain pore scale information and as a guide to understand large-scale natural processes. In the following two chapters, we will describe our efforts to directly simulate the motion of two immiscible fluids in the porous media with 2D realistic geometries and fractured media.

Chapter 4

Immiscible Two-Phase Displacement in Two-Dimensional Berea Sandstone

In this chapter, we will first validate the accuracy of our model by comparing the numerical results with the analytical solution. Then, we will investigate the colour gradient two-phase LBM for simulating the oil and water dynamics within a realistic 2D porous geometry. The effects of several parameters will be unraveled systematically in the subsequent sections.

4.1 Dynamic validation: capillary filling

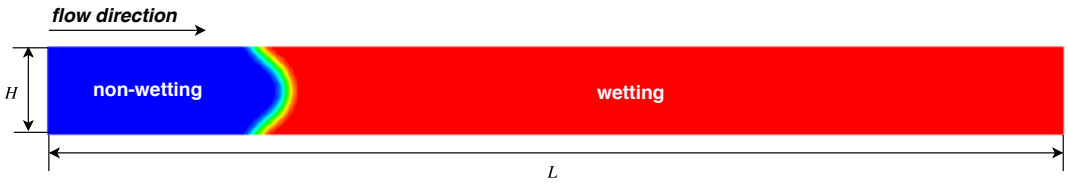

Figure 4.1: Simulation set-up for capillary filling. The length of the capillary tube is L and the width is H. The blue fluid is the displacing fluid (nonwetting) and the red fluid is the displaced fluid (wetting).

In this section, we concentrate on the capillary filling dynamics which has a moving

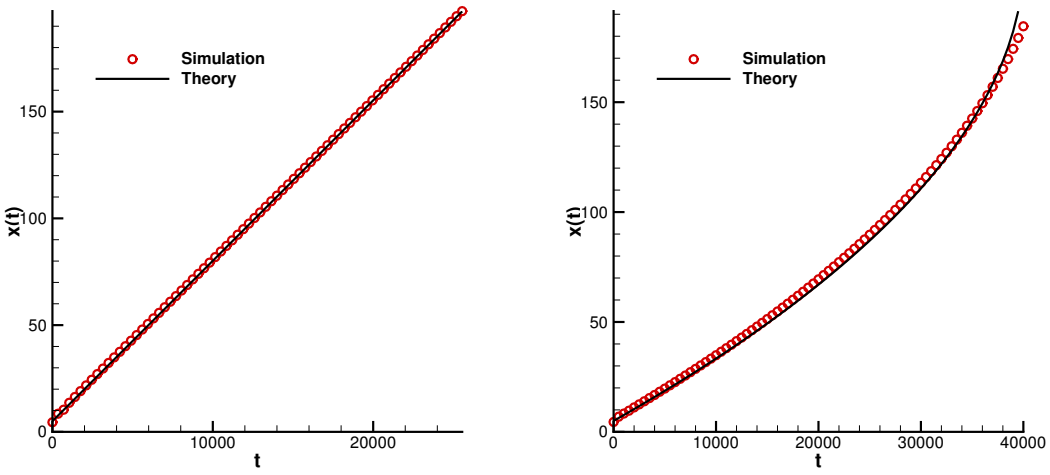

(a) $\lambda = 1$ (b) $\lambda = 10$

Figure 4.2: The length of the tube occupied by the filling fluid as a function of time for drainage with (a)$\lambda = 1$ and (b)$\lambda = 10$. The (red) open circles represent simulation results and the (black) solid lines are theoretical predictions based on Eqn. 4.1.

interface. The nonwetting (blue) fluid is injected to displace the wetting (red) fluid under a constant pressure difference as shown in Fig. 4.1. Assuming that the gravity and inertial effects can be neglected, the balance between the pressure difference over the interface, the Laplace pressure and the viscous drag of the fluid column gives the position of the fluid interface x in the capillary with time t

$$\frac{12}{H^2}\left[\eta_B x + \eta_R(L-x)\right] \cdot \frac{dx}{dt} = p_{in} - p_{out} - \frac{2\sigma cos\theta}{H}, \tag{4.1}$$

where H is the capillary tube width, x is the position of the phase interface, η_R and η_B are the dynamic viscosities of the red (wetting) and blue (nonwetting) fluids, L is the length of the capillary tube, p_{in} and p_{out} are pressures at the inlet and the outlet, σ is the interfacial tension coefficient and θ is dynamic contact angle between the wetting phase and the capillary measured from the simulation results [136]. The details of the derivation and solution to this equation are given in Appendix C.

The breakthrough time T_B can be derived by setting $x = L$, then we have

$$T_B = \frac{6L^2(\eta_R + \eta_B)}{H^2(p_{in} - p_{out} - \frac{2\sigma cos\theta}{H})}. \tag{4.2}$$

The simulation set-up consists of a 200×20 lattice domain with fixed pressure boundary condition of Zou and He [4] used in the x direction. On the solid walls, the bounce-back

rule is applied. Initially, the capillary tube is filled by the blue phase for $x <= 5$ and the red fluid for $x > 5$. The simulations are stopped when x reaches 196 to avoid the outlet effect. Thus the effective length of filling $x_e = 191$. And the simulations are run with the parameters $\rho_R = \rho_B = 1$. Two sets of simulations are conducted with different viscosity ratio λ, i.e., the ratio of dynamic viscosity between the defending and invading fluids here denoted as $\lambda = \mu_R/\mu_B$.

Figure 4.2 compares the simulation results to the analytical solution of Eqn. 4.1. The open circles represent the simulation results and the solid line shows the theoretically expected profile based on the numerically measured contact angle and the effective length of filling. It can be seen that in the drainage case (a), location of the interface in simulation is in very good agreement with the analytical solution. The error in breakthrough time for Case (a) is 0.4998%. In the drainage case (b), despite the interface in the simulation is slightly left behind than the analytical solution near the outlet, the breakthrough time error is -0.4838%. The error is calculated by $E\% = ((T_{B,simulation} - T_{B,theoretical})/T_{B,theoretical} \times 100\%)$.

4.2 Relative permeability validation: cocurrent flow in a 2D channel

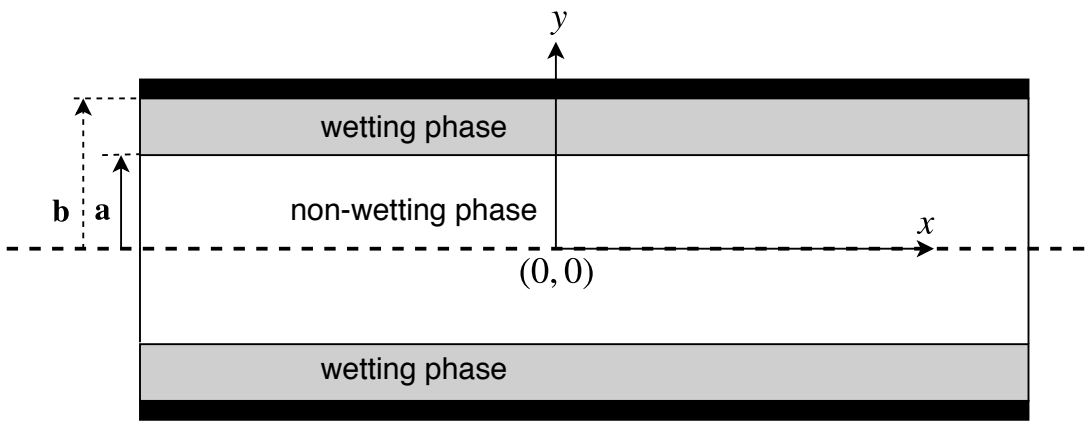

Figure 4.3: Schematic diagram for the cocurrent immiscible two-phase flow in a 2D channel. The wetting phase flows along the upper and lower solid walls, while nonwetting phase flows in the central region of the channel.

We first use the above model to simulate a pressure driven flow through a porous media. In the single-phase case, the intrinsic permeability K can be determined according to

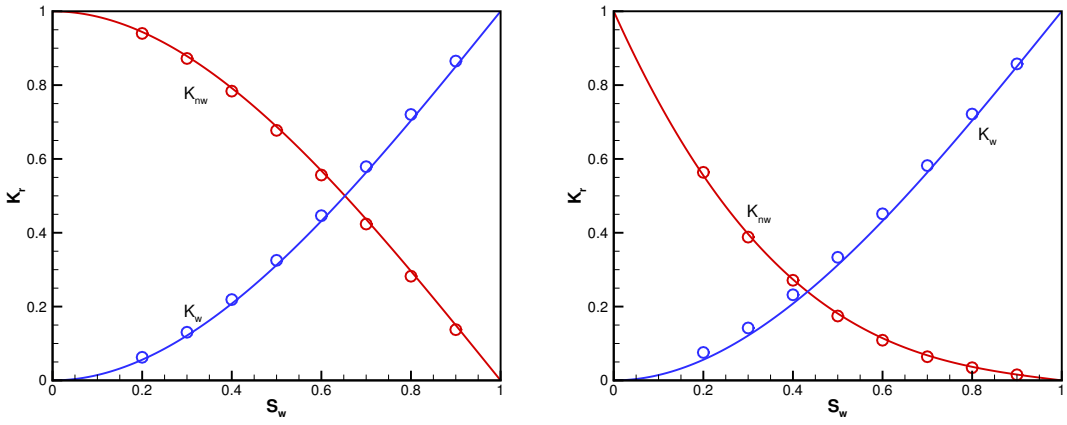

(a) $\lambda = 1$ (b) $\lambda = 0.1$

Figure 4.4: Relative permeabilities as a function of wetting phase saturation for two-phase cocurrent flow in a 2D channel for (**a**) $\lambda = 1$ and (**b**) $\lambda = 0.1$. The open circles represent the simulation results, and the solid lines are the analytical solutions from Equation (4.5).

the Darcy's law [9]

$$\boldsymbol{u} = -\frac{K}{\mu}\boldsymbol{\nabla} P, \quad K = -\frac{\mu \boldsymbol{u}}{\boldsymbol{\nabla} P}, \tag{4.3}$$

where $\boldsymbol{u}$ is the Darcy velocity in the porous medium. Note that the intrinsic permeability does not depend on the nature of the flow field but only on the geometry of the porous medium. In case of two-phase flows, the relative permeability $K_{r,i}$ can be given as [9]

$$\boldsymbol{u}_i = \frac{K K_{r,i}}{\mu_i}\boldsymbol{\nabla} P_i, \quad K_{r,i} = \frac{\mu_i \boldsymbol{u}_i}{K \boldsymbol{\nabla} P_i}, \quad i = w, nw. \tag{4.4}$$

Here, $i = w$ and nw refer to the wetting and nonwetting fluids respectively, μ_i is the dynamic viscosity of fluid i, and $\boldsymbol{\nabla} P_i$ is the pressure gradient of fluid i. We test whether the LBM model can accurately predict relative permeability for a simple immiscible two-phase cocurrent flow. Specifically, we calculate the relative permeabilities of the layered two-phase flow in a channel under different saturation values. In the simulation, a constant pressure difference is applied on the inlet and outlet boundaries following Zou and He [4], and a non-slip (bounce-back) boundary condition is applied on the upper and lower walls using the halfway bounce-back scheme. As shown in Fig. 4.3, the wetting phase flows along the walls ($a < |y| < b$) and nonwetting phase flows in the central region ($|y| < a$). One can obtain the analytical solutions for the relative

permeability, a function of wetting phase saturation S_w and viscosity ratio λ [137],

$$K_{r,nw} = (1 - S_w)\left[\frac{3}{2}\lambda + (1 - S_w)^2(1 - \frac{3}{2}\lambda)\right], \quad K_{r,w} = \frac{1}{2}S_w^2(3 - S_w), \tag{4.5}$$

where S_w is the wetting phase saturation, which is defined as $S_w = 1 - a/b$, and λ is the viscosity ratio of the nonwetting to wetting fluids, i.e., $\lambda = \mu_{nw}/\mu_w$.

For two typical viscosity ratios of $\lambda = 1$ and $\lambda = 0.1$, Figure 4.4 shows excellent agreement between the computed relative permeabilities and the analytical solutions.

4.3 Results and discussion

This section presents a systematic investigation on a pressure-driven immiscible two-phase flow in a 2D micromodel extracted from Boek et al. [138], which was engineered at Schlumberger Cambridge Research based on a thin section of a 3D Berea sandstone

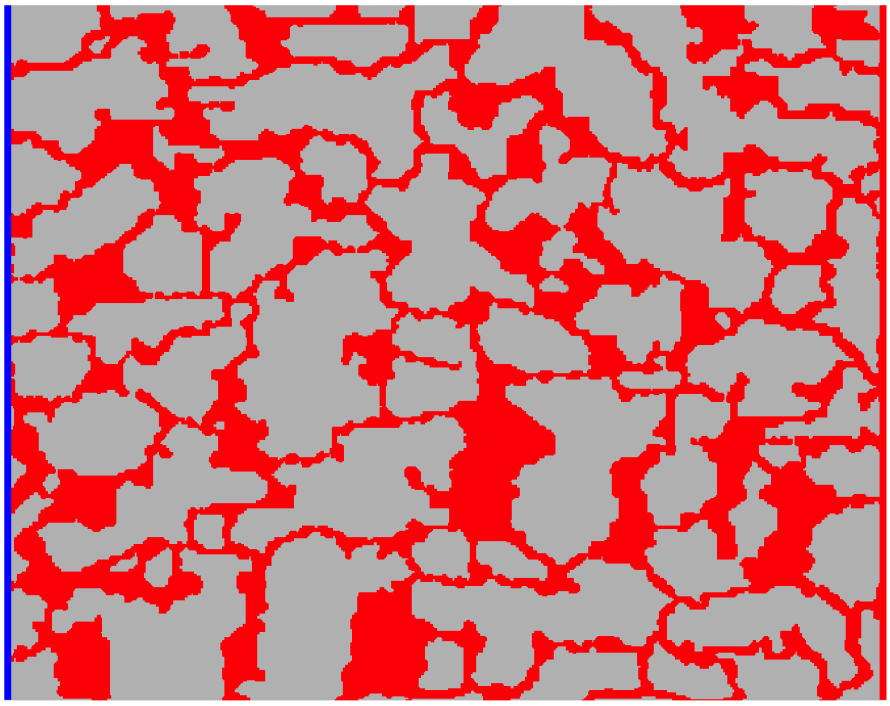

Figure 4.5: The 2D pore network used in the present lattice Boltzmann method simulations. The solid grains are represented in gray, while the displacing and displaced fluids are represented in blue and red, respectively. The domain size is 1774 μm by 1418 μm.

rock sample. We defined the lattice units for length, mass and time as lu, mu, and ts, respectively. To match the parameters in the lattice unit towards their physical values, three basic physical quantities are chosen as the reference values: the length scale (l_0), the mass scale (m_0) and the time scale (t_0). In the present study, $l_0 = 8 \times 10^{-6}$ m, $m_0 = 5.12 \times 10^{-13}$ kg, and $t_0 = 7.2 \times 10^{-7}$ s. Therefore, the density can be obtained by $\rho^{phy} = \rho \frac{m_0}{l_0^3} = \frac{5.12 \times 10^{-13}}{(8 \times 10^{-6})^3} = 10^3$ kg/m^3, the dynamic viscosity by ${\eta_{displaced}}^{phy} = \eta_{displaced} \frac{m_0}{l_0 t_0} = 0.167 \times \frac{5.12 \times 10^{-13}}{8 \times 10^{-6} \times 7.2 \times 10^{-7}} = 0.0148$ Pa·s, and the interfacial tension by $\sigma^{phy} = \sigma m_0 / {t_0}^2$. More details about the unit conversion can be found in Appendix 2.5.1.5. For the interfacial tension values used in the present work, the corresponding physical values for 0.03 mu·ts^{-2}, 0.015 mu·ts^{-2}, and 0.0005 mu·ts^{-2} are 0.0296 N·m^{-1}, 0.0148 N·m^{-1}, and 0.0004938 N·m^{-1}, respectively. However, using a time scale of t_0 means that about 1 million iterations are needed to simulate 1 second of physical time in a physical system, imposing limitations on the physical size or physical time that can be simulated.

Crude oil has a wide range of dynamic viscosity in nature varying with different compositions, temperature and pressure, etc. Thus it is reasonable to consider that the dynamic viscosity of the displaced fluid (crude oil) is 0.167 mu lu^{-1} ts^{-1} (0.0148 Pa· s). The dynamic viscosity of water is 8.9×10^{-4} Pa· s under room temperature, the resulted viscosity ratio between the displaced and invading fluid is 16.6 which is within the range of 1-50. This validates the practicality of the simulation.

4.3.1 Problem statement

The 2D micromodel is shown in Fig. 4.5, and its porosity is 0.33. The entire micromodel is divided into $L \times H = 2644 \times 2117$ lu^2 with a resolution of 0.67 μm per lu. The narrowest throat has a width of 12 lu which is fine enough to produce grid-independent results in two-phase displacement simulations [44]. Twenty-two extra layers of lattices are added to both the inlet and outlet to facilitate the implementation of boundary conditions and to act as NWP and WP reservoirs respectively, so the actual domain size is 2688×2117 lu^2. Here, the flow velocity for each fluid is so small that the inertial effect becomes insignificant.

The constant pressure boundary condition developed by Zou and He [4] is imposed at the inlet and outlet, which are located at the left and right sides of the domain, respectively. The halfway bounce-back scheme and wetting boundary condition are applied at the walls that contain the surfaces of solid grains as well as the upper and lower edges of the domain. The densities of both wetting and nonwetting fluids are

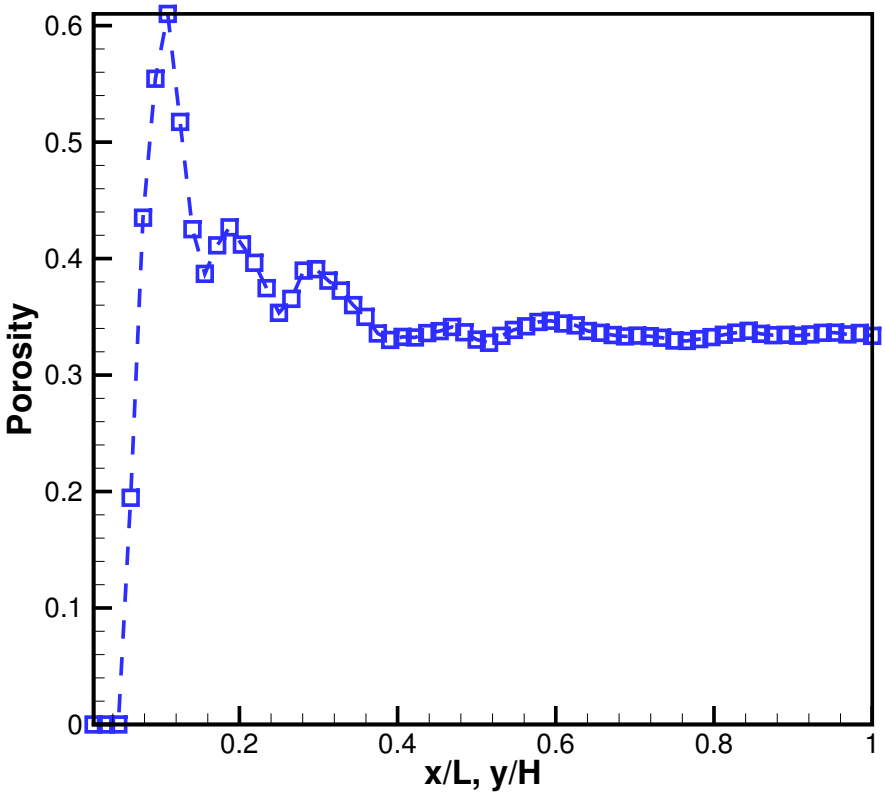

Figure 4.6: Porosity as a function of the domain size. L is the length of the entire micromodel, while H is its width; x refers to the distance to the left boundary, and y is the distance to the bottom boundary. For each point shown above, the same scaling is applied to x and y, i.e. $x/L = y/H$.

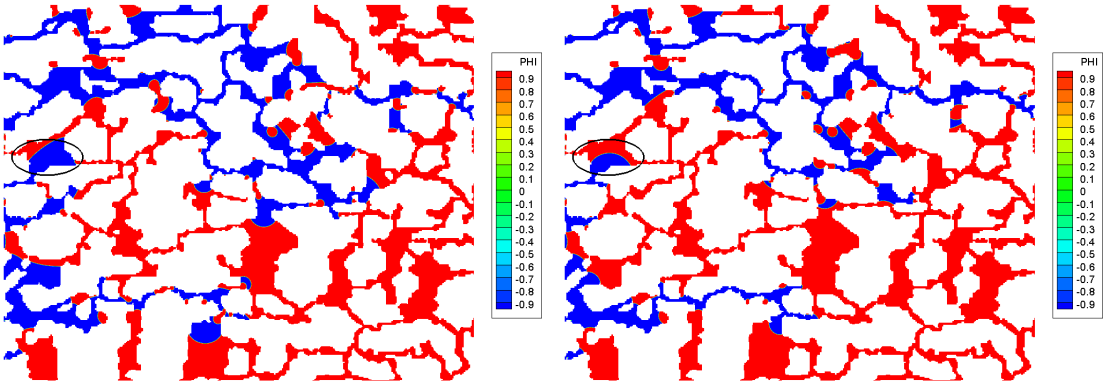

(a) $\lambda = 1$ (b) $\lambda = 2$

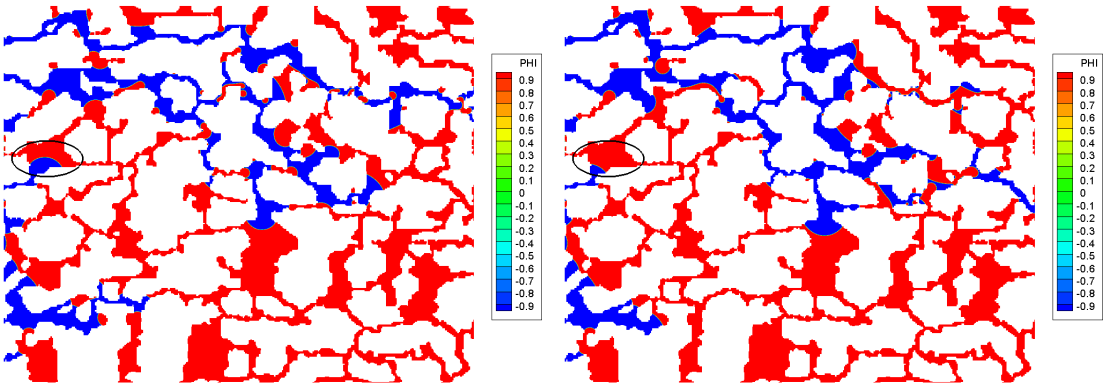

(c) $\lambda = 5$ (d) $\lambda = 10$

Figure 4.7: Fluid distributions at breakthrough for a wetting fluid invading a porous medium initially saturated with a nonwetting fluid. The wetting fluid (indicated in blue) is injected from the left side, and the viscosity ratio λ equals to 1, 2, 5, and 10, respectively.

set to be unity as the density difference between oil and water is insignificant. The dynamic viscosity of the displaced fluid is kept as 0.167 mu·lu^{-1}·ts^{-1}, and the dynamic viscosity of the displacing fluid is varied to achieve different viscosity ratio values ($\lambda = \eta_{displaced}/\eta_{invading}$). Initially, for $x \geq 22$ lu, the domain is filled with the displaced fluid (represented in red) at rest, and a constant pressure $p_{out} = 1/3$ mu·lu^{-1}·ts^{-2} is imposed at the outlet, while for $x < 22$ lu, the region is occupied by the displacing fluid (represented in blue) with a higher pressure at the inlet. The simulations are stopped when the displacing fluid breaks through at the outlet to avoid the capillary end effect[1] in the finite-sized computational domain [139].

By studying the dependency of porosity on the size of the rock sample, we calculated the porosity using different sizes of Berea sandstone to find its representative elementary volume (REV). The results are shown in Figure 4.6, which demonstrates that the chosen size of 2688×2117 lu^2 could be a good REV of the Berea sandstone. This guarantees that the simulated geometry included a sufficient number of pores for the meaningful statistical average, which is generally required by the continuum concept [9].

4.3.2 The viscosity ratio effect

The viscosity ratio is one of the most important dimensionless numbers in two-phase displacement through a porous media, and its effect is studied for a constant contact angle of 120°, corresponding to a weak wetting property of the displacing fluid. The inlet pressure is also the same for different viscosity ratios, i.e. $p_{in} = (p_{out} + 0.0125)$ mu·lu^{-1}·ts^{-2}. Figure 4.7 shows the fluid distributions inside the pore network when breakthrough of the displacing fluid occurs for viscosity ratios of 1, 2, 5, and 10. It can

Table 4.1: Parameters used in four typical cases of immiscible displacement.

Case	$\boldsymbol{\Delta P}$	$\boldsymbol{\sigma}$	$\boldsymbol{\cos\theta}$
I	0.0125	0.015	−0.5
II	0.0125	0.0005	−0.5
III	0.0125	0.0005	0.5
IV	0.0125	0.015	0.5

be seen that for these viscosity ratios considered, two or three preferential paths are generally formed. As the viscosity ratio increases, it becomes harder for the finger to flow into the large pore as highlighted by the black elliptical circles due to lower viscous pressure from the invading fluid. The front of the bottom finger is finally halted at the

[1]Due to the experimental/numerical setup, capillary end effects are commonly observed at the outlet as a result of the capillary jump generated by the discontinuity in the solid matrix at the interface between the rock sample and the outlet.

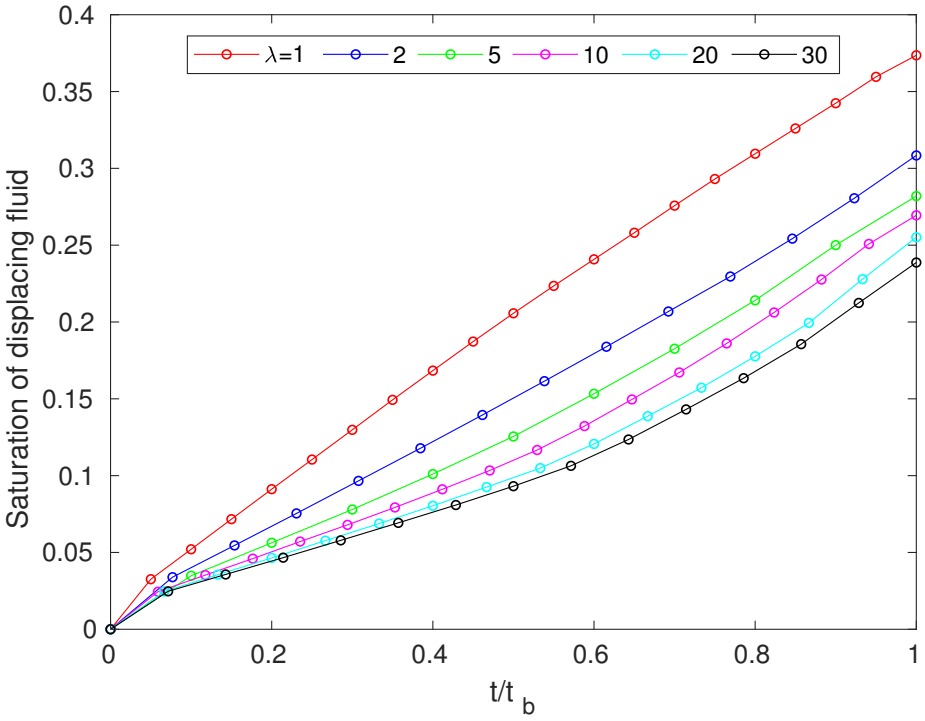

Figure 4.8: Evolution of the displacing fluid saturation for the viscosity ratio λ increased from 1 to 30 at $\sigma = 0.015$ mu·ts^{-2} and $\theta = 120°$ (imbibition). Note that the time step is normalized by t_b, defined as the time step at which the breakthrough occurs.

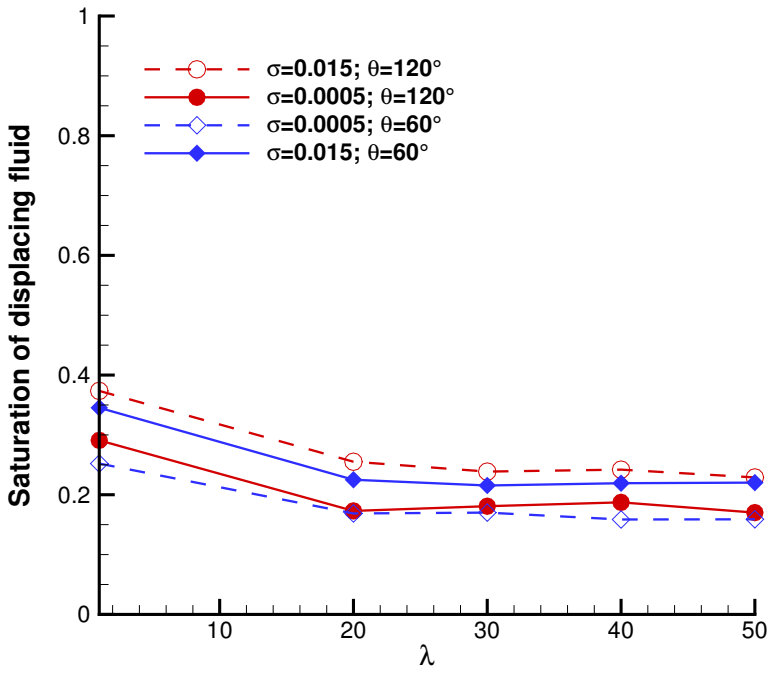

Figure 4.9: Displacing fluid saturation as a function of viscosity ratio for the four typical cases listed in Table 4.1.

position near the inlet for the viscosity ratio of 10 for the same reason. Also, the breakthrough finger switches to a lower position at the outlet when the viscosity ratio increases to 10.

Figure 4.8 shows the time evolution of the displacing (wetting) fluid saturation for viscosity ratio changing from 1 to 30. It can be clearly seen that a higher viscosity ratio results in a lower fluid saturation which is less favourable for the recovery of displaced fluid. This is consistent with previous experimental [2] and numerical results [140]. At the viscosity ratio of unity, the highest displacing fluid saturation (around 0.37) is observed, and the displacing fluid saturation keeps increasing linearly with time. Although the displacing fluid saturation reduces with λ, the reduction becomes less significant at larger λ values.

We also tested whether the above observations are valid for varying wettability and interfacial tension. Four pairs of contact angle and interfacial tension are considered (see Table 4.1), and the simulation results are shown in Figure 4.9. It is clear that the displacing fluid saturation drops rapidly when the viscosity ratio increases from 1 to 20 and then stays almost unchanged for all the cases considered. For each viscosity ratio, increasing contact angle or interfacial tension always leads to a higher displacing fluid saturation or displacement efficiency and the interfacial tension has a higher impact. In addition, the limitation of the current model is tested by decreasing the viscosity of the displacing fluid, and it is found that the maximum viscosity ratio that it can successfully access is as high as 50.

4.3.3 The interfacial tension effect

The interfacial tension between the displacing and displaced fluid is known to play an important role at the pore scale for two-phase displacement through a porous media. The same viscosity ratio ($\lambda = 1$) is used and the contact angle is fixed at 120°. Figure 4.10 shows the fluid distributions at breakthrough for the interfacial tensions of 0.03 mu·ts^{-2}, 0.015 mu·ts^{-2}, and 0.0005 mu·ts^{-2}. From this figure, it is seen that when the interfacial tension is as low as 0.0005 mu·ts^{-2}, the viscous force prevails, the main fingers get thinner and even break up, and many fingers only occupy partial pores or throats that they pass by. Also a number of small blobs of displaced fluid are left behind at low levels of interfacial tension. When the interfacial tension increases to 0.015 mu·ts^{-2}, larger blobs of the displaced fluid are trapped by the displacing fluid, and the displacing fluid flows into the large pore more easily due to higher capillary pressure, as highlighted by the black elliptical circles in Figure 4.10. As the interfacial

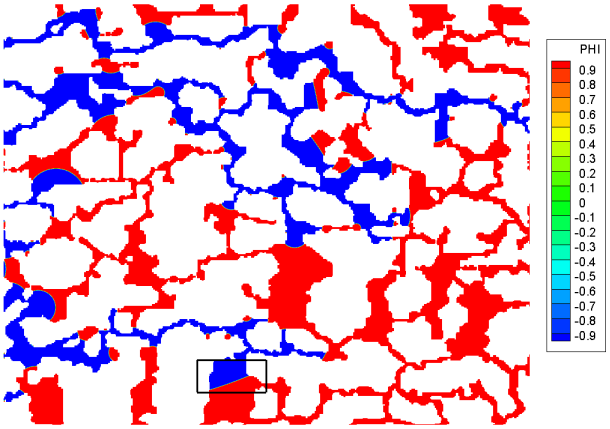

(a) $\sigma = 0.03$

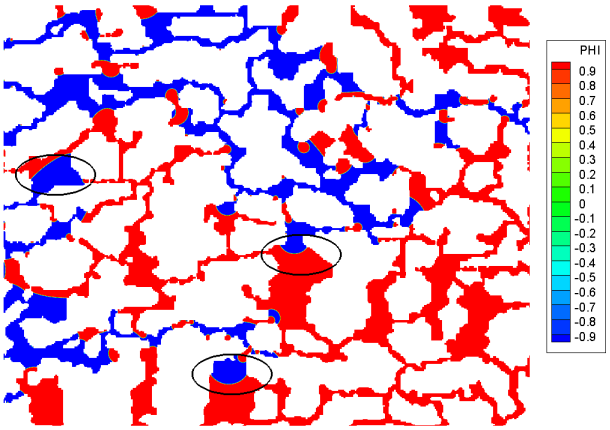

(b) $\sigma = 0.015$

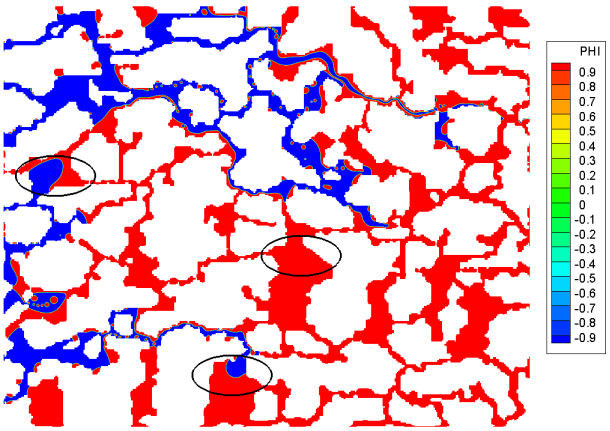

(c) $\sigma = 0.0005$

Figure 4.10: Fluid distributions at breakthrough for a wetting fluid invading a porous medium initially saturated with a nonwetting fluid. The wetting fluid (indicated in blue) is injected from the left side and the values of the interfacial tension are 0.03 mu·ts^{-2}, 0.015 mu·ts^{-2}, and 0.0005 mu·ts^{-2} from the top to bottom.

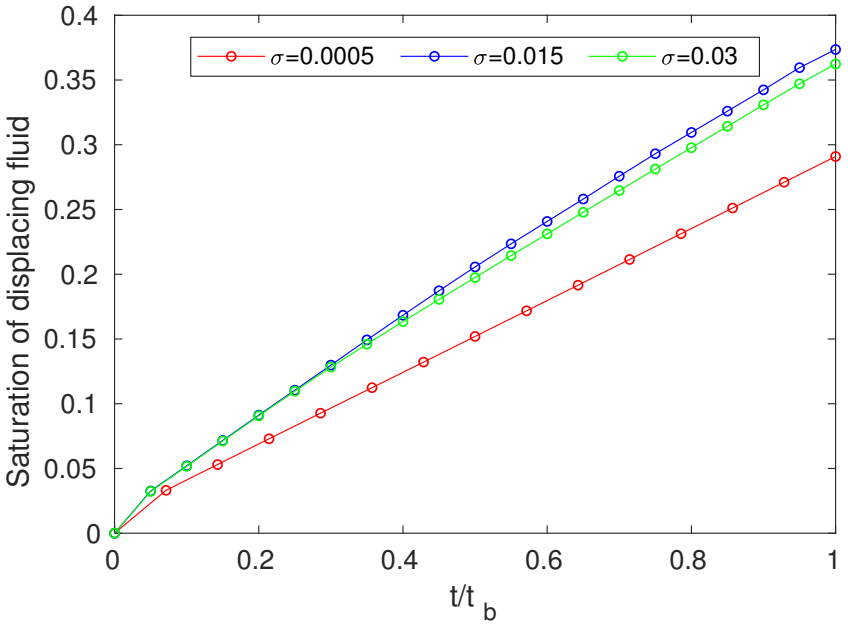

Figure 4.11: Evolution of the displacing fluid saturation for the interfacial tension of 0.0005 mu·ts^{-2}, 0.015 mu·ts^{-2} and 0.03 mu·ts^{-2}.

tension is further increased to 0.03 mu·ts^{-2}, we surprisingly found that the front of the displacing fluid can be flat inside some pores, e.g., the one surrounded by the black rectangle box in Figure 4.10, though most interfaces remain curved due to large capillary pressure. Meanwhile, much less of the displaced phase is left behind as the invading phase tends to occupy the pore body completely before reaching a neighbouring pore.

Figure 4.11 shows the evolution of the displacing fluid saturation for an interfacial tension of 0.0005 mu·ts^{-2}, 0.015 mu·ts^{-2} and 0.03 mu·ts^{-2}. It is seen that generally higher interfacial tension results in a higher saturation. The linear relationship between saturation and the evolving time is again observed.

4.3.4 The contact angle effect

The contact angle is measured from the displaced fluid. All the contact angles are larger than 90° in this part to simulate the imbibition process.

Figure 4.12 shows the fluid distributions when the displacing fluid breaks through at the outlet for the contact angles of 162°, 150°, 135°, and 120°. The contact angle is chosen as any value larger than 90° to simulate imbibition. Recent studies have shown that contact angles vary pore by pore as a result of wettability alteration by

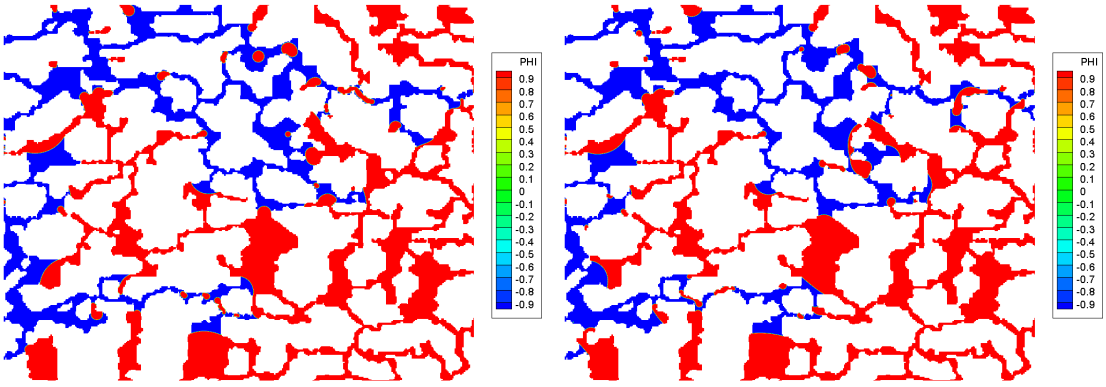

(a) $\theta = 162^\circ$ (b) $\theta = 150^\circ$

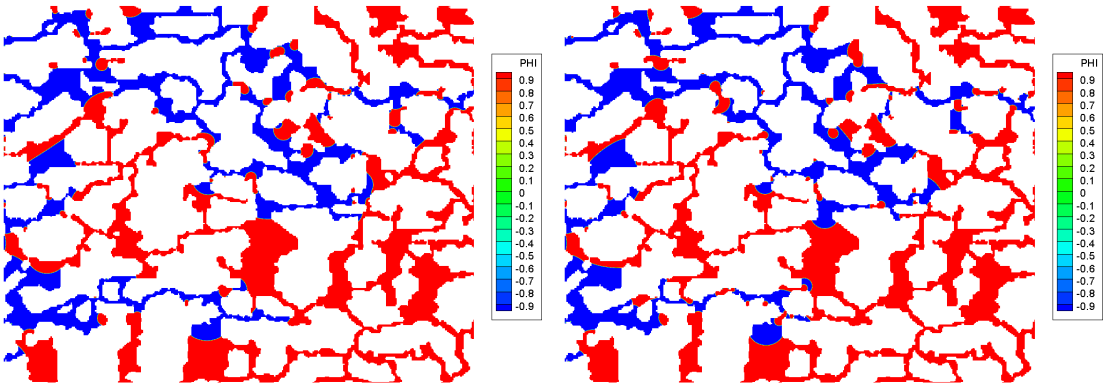

(c) $\theta = 135^\circ$ (d) $\theta = 120^\circ$

Figure 4.12: Fluid distributions at breakthrough for a wetting fluid invading a porous medium initially saturated with a nonwetting fluid. The wetting fluid (indicated in blue) is injected from the left side and the values of the contact angle are 162°, 150°, 135°, and 120°, respectively.

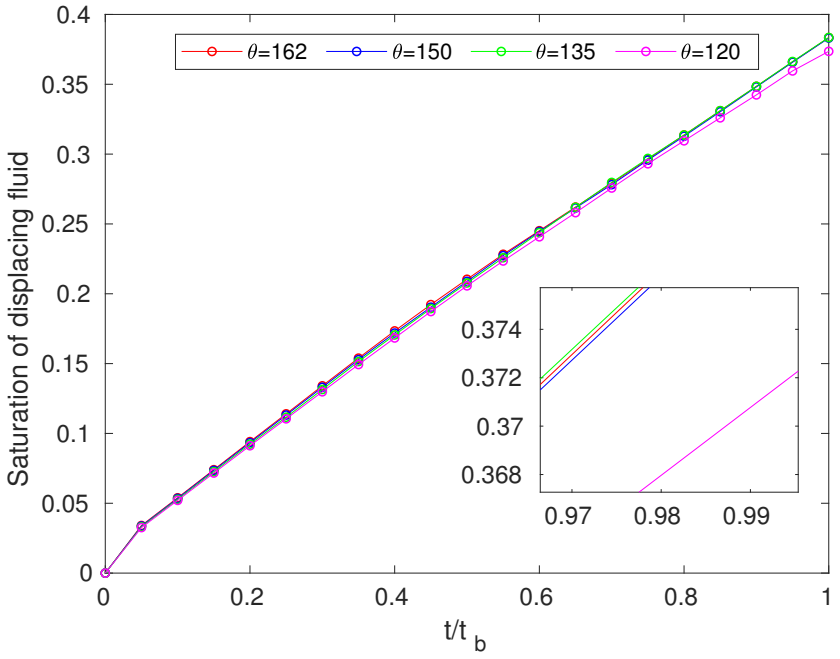

Figure 4.13: Evolution of the displacing fluid saturation for contact angles of 162°, 150°, 135°, and 120°.

the sorption of surface active compounds in crude oil [141]. Hence it is still not fully understood how this surface wettability condition affects oil recovery. As a preliminary study we apply same contact angle in each pore within this thesis however it is desirable to investigate further, e.g., the effect of mixed wettability, contact angle hysteresis etc in future as the wettability significantly affects the darcy scale multiphase flow [142]. It is observed that the invading paths of the wetting fluid do not change significantly except for a few branches. An obvious difference can be seen at the contact angle of 135° where the bottom finger advances furthermost. Figure 4.13 shows the evolution of the displacing fluid for different contact angles. The case of $\theta = 120°$ has the lowest wetting fluid saturation but its difference from the others is very small. It can also be seen from Figure 4.9 that the contact angle does not have a big impact on the saturation. Therefore, the contact angle has a limited effect on the efficiency of displacement in the micro-model of Berea sanstone.

4.4 Conclusions

The colour gradient two-phase LBM is used to study dynamic displacement of immiscible fluids in a 2D micromodel of Berea sandstone. The effects of the viscosity ratio,

interfacial tension, and contact angle on the fluid distributions at breakthrough and the evolution of displacing fluid saturation are systematically investigated. When the viscosity ratio is no more than 20, a higher viscosity ratio results in a lower displacing fluid saturation which is less favourable for the recovery of the displaced fluid. However, when the viscosity ratio is larger than 20, the saturation is almost constant for both imbibition and drainage, regardless of the interfacial tension. At the viscosity ratio of unity, the displacing fluid saturation has the highest value, and it linearly increases with time.

The interfacial tension affects the flow pattern. When the interfacial tension is as low as 0.0005 mu·ts^{-2}, thin viscous fingers appear. A number of small drops of displaced fluid are left behind. As the interfacial tension increases from 0.0005 mu·ts^{-2} to 0.015 mu·ts^{-2}, the size of the trapped blobs increases, and the number decreases. The displacing fluid flows into large pores more easily due to the increased capillary pressure. When the interfacial tension continues to increase, smaller amount of the displaced phase is left behind as the invading phase tends to occupy the pore body completely before reaching a neighbouring pore. In addition, increasing interfacial tension results in a higher saturation of wetting fluid.

The contact angle generally does not change preferential flow paths except for a few branches in the imbibition, suggesting that the contact angle has limited effect on the efficiency of displacement within 2D Berea sandstone.

Chapter 5

Counter-current imbibition in strongly water-wet fractured porous media

In Chapter 4, a series of parameters have been used to investigate two immiscible fluids flow in a realistic 2D porous geometry, including different viscosity ratios, interfacial tensions, and contact angles. All of these parameters can affect fluid flow within fractured media as well.

In this Chapter, the colour gradient LBM is used to investigate the counter-current spontaneous imbibition mechanism in the fracture-matrix system. In Section 5.1, the Voronoi tessellation technique is used to construct the pore structure. In Section 5.2, the effect of water injection velocity, geometry configuration of the dual permeability zones, interfacial tension, viscosity ratio, and fracture spacing (only when multiple fractures are present) is systematically studied, and the sensitivity analysis is performed to find the optimal parameters that maximise the oil recovery. Three distinct imbibition regimes will be identified, characterized with different morphologies of expelled oil in the fracture.

5.1 Matrix construction

The matrix is constructed using a Voronoi tessellation technique where the pore structure is simplified as randomly connected throats. The throat widths are specified according to the log-normal distribution, which is found to be a good geometric ap-

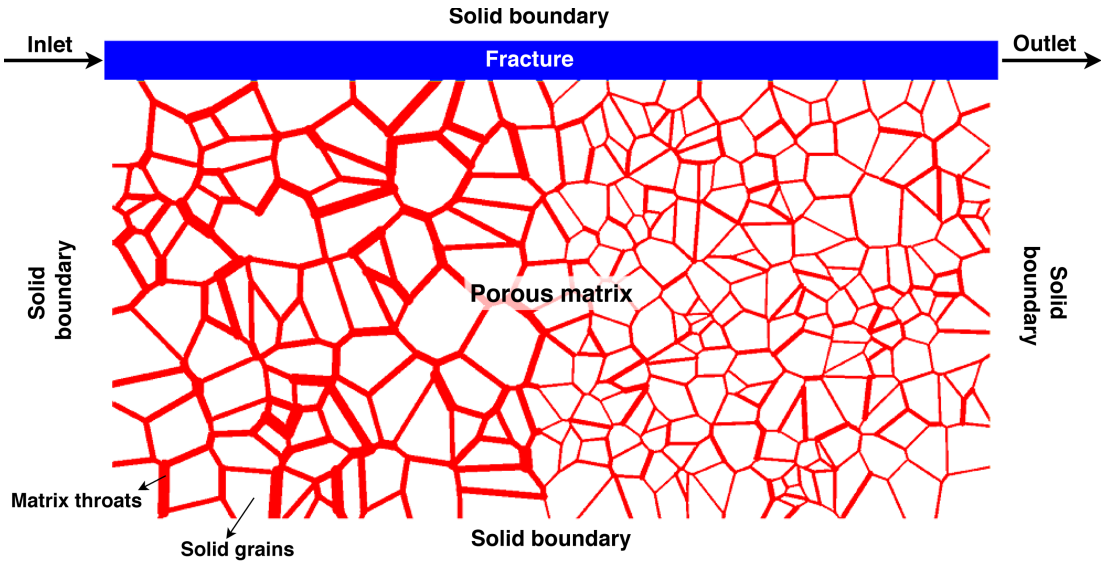

Figure 5.1: Schematic of the simulated geometry used for counter-current displacement of oil from a porous matrix by the wetting water. White color indicates the solid grains. The inlet and outlet are specified with arrows, and the matrix is initially saturated with oil (red colour) and the fracture with water (blue colour).

proximation to natural porous media in statistics [143]. Also, the matrix is constructed with two different permeability zones along the fracture as commonly encountered in multiplayer geological formations [129].

5.2 Results and discussion

In this section, we will analyse the effect of various factors on the counter-current spontaneous imbibition in matrix-fracture systems, which include the water injection velocity, interfacial tension, viscosity ratio, geometry configuration of the dual permeability zones and fracture spacing. In the following, we first present a detailed description of the problem, including the simulated geometries, boundary conditions, and the parameter setting.

Figure 5.1 illustrates the primary geometry investigated in this study. It is composed of a rectangular porous matrix and a single fracture with the same length attached on its top side. The matrix is constructed by randomly placed throats. The throat positions are generated by applying the Voronoi tessellation technique with randomly placed sites. Details of this algorithm are described in Debnath et al. [144]. To introduce the permeability heterogeneity in the matrix, the sites population density (or the number of throats) in the right-half domain is twice of that in the left-half domain. The pore

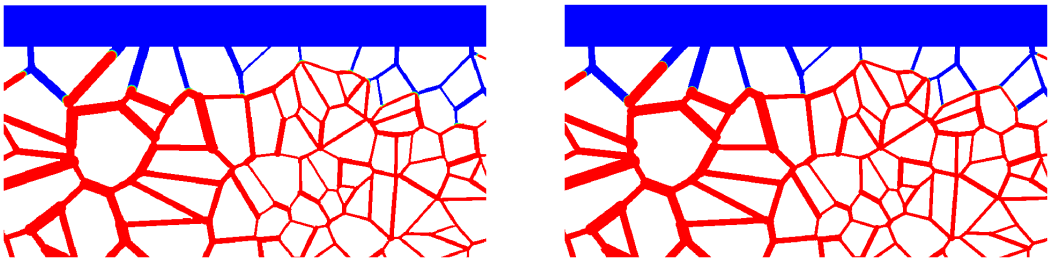

(a) (b)

Figure 5.2: Final fluid distribution in (a) the coarse grid and (b) the fine grid for $\lambda = 1$, $\sigma = 30$ mN/m and $u_{inj} = 5.6$ mm/s. The minimum throat width in the coarse grid is 4 lattices while in the fine grid it is 8 lattices. Note that the water and the oil are shown in blue and red respectively.

diameter and throat width in both half-domains follow a truncated log-normal distribution with $Lognormal(\mu, \sigma^2)$ ($\mu = 0, \sigma = 0.5$), where the variation range is specified by the minimum and maximum values [145]. The common statistic approximation for the throat widths in natural fractured porous media is the log-normal distribution [143]. The statistic average of the pore throat width in the left half of the domain is twice of that in the right half, yielding a dual-permeability porous matrix with high and low permeability zones. The resultant matrix porosity is 0.26. The length and width of the computing domain is $L = 13.44$ mm and $H = 7.2$ mm, which are divided into 1680 and 900 cells, respectively. The fracture width is $h = 0.6$ mm (75 lattices) and the minimum width of the pore throats is 32µm (4 lattices).

To obtain statistically meaningful results, we should apply sufficient number of lattices for the thinnest throat and simulate as many as possible pores and throats. With the restriction of the high-performance computer we can access to, we need to strike a balance on the computational efficiency and accuracy. Thus, it is important to minimize the grid number while necessary physics can be retained. Here we provide a test to examine the dependence of numerical results on the grid resolution. In order to minimize the computing resources, we take a slice of 6.888×3.600 mm^2 which incorporates the thinnest throats from the middle upper side of the primary geometry, i.e., "left-wide matrix" shown in Fig. 5.1. The simulation parameters are chosen as $\lambda = 1$, $\sigma = 30$ mN/m and $u_{inj} = 5.6$ mm/s (see later for the matrix configuration and parameter setting). Fig. 5.2(a) shows the final fluid distribution in the coarse grid with the thinnest throat width of 4 lattices and (b) shows the final fluid distribution in the fine grid with the thinnest throat width of 8 lattices. It is observed that the grid refinement only slightly affects the numerical results. The final oil saturation in the

matrix varies from 0.114 in the coarse grid to 0.113 in the fine grid, with a difference of 0.88%. This verifies that the coarse grid simulation with the thinnest throat width of 4 lattices can offer acceptable computational accuracy.

Initially, the fracture and the matrix are saturated with water and oil (denoted by blue and red in Fig. 5.1), respectively. Then water is continuously injected from the left inlet of the fracture with a constant velocity of u_{inj}, and the outlet pressure is set to be zero. Both water and the expelled oil flow out at the right end of the fracture. All the sides of the matrix are assumed to be solid walls, except for the top side, which is connected to the fracture. At the solid surfaces, no-slip boundary condition is imposed by using the half-way bounce-back scheme [146] and the desired contact angle is achieved by using the wetting boundary condition proposed by Xu et al. [69], which modifies the direction of the colour gradient $\boldsymbol{\nabla}\rho^N$ at the boundary to match the specified contact angle θ. These boundary conditions are to maintain a counter-current imbibition environment in which the oil in the matrix can only flow into the fracture that supplies water, which have been widely adopted in the previous numerical and experimental studies of counter-current imbibition [50, 55, 68, 147]. Among various factors that influence the capillary imbibition, surface wettability is of vital importance for both imbibition rate and ultimate oil recovery, and its effect has been thoroughly investigated by Rokhforouz and Amiri [50]. They found that, when the contact angle θ (measured from the water side) is greater than $\pi/4$, the oil recovery is negligible, but both the imbibition rate and the oil recovery drastically increase with decreasing contact angle when $\theta < \pi/4$. Similar findings are also demonstrated by the present simulations and the simulation results are shown in Appendix D, where the effect of surface wettability is studied for the contact angles varying from $\pi/10$ to $\pi/4$. Therefore, the porous matrix is considered strongly water-wet with $\theta = \pi/10$ in the following study.

For most pore-scale studies, the ratio of gravity to capillary forces is very small and thus the effects of density difference can be neglected [10]. In the LB simulations, the densities of both fluids are set to unity for the sake of simplicity. Five different water-oil viscosity ratios are considered, i.e. $\lambda = 0.1, 0.5, 1, 5$ and 10, and six different interface tensions are used, i.e. σ =5, 10, 15, 30, 45 and 60 mN/m. The water injection velocity at the inlet ranges from $u_{\text{inj}} = 0.075$ mm/s to 44.4 mm/s. Unless otherwise stated, the simulation parameters are chosen as $\lambda = 1$, $\sigma = 30$ mN/m and $u_{\text{inj}} = 5.6$ mm/s. For each case, the simulation is run until the saturation of water in the matrix reaches a constant value.

Apart from the primary geometry setup as illustrated in Fig. 5.1, we also consider several different geometries that are derived from it to study the effect of matrix geometry

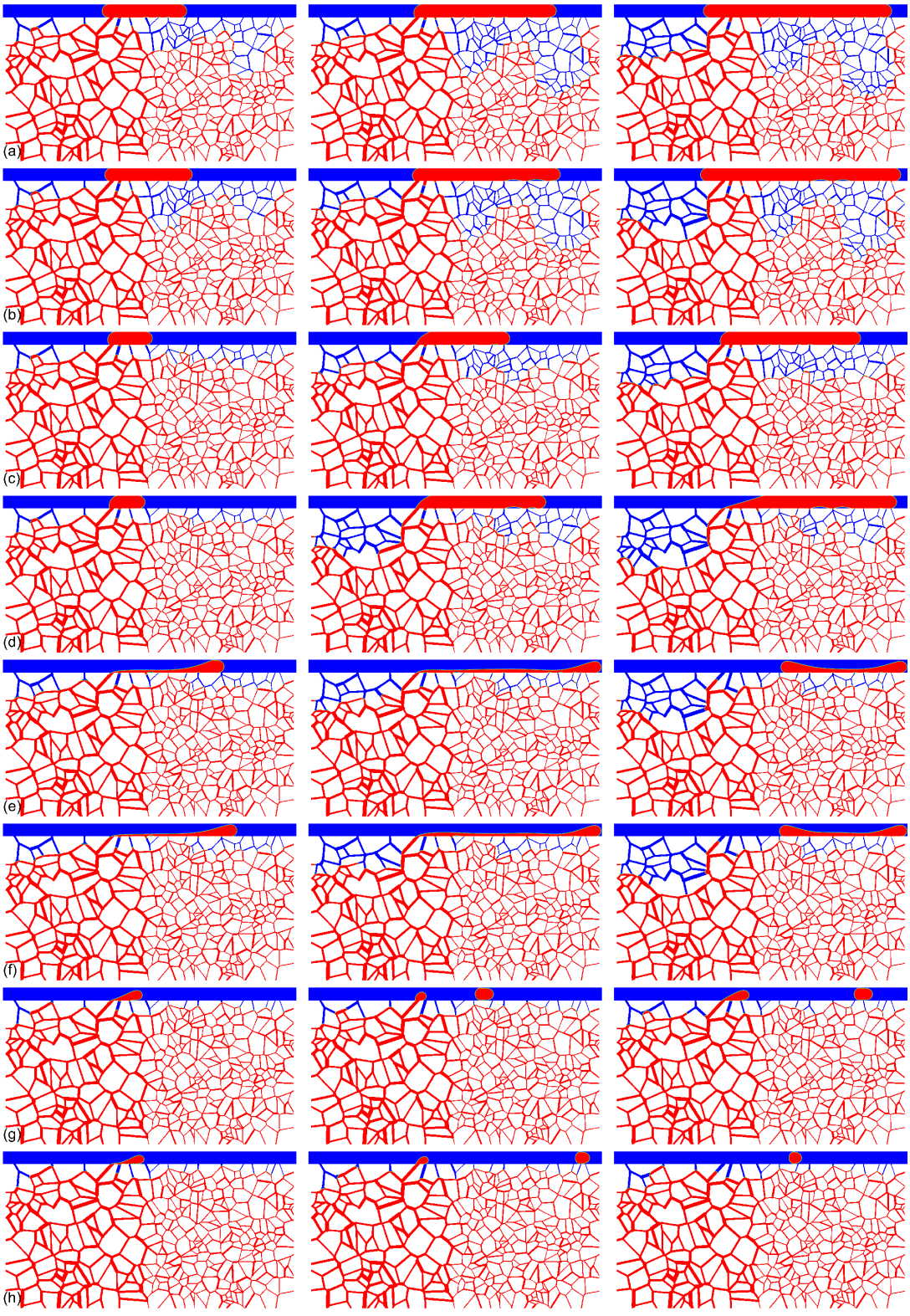

Figure 5.3: Snapshots of fluid distributions during imbibition for different injection velocities: (a) $u_{\text{inj}} = 0.075$ mm/s; (b) $u_{\text{inj}} = 0.11$ mm/s; (c) $u_{\text{inj}} = 0.56$ mm/s; (d) $u_{\text{inj}} = 1.11$ mm/s; (e) $u_{\text{inj}} = 4.44$ mm/s; (f) $u_{\text{inj}} = 5.56$ mm/s; (g) $u_{\text{inj}} = 22.22$ mm/s and (h) $u_{\text{inj}} = 44.44$ mm/s. Note that the water and the oil are shown in blue and red respectively.

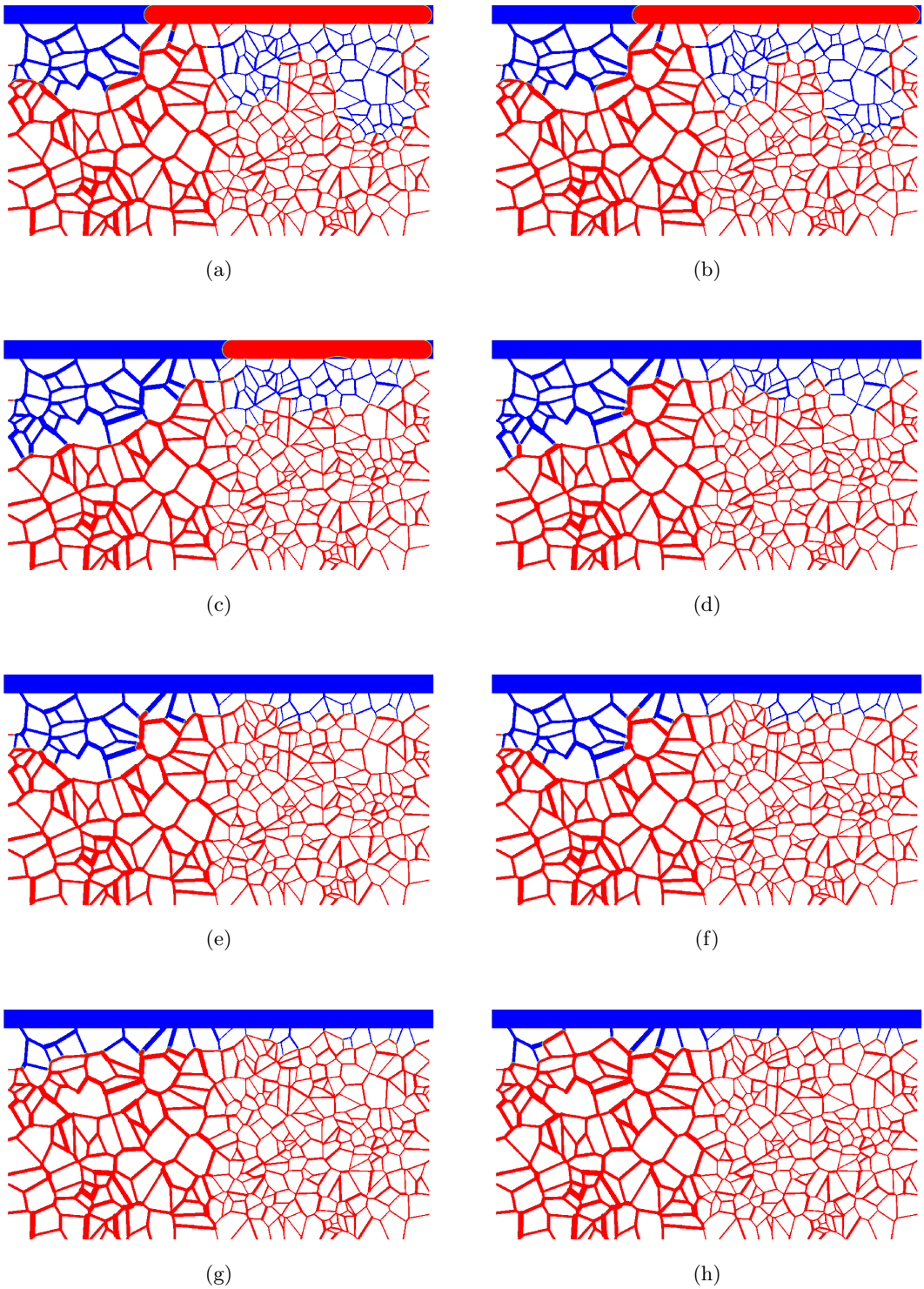

Figure 5.4: Fluid distributions at steady-state for different injection velocities: (a) $u_{\text{inj}} = 0.075$ mm/s; (b) $u_{\text{inj}} = 0.11$ mm/s; (c) $u_{\text{inj}} = 0.56$ mm/s; (d) $u_{\text{inj}} = 1.11$ mm/s; (e) $u_{\text{inj}} = 4.44$ mm/s; (f) $u_{\text{inj}} = 5.56$ mm/s; (g) $u_{\text{inj}} = 22.22$ mm/s and (h) $u_{\text{inj}} = 44.44$ mm/s. Note that the water and the oil are shown in blue and red respectively.

configuration and the interplay between imbibition and fluid transport in the fractures. The first variant is the mirrored one by reversing the matrix from left to right. The second variant is the two-fracture system by adding an additional horizontal fracture at various positions.

5.2.1 Effect of water injection velocity

The interaction of water with the matrix is strongly related to the rate of water injection [148] as the expelled oil accumulates and transports in the fracture. In order to investigate the effect of water injection velocity, eight numerical experiments with the injection velocities of 0.075, 0.11, 0.56, 1.11, 4.44, 5.56, 22.22 and 44.44 mm/s are conducted. In the LB model, the numerical values corresponding to these values are 6.75×10^{-6}, 1×10^{-5}, 5×10^{-5}, 1×10^{-4}, 4×10^{-4}, 5×10^{-4}, 2×10^{-3} and 4×10^{-3} lu/ts, respectively. These values are chosen for the sake of generality of the computational experiment.

Figure 5.3 shows snapshots of the fluid distributions for various injection velocities. It is observed that regardless of the water injection velocity, the oil selects the widest matrix throat connecting with the fracture to flow into the fracture, while water in the fracture imbibes into the matrix from the other narrower matrix throats. This is because the wider throat corresponding to the lower capillary pressure makes the water imbibition more difficult. Such a pattern was also observed by Gunde et al. [68] when they analyzed the counter-current imbibition in a fracture-matrix system where the porous matrix is composed of randomly placed square solid grains.

As more oil comes out of the matrix from the widest channel continuously, the oil accumulates locally to form either piston-like plug, elongated liquid thread, or isolated drops, depending on the water injection velocity. The water imbibition characteristics including the preferential path and the imbibition depth also change significantly with the injection velocity. We will later discuss these differences from the perspective of different regimes.

When the oil cannot further move out from the matrix, we assume the imbibition has reached the steady-state. The fluid distributions at the steady-state for the eight different injection velocities are presented in Fig. 5.4. It shows the oil recovery factor and the imbibition depth overall increase as the water injection velocity decreases. For the present geometry, one would expect that the wetting fluid (water) will preferentially enter the narrowest neighboring throat due to its highest capillary pressure [149]. Such a trend is observed in the early stage, while in the late stage, the water front could

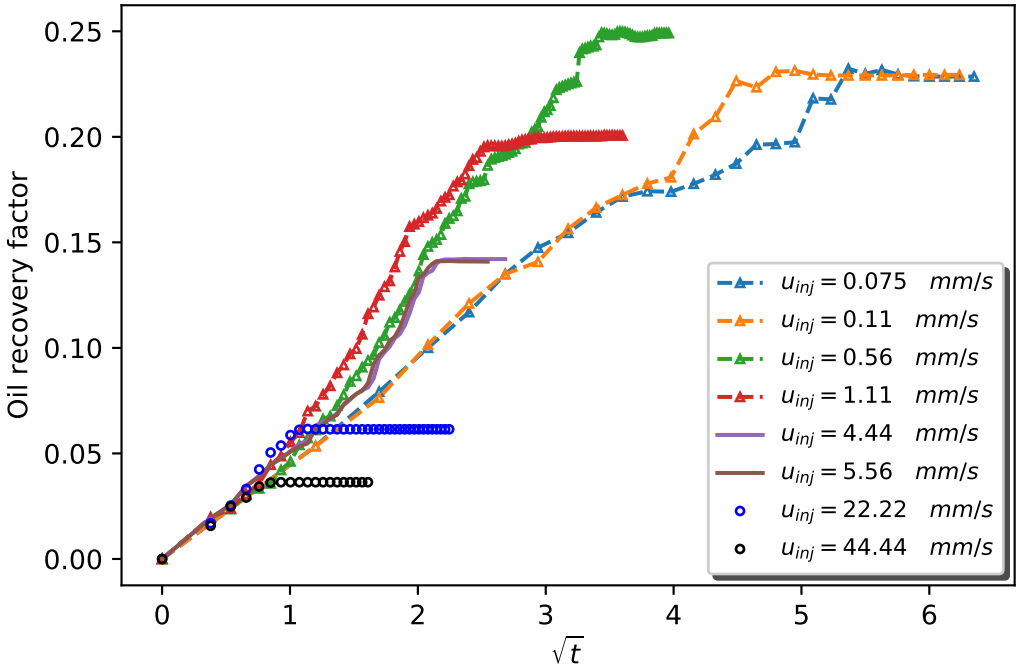

(a)

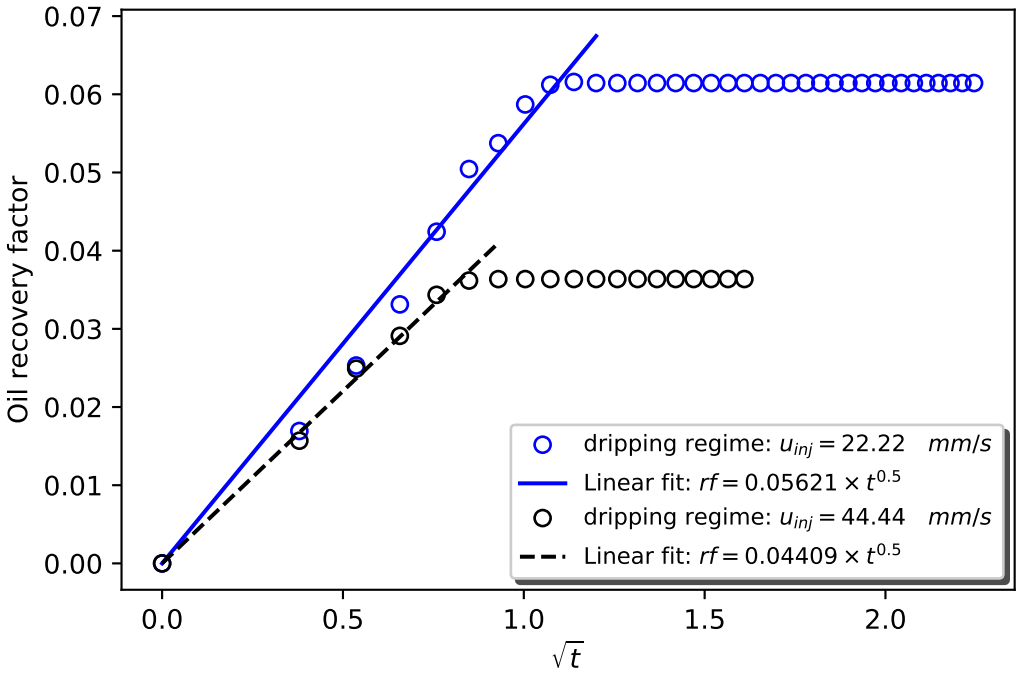

(b)

Figure 5.5: (a) Time evolution of the oil recovery factor for different injection velocities of 0.075 mm/s, 0.11 mm/s, 0.56 mm/s, 1.11 mm/s, 4.44 mm/s, 5.56 mm/s, 22.22 mm/s and 44.44 mm/s; (b) The magnified illustration of the oil recovery factor evolution in the dripping regime.

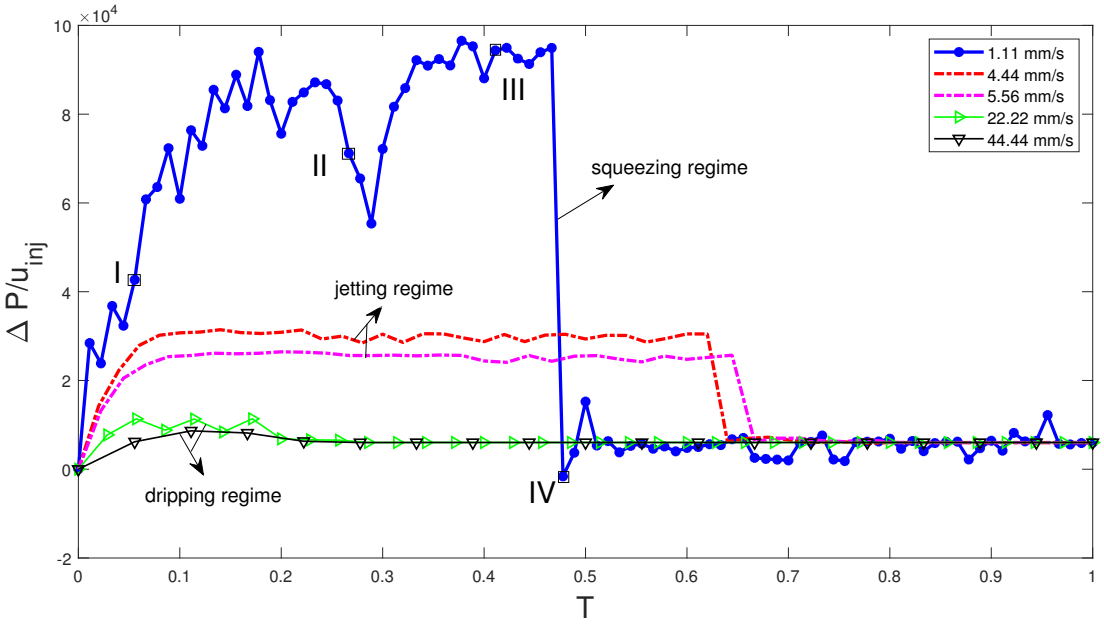

Figure 5.6: Time evolution of the pressure difference (which is scaled against the water injection velocity u_{inj}) between the upstream and outlet in the fracture for three typical regimes. Blue lines with solid circles correspond to the case shown in Fig. 5.3(d) (the squeezing regime), the dashed red and magenta lines correspond to Fig. 5.3(e) and (f) (the jetting regime), and the green and black lines with open triangles correspond to Fig. 5.3(g) and (h) (the dripping regime). The black squares labelled I, II and III correspond to the three snapshots shown in Fig. 5.3(d), while IV represents the instant at which the widest matrix throat connected with the fracture being invaded by water. The dimensionless time T is defined by $T = t/t_s$ where t_s is the time of reaching the steady state. The values of t_s are 12.96s, 7.2s, 6.48s, 5.04s and 2.59s for Fig. 5.3(d)-(h).

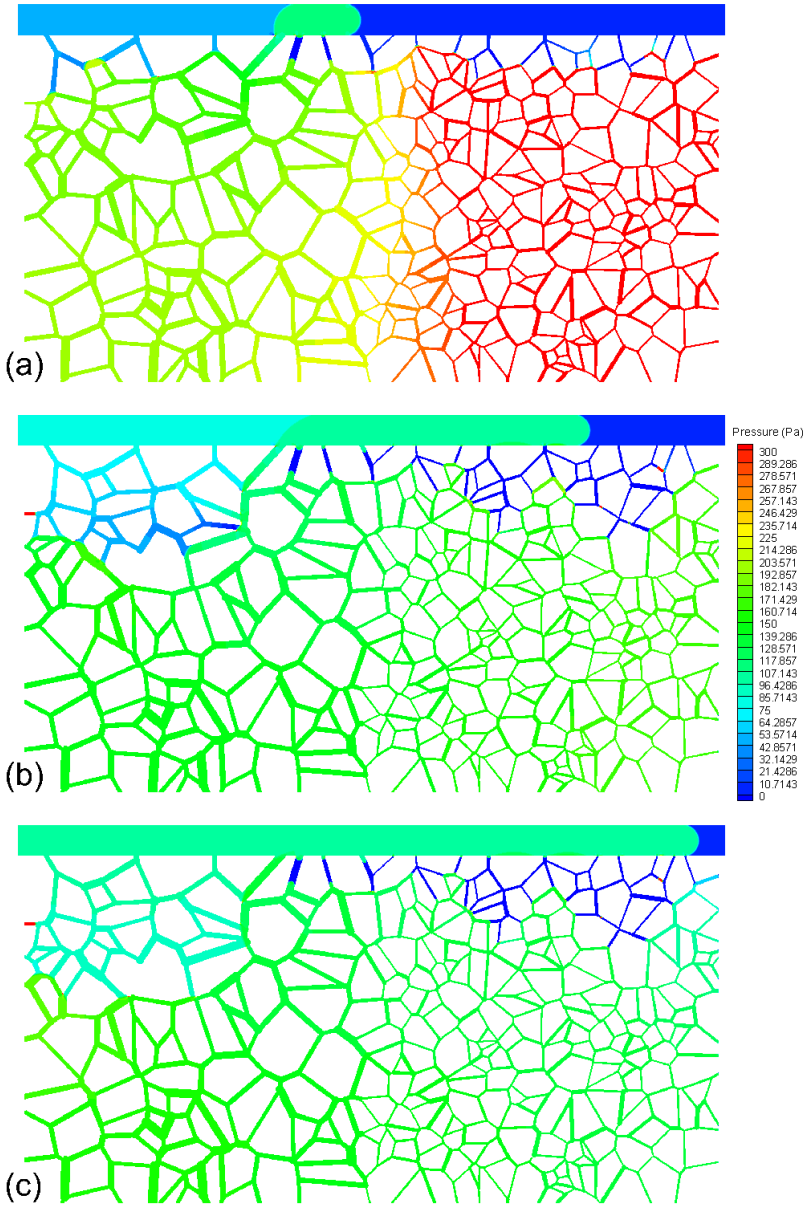

Figure 5.7: The distributions of pressure (difference to the outlet pressure) at the times of (a) t=0.72s; (b) t=3.46s and (c) t=5.33s, which correspond to the three snapshots shown in Fig. 5.3(d).

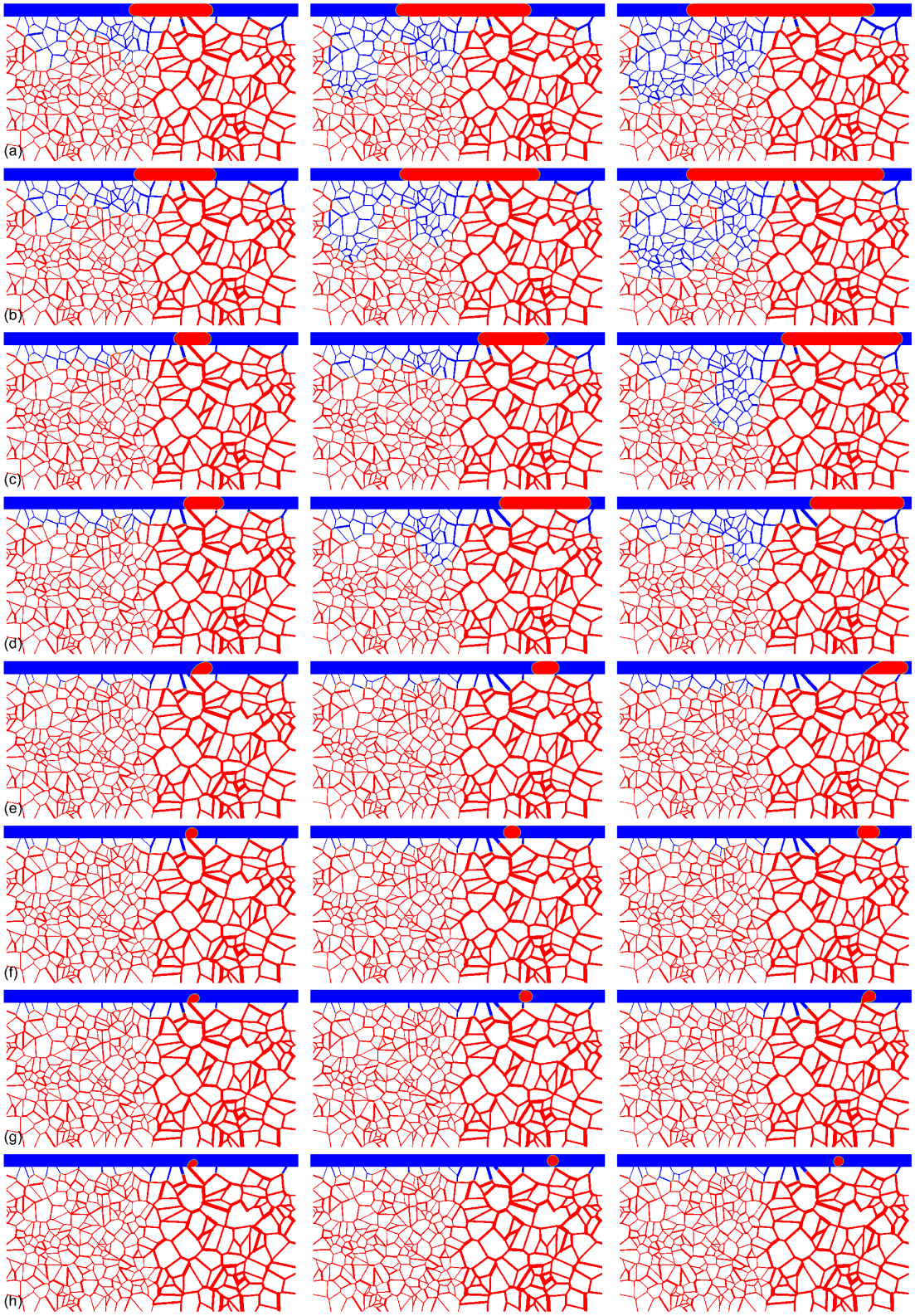

Figure 5.8: Snapshots of fluid distributions during imbibition in the right-wide matrix for different injection velocities: (a) $u_{\text{inj}} = 0.075$ mm/s; (b) $u_{\text{inj}} = 0.11$ mm/s; (c) $u_{\text{inj}} = 0.56$ mm/s; (d) $u_{\text{inj}} = 1.11$ mm/s; (e) $u_{\text{inj}} = 4.44$ mm/s; (f) $u_{\text{inj}} = 5.56$ mm/s; (g) $u_{\text{inj}} = 22.22$ mm/s and (h) $u_{\text{inj}} = 44.44$ mm/s. Note that the water and the oil are shown in blue and red respectively.

invade the matrix further in the left-half region where the throat width is larger [see Fig. 5.4(c)-(f)]. Again, this will be discussed in more details later.

Based on the different morphologies of the expelled oil in the fracture, as shown in Fig. 5.3, we identified three different regimes: the squeezing regime when the expelled oil forms a piston-like plug and grows in the fracture [Fig. 5.3 (a) - (d)]; the dripping regime when the expelled oil forms isolated drops in the fracture [Fig. 5.3 (g) and (h)]; and the jetting regime where the expelled oil develops into a thin and elongated oil thread [Fig. 5.3 (e) and (f)]. It is noted that a similar regime classification was also performed in the studies of droplet formation using a microfluidic T-junction [150, 151, 152]. These three different regimes are analyzed below individually.

First, when the water injection velocity is small (typically varying from 0.075 mm/s to 1.11 mm/s), the squeezing regime occurs, where the expelled oil blobs form a continually growing plug in the fracture [Fig. 5.3 (a) - (d)]. The oil plug is big enough to entirely block water flowing through the fracture. As a result, the pressure builds up at the upstream of the oil plug as observed in the simulations. The increased pressure at the upstream forces water to advance into the left-half region of the matrix gradually from the upstream. At the same time, as the plug length increases, it blocks the imbibition of water into the narrower throats in the right-half region of the matrix. This mechanism explains why we observe the counterintuitive phenomenon that water advances further in the left-half region of the matrix which has wider throats, as shown in Fig. 5.4(c) and (d). For the extremely low water injection rate, e.g. $u_{\text{inj}} \leq 0.11$ mm/s, we can clearly see from Fig. 5.4(a) and (b) that water progresses with three distinctive capillary fingers into the matrix. In the squeezing regime, thanks to the blocking effect from the oil plug, more water imbibes into the matrix and thus a relatively large amount of oil is expelled from the matrix into the fracture. This suggests a higher oil recovery factor at steady state as shown in Fig. 5.5(a).

As the water injection velocity increases, e.g., $u_{\text{inj}} = 4.44$ mm/s and 5.56 mm/s, the jetting regime occurs where the expelled oil exhibits a shape different from the one in the squeezing regime. Due to the higher water injection velocity in the fracture, the oil droplet is stretched into a long thread by the incoming water, with its root attached to the widest matrix channel that supplies the expelled oil [Fig. 5.3 (e) and (f)]. After the oil thread gets pinched off at its root, it quickly retracts to a dumbbell shape. During the early stage of the oil thread spreading towards the right end of the fracture, the imbibition of water into the right-half region of the matrix is quickly blocked, which explains why the final oil recovery factor is much less than that in the squeezing regime [see Fig. 5.5(a)]. The dumbbell-shaped oil thread eventually flows out of the fracture,

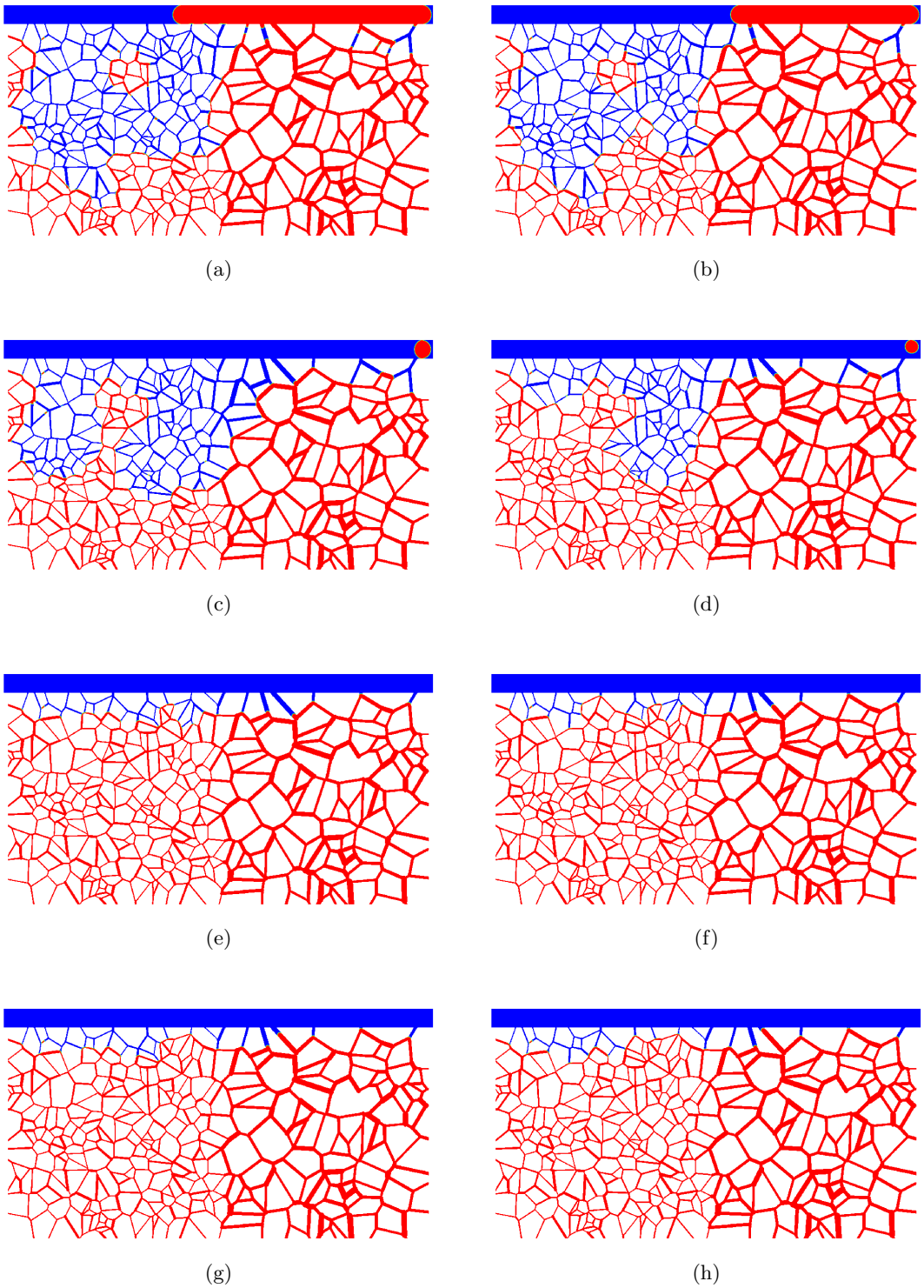

Figure 5.9: Steady-state fluid distributions in the right-wide matrix for different injection velocities: (a) $u_{\text{inj}} = 0.075$ mm/s; (b) $u_{\text{inj}} = 0.11$ mm/s; (c) $u_{\text{inj}} = 0.56$ mm/s; (d) $u_{\text{inj}} = 1.11$ mm/s; (e) $u_{\text{inj}} = 4.44$ mm/s; (f) $u_{\text{inj}} = 5.56$ mm/s; (g) $u_{\text{inj}} = 22.22$ mm/s and (h) $u_{\text{inj}} = 44.44$ mm/s. Note that the water and the oil are shown in blue and red respectively.

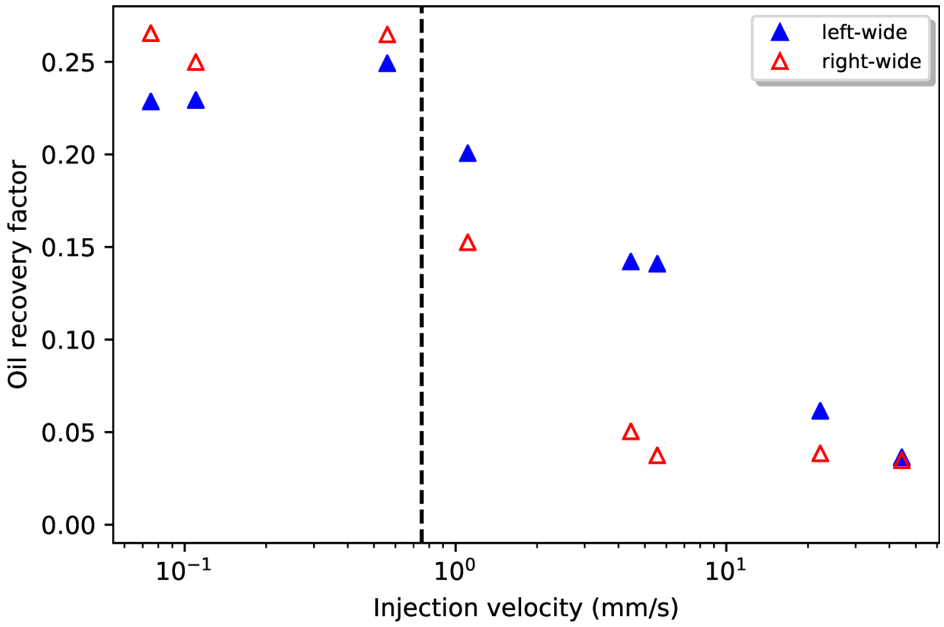

Figure 5.10: Ultimate oil recovery factor as a function of injection velocity u_{inj} for both the left-wide and the right-wide matrixes.

which can be seen from Fig. 5.4 (e) and (f).

As the rate of water injection continues to increase, the expelled oil enters the fracture as isolated drops [Fig. 5.3 (g) and (h)], which is known as the dripping regime. The higher injection velocity results in a larger shear force acting on the expelled oil drop, leading to an earlier pinch-off before it can grow longer. The size of the drop decreases with increasing water injection rate. These drops are transported quickly along the fracture by the injected water. Since the water is able to freely flow out through the fracture and no blocking effect exists, overall imbibition depth is much shallower than that in the other two regimes. Accordingly, the oil recovery factor in this regime is the lowest among all the three regimes, typically lower than 8% as observed in Fig. 5.5(a). On the other hand, the water infiltration path into the matrix is less selective than the other two regimes, as can been seen from Fig. 5.4 (g) and (h) where the imbibition front progresses almost uniformly down into the matrix. This regime resembles the "instantly filled fracture" regime identified experimentally by Rangel-German et al. [66], in which water is mainly pumped through the fracture and little water is imbibed into the matrix. In addition, the water saturation in the matrix in this regime scales linearly (correlation coefficient of 0.99) with the square root of time before reaching the steady state [see Fig. 5.5(b)], which is consistent with the experimental finding of Rangel-German et al. [148].

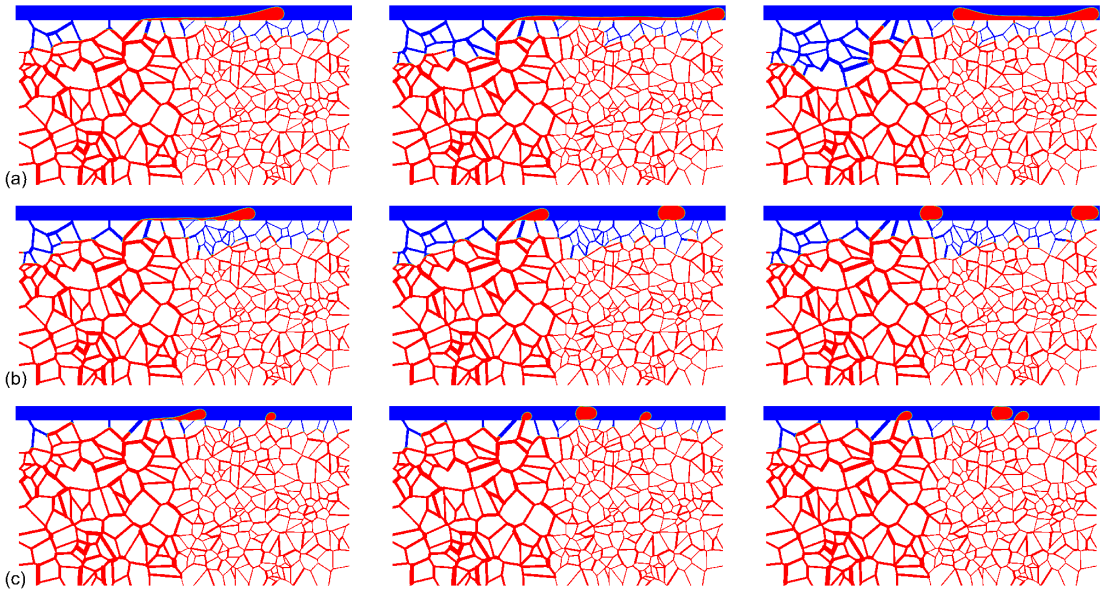

Figure 5.11: Snapshots of fluid distributions during imbibition for different interfacial tensions: (a) $\sigma = 30$ mN/m; (b) $\sigma = 15$ mN/m and (c) $\sigma = 5$ mN/m. Note that the water and the oil are shown in blue and red respectively.

Among the above three regimes, the squeezing regime has the highest oil recovery factor and takes a relatively long time to reach the steady state. Specifically, the maximum oil recovery factor rf $= 0.25$ is reached at $u_{\text{inj}} = 0.56$ mm/s in the squeezing regime. On the contrary, in the dripping regime, the imbibition reaches the steady state almost instantly, and the final oil recovery factor is extremely low. We also record the pressure differences between the upstream and outlet in the fracture during the displacement for the three typical regimes, and the results are shown in Fig. 5.6. Among these three regimes, the pressure build-up is the most significant in the squeezing regime. For the squeezing regime, the pressure upstream keeps at a high level before reaching IV, although sudden drop occurs when more wetting fluid is imbibed into the matrix. The pressure build-up process in the squeezing regime can be also seen from the pressure distributions plotted in Fig. 5.7. As the oil plug grows, the pressure upstream in the fracture increases while the pressure of the non-wetting fluid in the matrix decreases [Fig. 5.7(a)-(c)]. For the jetting regime, a certain level of pressure build-up is also observed, which is consistent with the fluid distributions in Fig. 5.3(e) and (f). In contrast, the pressure upstream maintains at a rather low level throughout the displacement process for the dripping regime.

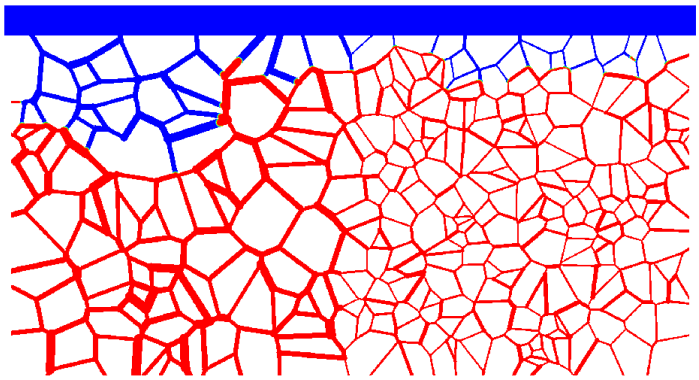

(a)

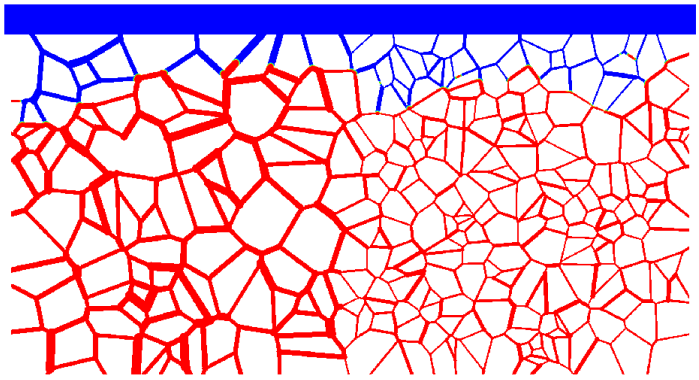

(b)

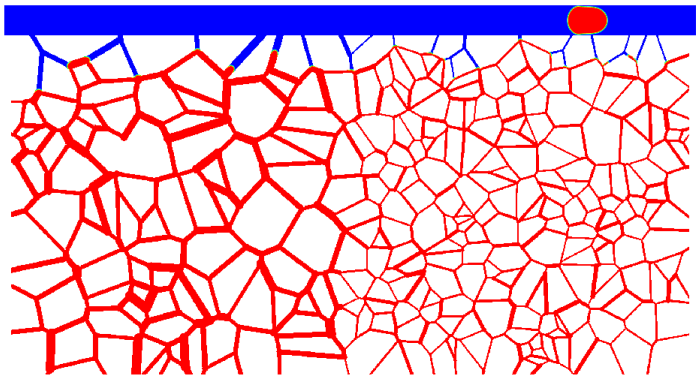

(c)

Figure 5.12: Fluid distributions at steady-state for different interfacial tensions: (a) $\sigma =$ 30 mN/m; (b) $\sigma = 15$ mN/m and (c) $\sigma = 5$ mN/m. Note that the water and the oil are shown in blue and red respectively.

5.2.2 Effect of geometry configuration of the dual permeability zones

The porous matrix in the primary geometry is intentionally constructed as two different regions, where the mean channel width in the left-half region of the matrix is twice of that in the right-half region. Such an geometry configuration of the matrix is expected to significantly influence the water imbibition process due to the interplay of the water imbibition into the matrix and oil accumulation and transport in the fracture. As previously shown in Fig. 5.3, the oil blobs prefer flowing through the widest throat into the fracture and accumulate locally in the fracture towards the downstream direction. In the squeezing and jetting regimes, the oil plug or thread would entirely or partially block the matrix entrances downstream. Thus, it is important whether the high permeability zone is located upstream or downstream of the fracture.

In this subsection, we investigate how the geometry configuration of the high and low permeability zones affects the imbibition process and the oil recovery factor. By reversing the matrix in the primary geometry (Fig. 5.1) from left to right, we create another geometry with wide throats distributed in the right-half region of the matrix and the water is still injected from the left end of the fracture. The new set-up is tantamount to reversing the water injection direction in Fig. 5.1. We now distinguish the two matrixes by calling the original one "left-wide matrix" and the new one "right-wide matrix", respectively. The left-wide matrix corresponds to the geometry configuration that the high permeability zone is located upstream and the low permeability zone downstream. By contrast, the right-wide matrix has the high permeability zone downstream and the low permeability zone upstream.

Fig. 5.8 shows the water imbibition process in the right-wide matrix and the dynamics of expelled oil blobs in the fracture for eight different injection velocities. Note that the corresponding results regarding the left-wide matrix have been shown in Fig. 5.3. Different from the results in Fig. 5.3, it is seen in Fig. 5.8 that the squeezing regime [Fig. 5.8(a-d)] changes to the dripping regime [Fig. 5.8(e-h)] directly without undergoing the jetting regime, as the oil shape in the fracture changes from plug to small drop by increasing injection velocity. The regime alteration process is seen clearly from row (d) to (e) in Fig. 5.8, as the location of the high permeability zone is downstream near the outlet of the fracture, the expelled oil blobs from the widest throat are snapped off easily and carried away quickly as the injection velocity increases. Thus the elongation of the oil thread is less likely to happen. In addition, we also notice that water advances almost exclusively into the matrix from the left-half region, i.e. low permeability zone [also see the steady-state fluid distributions in Fig. 5.9 (a)-(d)], whereas in the left-wide matrix, water invades mostly into the high permeability zone. This difference lies

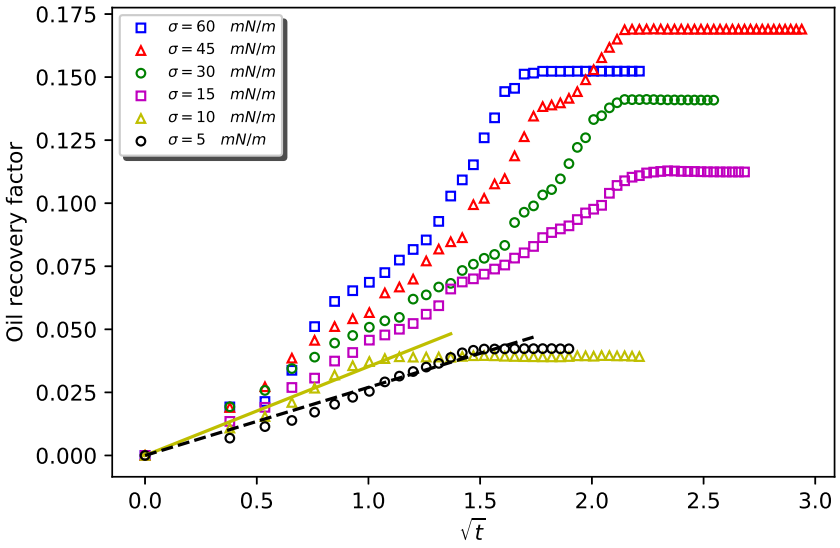

Figure 5.13: Time evolution of oil recovery factor for various water-oil interfacial tensions. The solid and dashed lines are the linear fits to the data of $\sigma = 10$ mN/m and $\sigma = 5$ mN/m, respectively, which are given by $rf = 0.03524 \times t^{0.5}$ and $rf = 0.02699 \times t^{0.5}$.

in that in the right-wide matrix, the preference of water imbibition into the narrower throats is attributed not only to the larger capillary pressure, but also to the build-up squeezing pressure.

Figure 5.10 plots the final oil recovery factor as a function of water injection velocity for both the left-wide matrix and the right-wide matrix. It reveals that the oil recovery factor is high (around $0.22 \sim 0.26$) at low injection velocity ($u_{\text{inj}} \leq 0.78$ mm/s) in both geometry configurations. Upon increasing u_{inj} from 1.11 mm/s, the oil recovery factor decreases and reaches its minimum value of 0.04 at the highest injection velocity in both matrix geometries. It is seen in Fig. 5.10 that there exists a critical velocity (around 0.78 mm/s) above which the left-wide matrix has a higher oil recovery factor, but below which, the right-wide matrix has a higher oil recovery factor. In the left-wide geometry, water is found to advance further into the left-half region (high permeability zone) which is connected to the upstream of the fracture. This counters our intuition that wider throats corresponding to smaller capillary pressure unfavor the imbibition of water into the matrix. We speculate that this is due to the build-up squeezing pressure upstream when the oil blobs accumulate at the downstream of the fracture and block the fracture channel. By flipping the geometry from "left-wide matrix" to "right-wide matrix", we again observe that water invades deeper into the left-half

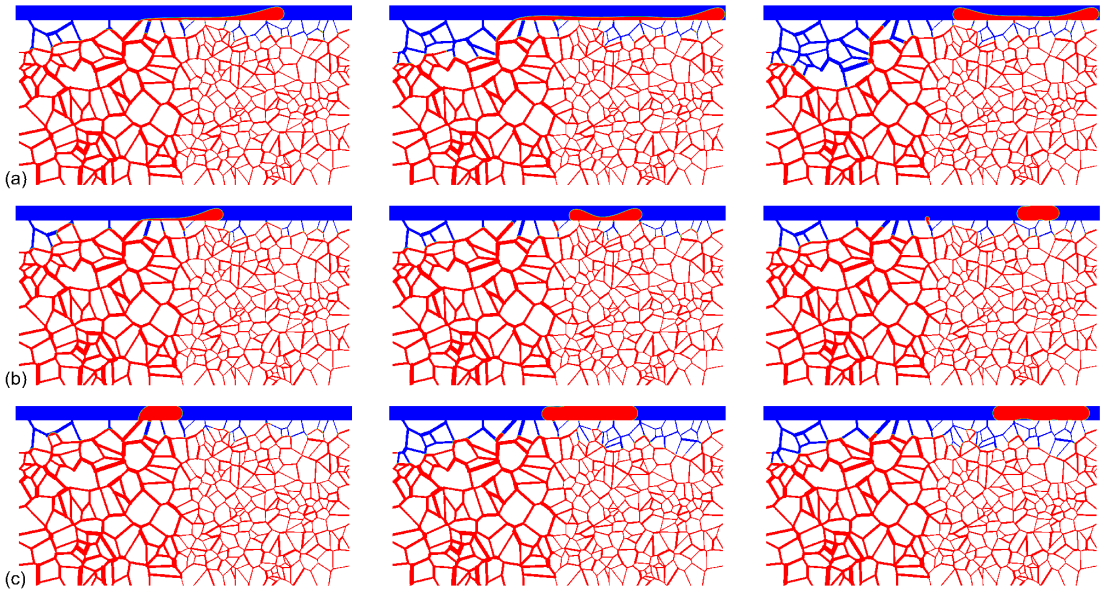

Figure 5.14: Snapshots of the fluid distributions during imbibition for different viscosity ratios: (a) $\lambda = 1$; (b) $\lambda = 0.1$ and (c) $\lambda = 10$. Note that the water and the oil are shown in blue and red respectively.

region of the matrix (low permeability zone) that is adjacent to the upstream of the fracture, which confirms our speculation. To conclude, the geometry configuration of the dual permeability zones plays a significant role in the oil recovery by counter-current imbibition in a fracture-matrix system.

5.2.3 Effect of interfacial tension

As spontaneous imbibition is a result of capillary pressure, the dynamic imbibition process and the final recovery factor are significantly affected by the interfacial tension between two fluids [153]. To investigate the impact of the interfacial tension on the oil recovery process in a fracture-matrix system, six different simulations with the interfacial tension values of $\sigma = 5$, 10, 15, 30, 45 and 60 mN/m are carried out. All the other parameters are chosen as the default values mentioned before, and the primary geometry, i.e. the left-wide matrix is used as an illustration.

According to the Young-Laplace equation, the capillary intrusion of water into the matrix is weakened with the decrease of interfacial tension σ. This is confirmed by the imbibition depths in Fig. 5.11, which shows the dynamic imbibition processes at different values of σ. It is also observed that with the interfacial tension decreasing from 30 mN/m to 5 mN/m, the flow regime for the expelled oil changes from the jetting

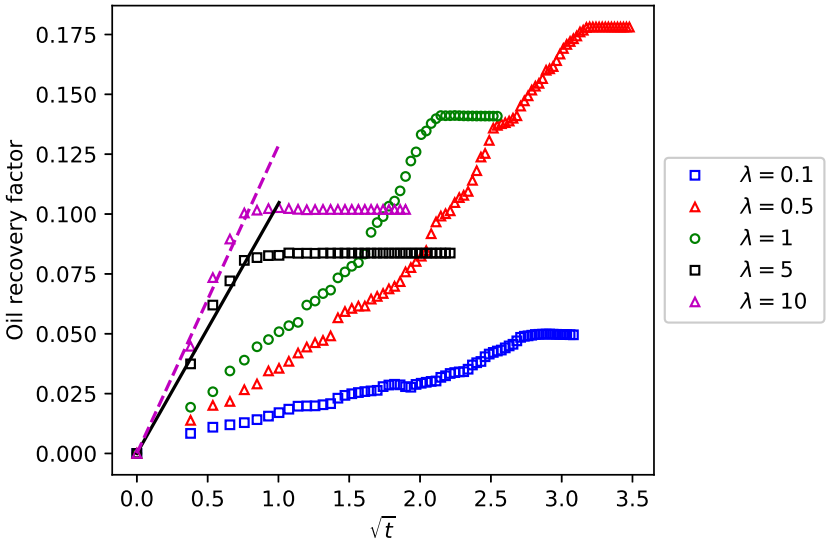

Figure 5.15: Time evolution of the oil recovery factor for the viscosity ratios of 0.1, 0.5, 1, 5 and 10. Note that the solid and dashed lines represent the linear fits to the data of $\lambda = 5$ and $\lambda = 10$, respectively, which are given by $rf = 0.10439 \times t^{0.5}$ and $rf = 0.12858 \times t^{0.5}$.

regime [Fig. 5.11 (a) and (b)] to the dripping regime [Fig. 5.11 (c)]. In this regard, decreasing interfacial tension has a similar effect to increasing water injection velocity, which can be explained by the competition between the viscous shear force exerted on the expelled oil blobs and the capillary force resisting the interface deformation. However, the imbibition behavior in the matrix cannot be described by the capillary number (Ca). The capillary number is often used to characterize the forced displacement, in which the characteristic velocity, as a measure of viscous force, is defined as the injection velocity or the imposed pressure difference. In the spontaneous imbibition, the imbibition rate is not determined by the injection velocity of water into the fracture but by the interfacial tension, suggesting that it is more appropriate to use the interfacial tension rather than the capillary number defined through the injection velocity of water for our discussion.

Figure 5.12 presents the steady-state oil-water distribution for different interfacial tensions. It shows that with larger interfacial tension, the water imbibes deeper into the left-half matrix with high permeability. This is because the elongated expelled oil in the jetting regime can block the fracture channel to some extent, leading to an increased upstream pressure that drives more water into the high permeability zone. In addition, increasing σ will increase the capillary pressure, which acts as the only driving force for

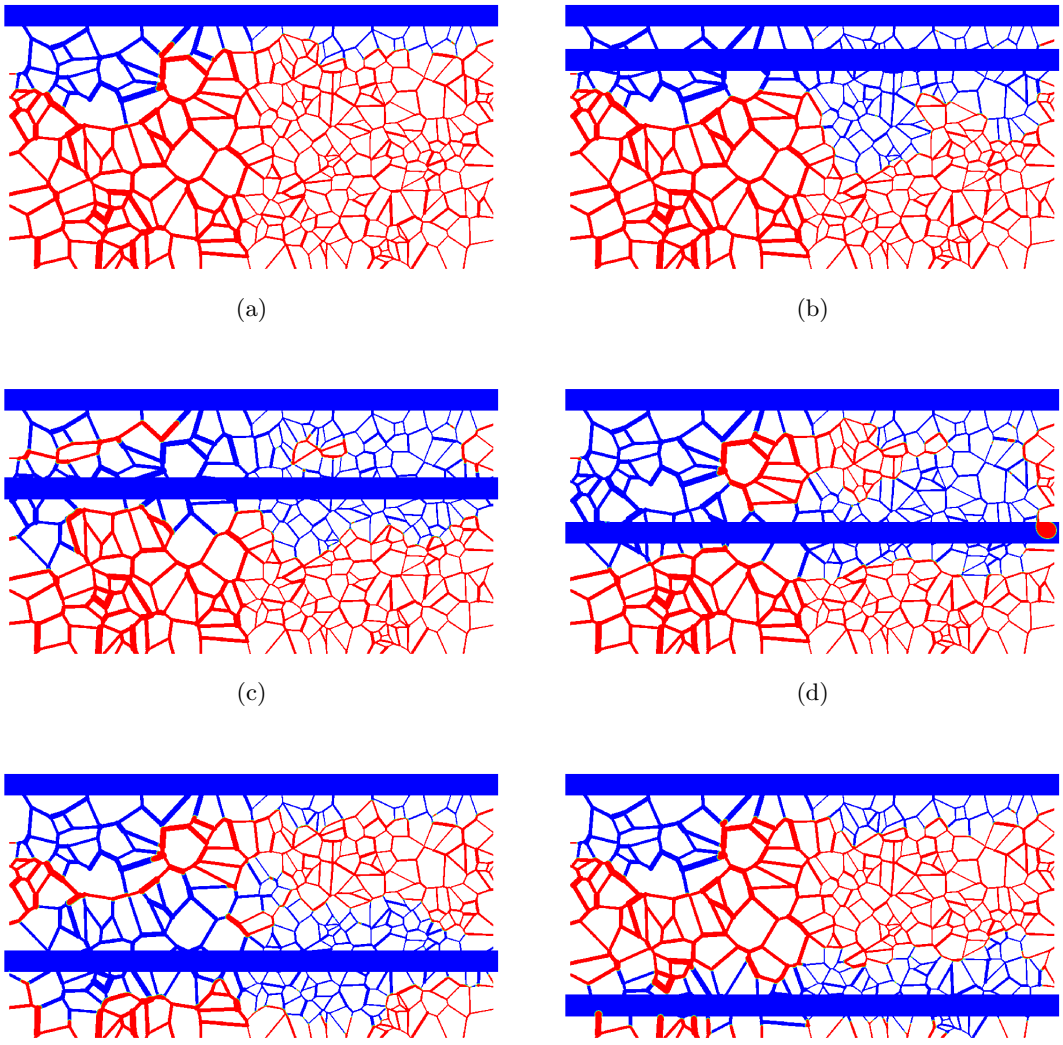

Figure 5.16: Fluid distributions at steady-state for different fracture spacing: (a) $\delta = 0$; (b) $\delta = 0.167$; (c) $\delta = 0.333$; (d) $\delta = 0.5$; (e) $\delta = 0.667$ and (f) $\delta = 0.833$. Note that $\delta = 0$ corresponds to the primary geometry with only one fracture. Note that the water and the oil are shown in blue and red respectively.

spontaneous imbibition of water into the matrix, leading to more water imbibed into the matrix and enhancing the oil recovery.

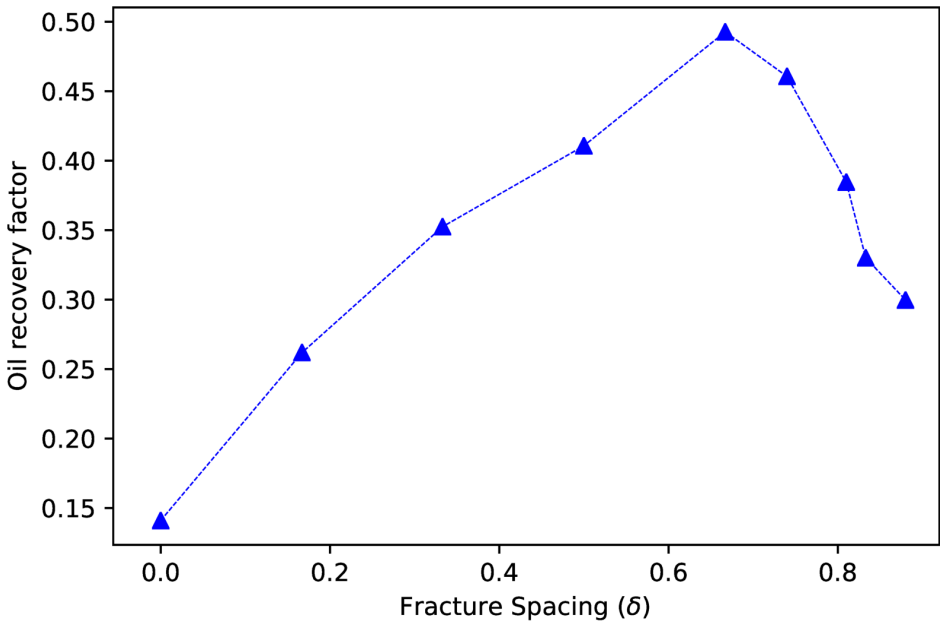

Figure 5.17: Ultimate oil recovery factor as a function of the fracture spacing, which is normalized by the matrix height.

Figure 5.13 displays the oil recovery factor as a function of the square root of time for different interfacial tensions. It is found that a larger interfacial tension leads to a higher imbibition rate and usually a higher ultimate oil recovery factor. These trends are consistent with the previous findings by Rokhforouz and Amiri [50] who studied the imbibition of water from a fracture into a porous media composed of randomly distributed cylinders using the phase-field method. In addition, Fig. 5.13 shows that in the dripping regime, the linear relationship between the oil recovery factor and the square root of time is still valid.

5.2.4 Effect of viscosity ratio

The effect of viscosity ratio, defined as $\lambda = \mu_{water}/\mu_{oil}$, is investigated for $\lambda = 0.1$, 0.5, 1, 5 and 10. Different values of viscosity ratio are achieved by adjusting the viscosity of oil while keeping the viscosity of water unchanged.

Fig. 5.14(a) shows snapshots of the fluid distributions for the viscosity ratios of 0.1, 1 and 10. It is found in the fracture that the expelled oil morphology changes from jetting regime to the dripping regime with increasing viscosity ratio. In the jetting regime, see

Fig. 5.14 [row (a)], water progresses more in the high permeability zone because the long oil thread blocks the water passage into the low permeability zone. Fig. 5.14(b) shows a combination of the jetting and dripping regimes. Clearly, water advances into the matrix within a very limited depth because of high viscous force between oil and the matrix wall. When the viscosity ratio is increased to 10, see Fig. 5.14(c), the oil blob occupies the whole cross-section of the fracture, and the squeezing regime seemingly occurs. However, the squeezing pressure upstream is not built up because the oil plugs in the fracture are driven by water towards the outlet quickly. Note that the formed oil plugs move more easily towards the outlet in the fracture when the oil phase is of lower viscosity. In this case, the water front advances evenly into the left and right regions of the matrix – like in the dripping regime. Figure 5.15 displays the oil recovery factor as a function of the square root of time for various viscosity ratios. It is clear that the highest oil recovery factor is reached when $\lambda = 0.5$, different from the previous finding of Rokhforouz and Amiri [50], who found the highest oil recovery factor occurring at the viscosity ratio of unity. In addition, the imbibition rate increases with the viscosity ratio, and the linear relationship between oil recovery factor and the square root of time is interestingly observed for $\lambda = 5$ and $\lambda = 10$, also like in the dripping regime.

5.2.5 Effect of fracture spacing

In standard "water-flooding" oil recovery, the fracture spacing is an important characteristic of natural fractured rock [154, 155, 156, 157] that affects the water supply, the transport of expelled oil and thus the amount of recoverable oil. It is also important in artificially created fracture network during unconventional gas & oil extraction to optimize the production rate and reduce the economic costs [158, 159, 160, 161]. To investigate the effect of fracture spacing on the counter-current imbibition, we add another horizontal fracture in the primary geometry. By varying the spacing between the added fracture with the original one, we can observe the effect of fracture spacing on the dynamic imbibition process and the ultimate oil recovery factor. Eight different fracture spacings are considered, where the fracture spacings normalized by the matrix height are $\delta = 0.167$, 0.333, 0.5, 0.667, 0.74, 0.81, 0.833 and 0.88, respectively.

Figure 5.16 shows the steady-state fluid distributions for different fracture spacings where the result of the primary geometry with a single fracture is also shown for comparison. From this figure, it can be seen that the interaction between the water fronts from different fractures is greatly affected by the fracture spacing. Specifically, when two fractures are very close to each other [Fig. 5.16(b)], the oil in the porous matrix located between two fractures is quickly expelled out, and thus only the lower fracture

supplies water for further imbibition into the lower porous region. By increasing the fracture spacing, the water fronts from two fractures have more space to develop, and thus more oil is expelled into the fracture [Fig. 5.16(c) - (d)]. This explains why the oil recovery factor overall increases with the fracture spacing, which is shown in Fig. 5.17. However, when the fracture spacing δ is increased from 0.667 to 0.88, the oil recovery factor does not increase but decrease instead (Fig. 5.17). This is because the lower fracture is too close to the matrix downside boundary, leading to dead throats in the lower porous region and thus restricting the development of water fronts, for example, at $\delta = 0.833$ [see Fig. 5.16(f)].

5.3 Conclusions

A lattice Boltzmann colour-gradient model is used for pore-scale simulation of the counter-current water-oil imbibition in a strongly water-wet fracture-matrix system. The effects of water injection velocity into the fracture (u_{inj}), geometry configuration of the high and low permeability zones, interfacial tension (σ), viscosity ratio (λ) of water to oil and the fracture spacing (δ) (if there are multiple fractures) on the dynamic imbibition process and the ultimate oil recovery factor are systematically analyzed. The main findings are summarized as follows.

The morphology of the expelled oil in the fracture changes with the water injection velocity and the interfacial tension. Depending on the relative strength of the viscous shear force and capillary force, the expelled oil in the fracture appears as either plugs or long threads or isolated drops. Accordingly, they are classified into three regimes, i.e. squeezing, jetting and dripping.

In the primary geometry, i.e. the one with left-wide porous matrix, we observe the counter-intuitive phenomenon that more water invades into the left-half region of the matrix (high permeability zone), which is due to that the oil plug entirely blocks the downstream fracture channel. The build-up pressure upstream facilitates water to invade the wider throats which improves the oil recovery factor. The ultimate oil recovery factor is not significantly affected by the injection velocity and is generally high in the squeezing regime; whereas in the jetting regime, it decreases gradually with the increase of injection velocity. In the dripping regime, the ultimate oil recovery factor is extremely low and we find that the amount of oil expelled out from the matrix scales with the square root of time, consistent with the previous experimental result [148].

The geometry configuration of the high and low permeability zones affects the amount of

oil that can be recovered by the counter-current imbibition in a fracture-matrix system. There exists a critical injection velocity above which water is preferably injected from the fracture end adjacent to the high permeability zone.

Decreasing interfacial tension favors reduction of the oil recovery as the oil morphology in the fracture shifts to the dripping regime. Increasing water-to-oil viscosity ratio leads to a higher water imbibition rate and the highest oil recovery factor is achieved at $\lambda = 0.5$. Finally, introducing a second horizontal fracture is found to significantly enhance oil recovery. Increasing fracture spacing first leads to an increasing trend of the oil recovery factor, and then the highest oil recovery factor is reached when the fracture spacing is large enough to allow the water imbibition fronts from different fractures to develop independently. A further increase of the fracture spacing decreases the oil recovery factor as the lower fracture becomes too close to the matrix downside boundary.

Chapter 6

Conclusions and future research

In this final Chapter, we conclude our research and discuss possible directions for future research.

6.1 Summary

Our investigation into the transport mechanism of immiscible two phases within the porous and fractured media has resulted in a deeper understanding of the pore-scale dynamics. The colour gradient two-phase LBM has allowed us to systematically look into the effects of various fluid properties and geometry configurations, and reveal the role they play in the displacement process. This lays the foundation for explaining the phenomena on a larger-scale and aids to optimise the oil recovery process.

The first objective of this work is presented in Chapter 4 for the verification and validation of the model implementation. It is on the basis of the state-of-the-art colour gradient two-phase LBM, which is able to precisely control the contact angle for both static and dynamic problems, essential for accurate modelling of two-phase displacement in porous media. The model has shown many advantages including strict mass conservation for each fluid, low spurious currents, wide accessibility to various viscosity ratios, and high accuracy in modelling contact angle. However, it was previously limited to the simplified porous media. To fill this gap, the present work extends the colour-gradient model for two-phase displacement in a porous flow structure extracted from a realistic Berea sandstone sample. It is demonstrated that the colour-gradient model is effective and accurate for pore-scale simulation of two-phase flows in arbitrarily complex porous media. To be specific, direct simulation on the 2D realistic porous image based on a thin section of a 3D Berea sandstone rock sample is used, since the

complexity of the pore-space geometry is preserved. The size of the computational domain is large enough to be a representative elementary volume (REV) of the sample with the resolution of 0.67 μm. A series of two-phase displacement simulations driven by an imposed pressure difference are performed and the effect of the viscosity ratio, interfacial tension, and contact angle on the fluid distributions at breakthrough time and the evolution of displacing fluid saturation are analysed.

We demonstrated that the viscosity ratio plays an important role in the displaced phase recovery efficiency. When the viscosity ratio is equal to unity, the saturation of the displacing fluid has the highest value, and increases linearly with time. The displacing fluid saturation drops rapidly when the viscosity ratio varies from 1 to 20 and then stays almost unchanged regardless of the interfacial tension and the contact angle if the viscosity ratio continue to increase from 20 to 50. While the viscosity ratio (λ) changing from 1 to 30, although the displacing fluid saturation reduces with λ, the reduction becomes less significant at larger λ values. At each viscosity ratio, increasing the contact angle or the interfacial tension have the same effect, both leading to a higher displacing fluid saturation or displacement efficiency. Generally higher interfacial tension leads to a higher displacement efficiency. And the linear relationship between the saturation of the displacing fluid and the evolving time at various interfacial tension still holds. It is also observed that at low interfacial tension value of 0.0005 mu$\cdot$ts^{-2}, thin viscous fingers appear. When the interfacial tension increases from 0.0005 mu$\cdot$ts^{-2} to 0.015 mu$\cdot$ts^{-2}, the size of the trapped nonwetting fluid blobs increase and the number decrease. Further increase the interfacial tension to 0.03 mu$\cdot$ts^{-2}, the displacing front becomes flat in some pores, and the displacing fluid flows into the large pore more easily due to the higher capillary pressure. We also found that the effect of contact angle on the displacement efficiency is limited within the 2D Berea sandstone. Meanwhile, no obvious changes of the invading paths of the wetting fluid is observed except for a few branches.

Chapter 5 employed the colour gradient two-phase LBM model for the purpose of solving the counter-current spontaneous imbibition process in a dual-permeability fracture-matrix system. The studied matrix is constructed using a Voronoi tessellation technique where the pore structure is modeled as randomly connected throats. The throat widths obey a log-normal distribution, which often serves as a good geometric approximation to natural porous media in statistics. This is different from many previous works which were done based on simple circular or square cylinders of the solid grains in the matrix. The porous matrix is intentionally constructed as two different regions, where the statistic average of the pore throat width in the left half of the domain is twice of

that in the right half, yielding a dual-permeability porous matrix with high and low permeability zones.

By examining different water injection velocities and interfacial tensions, it is identified for the first time that the three distinct imbibition regimes exist, i.e. the squeezing, jetting and dripping regimes, and they can be distinguished with different morphologies of expelled oil in the fracture (piston-like plug, elongated liquid thread and isolated drops). Especially, in the squeezing regime, it is interestingly found that the build-up of the squeezing pressure upstream is able to facilitate water into the permeability zone closer to the fracture inlet thus increasing the oil recovery factor, due to the blocking effect from the oil plug. In the jetting regime, the final oil recovery factor is much less than that in the squeezing regime. And the oil recovery factor is the lowest in the dripping regime, typically lower than 8%. Besides, a linear relationship between the oil recovery factor and the square root of time is observed in the dripping regime, which is consistent with the available experimental finding. The geometry configuration of the dual permeability zones is shown to play a significant role in the oil recovery by switching the side of the high and low permeability zones. It has the potential to affect the amount of oil that can be recovered by the counter-current imbibition in a fracture-matrix system through transition of the different regimes. A series of simulations with different interfacial tensions show that a larger interfacial tension leads to a higher imbibition rate and usually a higher ultimate oil recovery factor, consistent with previous numerical findings studying the imbibition of water from a fracture into a porous medium composed of randomly distributed cylinders using the phase-field method. A higher viscosity ratio leads to a higher imbibition rate, however the highest oil recovery factor is reached when $\lambda = 0.5$, different from the previous work which reported that the highest oil recovery factor occurring at the viscosity ratio of unity. In addition, another horizontal fracture is added in order to investigate the effect of fracture spacing on the counter-current imbibition. The fracture spacing that produces the highest oil recovery factor is found. These results could serve as a guideline for the optimal design of the water-injecting oil extraction techniques.

6.2 Future research

In this thesis, the colour gradient two-phase LBM model has shown its potential in simulating a wide range of viscosity ratios for the two immiscible fluids in complex porous geometries. The underlying mechanisms for displacement dynamics are found to be well captured. With the continuous developments in computer hardware and

software methods, LB simulations are likely to be much faster and more affordable in the near future. Further studies can be carried out in three dimensional in terms of the computed porous geometry. Moreover, the present work stores the full lattice, making parallelization straightforward but wasteful. It is possible to use a sparse domain decomposition technique which helps to avoid the need to store and operate on lattice points located within a solid phase [162].

The current study on the counter-current spontaneous imbibition process in a dual-permeability fracture-matrix system is only preliminary, apart from the many factors investigated in this work, media inhomogeneity is also a key factor for spreading and displacement of fluids within porous media which deserves further study in the future. In addition, it is desirable to validate the numerical simulations by experimental measurement.

Lastly, real oil reservoirs tend to be mixed wet, which means some parts maybe water-wet and other parts being oil-wet. The effect of mixed wettability could be carried out on the counter-current imbibition process. Also, it is possible to quantify the interfacial area in order to provide insights about physical displacement process as proposed by Hassanizadeh and Gray [132].

Appendix A

From lattice Boltzmann equation to the Navier-Stokes equations: Chapman-Enskog expansion

Here we derive the macroscopic NSEs from the lattice Boltzmann equation in detail through Chapmann-Enskog expansion, which is a multi-scale analysis by Chapman and Enskog. Normally three time scales are adopted in the multiscale expansion:

- **the collision time scale ϵ^0 (ϵ is an arbitrarily small positive number)** the particle collision process is very fast.
- **the convection time scale ϵ^{-1}** the convection process is slower than the particle collision process.
- **the diffusion time scale ϵ^{-2}** the diffusion process is slower than the convection process.

The spatial scale for the collision process is the molecular mean free path (λ), while the characteristic flow length (L) for convection and diffusion process. Within this multiscale method, three time scales are usually adopted: the discrete scale t, and two continuous scale $t_0 = \epsilon t$ and $t_1 = \epsilon^2 t$. Two spatial scales are used: the discrete scale $\mathbf{x}$ and the continuous scale $\mathbf{x}_0 = \epsilon \mathbf{x}$. Thus the time derivative, spatial derivative and the distribution function are expanded as follows

$$\partial_t = \epsilon \partial_{t_0} + \epsilon^2 \partial_{t_1}, \quad \partial_\alpha = \epsilon \partial_{0\alpha}, \quad f_i = f_i^{(0)} + \epsilon f_i^{(1)} + \epsilon^2 f_i^{(2)} + \cdots \tag{A.1}$$

where ϵ is a small number proportional to Kn, and $\partial_\alpha = \nabla_\alpha$ is the spatial derivative.

The second order Taylor series expansion of the LBGK equation (2.9) yields

$$\delta_t(\partial_t + \mathbf{c}_i \cdot \nabla) f_i + \frac{\delta_t^2}{2}(\partial_t + \mathbf{c}_i \cdot \nabla)^2 f_i + \frac{1}{\tau}(f_i - f_i^{(eq)}) + O(\delta_t^3) = 0 \tag{A.2}$$

Now substitute the expansions (A.1) into Eq. (A.2) and compare the coefficients of each order of ϵ, one can obtain that

$$\epsilon^0 : f_i^0 = f_i^{(eq)}, \tag{A.3}$$

$$\epsilon^1 : (\partial_{t_0} + \mathbf{c}_i \cdot \nabla_0) f_i^{(eq)} + \frac{1}{\tau\delta_t} f_i^{(1)} = 0, \tag{A.4}$$

$$\epsilon^2 : \partial_{t_1} f_i^{(eq)} + (\partial_{t_0} + \mathbf{c}_i \cdot \nabla_0) f_i^{(1)} + \frac{\delta_t}{2}(\partial_{t_0} + \mathbf{c}_i \cdot \nabla_0)^2 f_i^{(eq)} + \frac{1}{\tau\delta_t} f_i^{(2)} = 0, \tag{A.5}$$

Using Eq. (A.4), Eq. (A.5) can be simplified as

$$\epsilon^2 : \partial_{t_1} f_i^{(eq)} + (1 - \frac{1}{2\tau})(\partial_{t_0} + \mathbf{c}_i \cdot \nabla_0) f_i^{(1)} + \frac{1}{\tau\delta_t} f_i^{(2)} = 0. \tag{A.6}$$

From Eq. (A.3), together with Eqs. (2.8) and (2.11), we can obtain that

$$\sum_i f_i^{(k)} = 0, \ \sum_i \mathbf{c}_i f_i^{(k)} = 0 \ for \ k > 0. \tag{A.7}$$

From Eq. (A.4), we can get the macroscopic equation at time scale t_0 from its zeroth and first order velocity moments

$$\partial_{t_0}\rho + \nabla_0 \cdot (\rho\mathbf{u}) = 0, \tag{A.8}$$

$$\partial_{t_0}(\rho\mathbf{u}) + \nabla_0 \cdot \pi^{(0)} = 0, \tag{A.9}$$

where $\pi_{\alpha\beta}^{(0)} = \sum_i c_{i\alpha} c_{i\beta} f_i^{(0)} = \rho u_\alpha u_\beta + p\delta_{\alpha\beta}$ is the zeroth-order momentum flux tensor, with $p = c_s^2\rho$. The following properties of the generalized lattice tensors of the $D2Q9$ model have been used here:

$$\begin{aligned} &\sum_i \omega_i c_{i\alpha} = \sum_i \omega_i c_{i\alpha} c_{i\beta} c_{i\gamma} = 0, \quad \sum_i \omega_i c_{i\alpha} c_{i\beta} = c_s^2 \delta_{\alpha\beta} \\ &\sum_i \omega_i c_{i\alpha} c_{i\beta} c_{i\gamma} c_{i\theta} = c_s^4 \Delta_{\alpha\beta\gamma\theta} \end{aligned} \tag{A.10}$$

where $\Delta_{\alpha\beta\gamma\theta} = \delta_{\alpha\beta}\delta_{\gamma\theta} + \delta_{\alpha\gamma}\delta_{\beta\theta} + \delta_{\alpha\theta}\delta_{\beta\gamma}$. Eqs. (A.8) and (A.9) are the Euler equations. Similarly, the zeroth and first order moments of Eq. (A.6) leads to the conservation

equations at time scale t_1,

$$\partial_{t_1}\rho = 0, \tag{A.11}$$

$$\partial_{t_1}(\rho\mathbf{u}) + \left(1 - \frac{1}{2\tau}\right)\nabla_0 \cdot \pi^{(1)} = 0, \tag{A.12}$$

where $\pi^{(1)}_{\alpha\beta} = \sum_i c_{i\alpha}c_{i\beta}f_i^{(1)}$. Next we evaluate $\pi^{(1)}_{\alpha\beta}$ by multiplying Eq. (A.4) by $c_{i\alpha}c_{i\beta}$ and take summation over i

$$\begin{aligned}
-\frac{1}{\tau\delta_t}\sum_i c_{i\alpha}c_{i\beta}f_i^{(1)} &= \sum_i c_{i\alpha}c_{i\beta}(\partial_{t_0} + \mathbf{c}_i \cdot \nabla_0)f_i^{(0)} \\
&= \partial_{t_0}\sum_i c_{i\alpha}c_{i\beta}f_i^{(0)} + \partial_{0\gamma}\sum_i c_{i\alpha}c_{i\beta}c_{i\gamma}f_i^{(0)} \\
&= \partial_{t_0}(\rho u_\alpha u_\beta + p\delta_{\alpha\beta}) + \partial_{0\gamma}[\rho c_s^2(\delta_{\alpha\beta}u_\gamma + \delta_{\alpha\gamma}u_\beta + \delta_{\beta\gamma}u_\alpha)]
\end{aligned} \tag{A.13}$$

where

$$\begin{aligned}
\partial_{t_0}(\rho u_\alpha u_\beta + p\delta_{\alpha\beta}) &= \partial_{t_0}(\rho u_\alpha u_\beta) - c_s^2\nabla_0(\rho u)\delta_{\alpha\beta} \\
&= u_\beta\partial_{t_0}(\rho u_\alpha) + u_\alpha\partial_{t_0}(\rho u_\beta) - u_\alpha u_\beta\partial_{t_0}\rho - c_s^2\nabla_0(\rho u)\delta_{\alpha\beta} \\
&= u_\beta[-\partial_{0\gamma}(\rho u_\alpha u_\gamma + \rho c_s^2\delta_{\alpha\gamma})] + u_\alpha[-\partial_{0\gamma}(\rho u_\beta u_\gamma + \rho c_s^2\delta_{\beta\gamma})] - u_\alpha u_\beta\partial_{t_0}\rho \\
&\quad - c_s^2\nabla_0(\rho u)\delta_{\alpha\beta} \\
&= -c_s^2 u_\beta\partial_{0\alpha}\rho - c_s^2 u_\alpha\partial_{0\beta}\rho - \partial_{0\gamma}(\rho u_\alpha u_\beta u_\gamma) - c_s^2\nabla_0(\rho u)\delta_{\alpha\beta}
\end{aligned} \tag{A.14}$$

and

$$\begin{aligned}
\partial_{0\gamma}[\rho c_s^2(\delta_{\alpha\beta}u_\gamma + \delta_{\alpha\gamma}u_\beta + \delta_{\beta\gamma}u_\alpha] = c_s^2\nabla_0(\rho u)\delta_{\alpha\beta} + \rho c_s^2\partial_{0\alpha}u_\beta + c_s^2 u_\beta\partial_{0\alpha}\rho + \rho c_s^2\partial_{0\beta}u_\alpha \\
+ c_s^2 u_\alpha\partial_{0\beta}\rho
\end{aligned} \tag{A.15}$$

Now we have

$$-\frac{1}{\tau\delta_t}\sum_i c_{i\alpha}c_{i\beta}f_i^{(1)} = \rho c_s^2(\partial_{0\alpha}u_\beta + \partial_{0\beta}u_\alpha) - \partial_{0\gamma}(\rho u_\alpha u_\beta u_\gamma) \tag{A.16}$$

So Eq. (A.12) can be written as

$$\frac{\partial}{\partial t_1}(\rho\mathbf{u}) + \left(1 - \frac{1}{2\tau}\right)\nabla_0 \cdot (-\tau\delta_t[\rho c_s^2(\partial_{0\alpha}u_\beta + \partial_{0\beta}u_\alpha) - \partial_{0\gamma}(\rho u_\alpha u_\beta u_\gamma)]) = 0 \tag{A.17}$$

which is equivalent to

$$\frac{\partial}{\partial t_1}(\rho\mathbf{u}) + \nabla \cdot [(-\rho\nu(\nabla\mathbf{u} + (\nabla\mathbf{u})^T) + \frac{\nu}{c_s^2}\nabla(\rho\mathbf{uuu})] = 0 \tag{A.18}$$

Eq. (A.9) can be rewritten as

$$\frac{\partial}{\partial t_0}(\rho \mathbf{u}) + \nabla \cdot (\rho \mathbf{u}\mathbf{u}) = -\nabla p \tag{A.19}$$

combining Eqs. (A.18) and (A.19), we can get the following equation,

$$\frac{\partial}{\partial t}(\rho \mathbf{u}) + \nabla \cdot (\rho \mathbf{u}\mathbf{u}) = -\nabla p + \nabla \cdot [\rho\nu(\nabla \mathbf{u} + (\nabla \mathbf{u})^T) - \frac{\nu}{c_s^2}\nabla(\rho \mathbf{u}\mathbf{u}\mathbf{u})] \tag{A.20}$$

Similarly, combining Eqs. (A.8) and (A.11), we can get the macroscopic equation as follows

$$\frac{\partial \rho}{\partial t} + \nabla \cdot (\rho \mathbf{u}) = 0 \tag{A.21}$$

It should be noted that the kinematic viscosity is given by $\nu = c_s^2(\tau - \frac{1}{2})\delta_t$ and $c_s = c/\sqrt{3}$ for the D2Q9 model. In small Mach number limit, the density of the fluid ρ is almost the same as ρ_0 calculated from the equilibrium distribution function, i.e. $\rho = \rho_0 = const.$ Thus the incompressible Navier-Stokes equations can be further obtained

$$\nabla \cdot \mathbf{u} = 0, \tag{A.22}$$

$$\frac{\partial \mathbf{u}}{\partial t} + \mathbf{u} \cdot \nabla \mathbf{u} = -\frac{1}{\rho}\nabla p + \nu \nabla^2 \mathbf{u}. \tag{A.23}$$

It is noted that the density variation of a flow is proportional to the square of the Mach number, i.e., the LBGK method is actually an artificially compressible method for the incompressible Navier-Stokes equations.

Appendix B

Derivation of the Burdine's law with the bundle of tubes model

Consider the drainage process, imagine now that we have a bundle of cylindrical tubes whose radii vary within the range of (r_1, r_2) with a distribution function $\alpha(r)$. Thus the nonwetting fluid occupies all pores larger than a size r' at the value of capillary pressure P_c,

$$r' = 2\sigma/P_c, \tag{B.1}$$

where r' is any value between (r_1, r_2). Thus the wetting fluid volume is

$$V_e = \int_{r_1}^{r'} \pi r^2 \alpha(r) dr, \tag{B.2}$$

from which the wetting fluid saturation S_e is

$$S_e = \int_{r_1}^{r'} \pi r^2 \alpha(r) dr / \int_{r_1}^{r_2} \pi r^2 \alpha(r) dr. \tag{B.3}$$

The change in saturation with radius is

$$r\frac{dS_e}{dr} = \frac{dS_e}{d\ln r} = \frac{r^3\alpha(r)}{\int_{r_1}^{r_2} r^2\alpha(r)dr} = G(r), \tag{B.4}$$

where $G(r)$ is the normalized distribution of volume on a logarithmic scale of radius and it is straightforward to write that

$$\int_{r_1}^{r_2} \frac{G(r)}{r} dr = 1. \tag{B.5}$$

Hence we can infer the distribution function $\alpha(r)$ of throat radius from the measured capillary pressure as a function of saturation $P_c = P_c(S_e)$. Using Eq. (B.1) and (B.4), we can write

$$\frac{dP_c}{dS_e} = \frac{dP_c}{dr}\frac{dr}{dS_e} = -\frac{P_c}{G(r)}, \tag{B.6}$$

from which we find

$$G(r) = -P_c\frac{dS_e}{dP_c} = -\frac{dS_e}{d\ln P_c}, \tag{B.7}$$

where $G(r)$ is also called the apparent throat size distribution and is routinely measured [1].

Assuming that the bundle is cut into a large number of thin slices then the short tubes in each slice are rearranged randomly and the slices are reassembled also randomly. In any slice of area A of the model, the area occupied by the wetting fluid is nS_eA in pores of radii between r_1 and r'. Because of the tubes model, an equal area is occupied by the wetting fluid in the neighbouring slices. However, not all of these areas are connected because of the random distribution of the pores in each slice. We use λ, called the pore-size distribution index, to characterize how the available interconnected total pore area is distributed, it also depends on $\alpha(r)$.

Considering a point on the interface between two neighbouring slices, the probability that it lies in the wetting fluid in each slice is nS_e. Similarly, the probability of a wetting-fluid-filled pore in a slice is nS_e, the area common to a **single pore** of cross-sectional area πr^2 in one slice and all the wetting-fluid-filled pores in a neighbouring slice, is therefore $\pi r^2 nS_e$. Thus the passage of wetting fluid takes place from an area πr^2 to a constricted area $\pi r^2 nS_e$. One may visualize the constricted area as a pore of smaller radius r'' so that

$$\lambda\pi r''^2 = \pi r^2 nS_e, \tag{B.8}$$

or

$$r'' = (nS_e/\lambda)^{1/2}r. \tag{B.9}$$

We now use the Poiseuille's law to describe the flow through the capillary model,

$$Q_v = -(\pi r''^4\gamma/8\mu)J = -\frac{\pi r^4 n^2 {S_e}^2\gamma}{8\mu\lambda^2}J, \tag{B.10}$$

where J is the pressure gradient in terms of piezometric head. Assuming that λ is independent of $\alpha(r)$, the specific discharge $q = Q/A$ is given by

$$q = -\frac{\pi n^3 {S_e}^2\gamma}{8\mu\lambda^2}J\frac{\int_{r_1}^{r'} r^4\alpha(r)dr}{\int_{r_1}^{r_2}\pi r^2\alpha(r)dr}, \tag{B.11}$$

where $Q = \int_{r_1}^{r'} Q_v \alpha(r) dr$ and $nA = \int_{r_1}^{r_2} \pi r^2 \alpha(r) dr$.

Equation (B.4) can be rewritten as

$$dr = \frac{\left(\int_{r_1}^{r_2} r^2 \alpha(r) dr\right) dS_e}{r^2 \alpha(r)}. \tag{B.12}$$

Now from Eq. (B.1) and (B.12), Equation (B.11) can be written as

$$q = -\frac{\pi n^3 {S_e}^2 \gamma}{8\mu\lambda^2} J \frac{\int_{r_1}^{r'} r^2 \left(\int_{r_1}^{r_2} r^2 \alpha(r) dr\right) dS_e}{\int_{r_1}^{r_2} \pi r^2 \alpha(r) dr} = -\frac{n^3 S_e^2 \gamma \sigma^2}{2\mu\lambda^2} J \int_0^{S_e} \frac{dS'_e}{P_c^2(S'_e)}, \tag{B.13}$$

Therefore,

$$q = \frac{k_w \gamma}{\mu} J, \quad k_w = \frac{n^3 S_e^2 \sigma^2}{2\lambda^2} \int_0^{S_e} \frac{dS'_e}{P_c^2(S'_e)}, \quad k = \frac{n^3 \sigma^2}{2\lambda^2} \int_0^1 \frac{dS'_e}{P_c^2(S'_e)}, \tag{B.14}$$

under the assumption that $1/\lambda^2$ is not a sensitive function of S_w. Thus

$$k_{rw} = (S_e)^2 \frac{\int_0^{S_e} \frac{dS'_e}{P_c^2(S'_e)}}{\int_0^1 \frac{dS'_e}{P_c^2(S'_e)}}. \tag{B.15}$$

Similarly,

$$k_{rnw} = (1 - S_e)^2 \frac{\int_{S_e}^1 \frac{dS'_e}{P_c^2(S'_e)}}{\int_0^1 \frac{dS'_e}{P_c^2(S'_e)}}. \tag{B.16}$$

Appendix C

Derivation and theoretical solutions to the governing equation for capillary filling

Here, we shall present the derivation of the Eqn. (4.1) for the capillary filling. As shown in Fig. C.1, in a 2D channel the volumetric flow rate can be defined by

$$Q = \frac{H^3}{12\eta_B}\frac{p_{in} - p_1}{x}, \tag{C.1}$$

and also by

$$Q = \frac{H^3}{12\eta_R}\frac{p_2 - p_{out}}{L - x}. \tag{C.2}$$

Equation.(C.1) and Eqn.(C.2) can be rewritten as

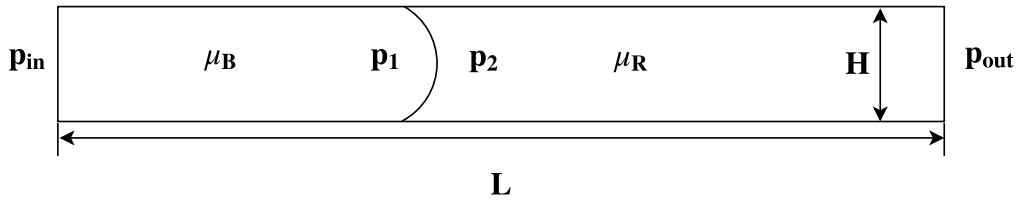

Figure C.1: The schematic diagram for the displacement of a wetting fluid with a non-wetting fluid in a capillary tube with a constant pressure differential.

$$p_{in} - p_1 = \frac{12\eta_B Q x}{H^3}, \tag{C.3}$$

$$p_2 - p_{out} = \frac{12\eta_R Q(L-x)}{H^3}. \tag{C.4}$$

Then we take the sum, which leads to

$$p_{in} - p_1 + p_2 - p_{out} = \frac{12\eta_B Qx + 12\eta_R Q(L-x))}{H^3}, \tag{C.5}$$

Hence,

$$Q = \frac{(p_{in} - p_{out} - p_1 + p_2)H^3}{12(\eta_B - \eta_R)x + 12\eta_R L}. \tag{C.6}$$

From $v = \frac{dx}{dt}$, we can write the following

$$\frac{dx}{dt} = \frac{(p_{in} - p_{out} - p_1 + p_2)H^2}{12(\eta_B - \eta_R)x + 12\eta_R L}. \tag{C.7}$$

The capillary pressure across the interface gives that

$$p_1 - p_2 = \frac{2\sigma\cos\theta}{H}. \tag{C.8}$$

This can be used in Eqn. (C.7) and we obtain

$$\frac{dx}{dt} = \frac{\left(p_{in} - p_{out} - \frac{2\sigma\cos\theta}{H}\right)H^2}{12(\eta_B - \eta_R)x + 12\eta_R L}. \tag{C.9}$$

It is easy to be seen that Eqn. (C.9) is another form of Eqn. (4.1). Now we are looking for the solution for this equation. It can be rearranged as

$$\left[12(\eta_B - \eta_R)x + 12\eta_R L\right]dx = \left(p_{in} - p_{out} - \frac{2\sigma\cos\theta}{H}\right)H^2 dt, \tag{C.10}$$

The following expression is obtained by integrating both sides of the equation

$$6(\eta_B - \eta_R)x^2 + 12\eta_R Lx = \left(p_{in} - p_{out} - \frac{2\sigma\cos\theta}{H}\right)H^2 t. \tag{C.11}$$

The above equation is a quadratic formula when $\eta_B \neq \eta_R$. Here are the solutions to the above equation:

- $\eta_B = \eta_R$,

$$x = \frac{H^2}{12} \cdot \frac{p_{in} - p_{out} - \frac{2\sigma\cos\theta}{H}}{\eta_R L} \cdot t, \tag{C.12}$$

- $\eta_B > \eta_R$,

$$x = -\frac{\eta_R L}{\eta_B - \eta_R} + \sqrt{\frac{\eta_R^2 L^2}{(\eta_B - \eta_R)^2} + \frac{H^2}{6} \cdot \frac{p_{in} - p_{out} - \frac{2\sigma\cos\theta}{H}}{\eta_B - \eta_R} \cdot t}, \tag{C.13}$$

- $\eta_B < \eta_R$,

$$x = -\frac{\eta_R L}{\eta_B - \eta_R} - \sqrt{\frac{\eta_R^2 L^2}{(\eta_B - \eta_R)^2} + \frac{H^2}{6} \cdot \frac{p_{in} - p_{out} - \frac{2\sigma \cos\theta}{H}}{\eta_B - \eta_R} \cdot t}. \tag{C.14}$$

By setting $x = L$ in Eqn. (C.11), the breakthrough time is obtained as shown in Eqn. (4.2).

Appendix D

The effect of wettability

To investigate the effect of wettability on the fluid displacement during the imbibition process, four preliminary tests have been carried out for the primary geometry with contact angles of $\pi/10$, $\pi/8$, $\pi/6$ and $\pi/4$. The other parameters are chosen as the default values. Figure D.1 shows the final fluid distributions for different contact angles. It can be observed that as the contact angle decreases from $\pi/4$ to $\pi/10$, the amount of water that can be imbibed into the matrix keeps increasing. Fig. D.2 plots the time evolution of the oil recovery factor. It is seen that both the imbibition rate and the ultimate oil recovery increase as the contact angle decreases, consistent with the previous numerical results [50].

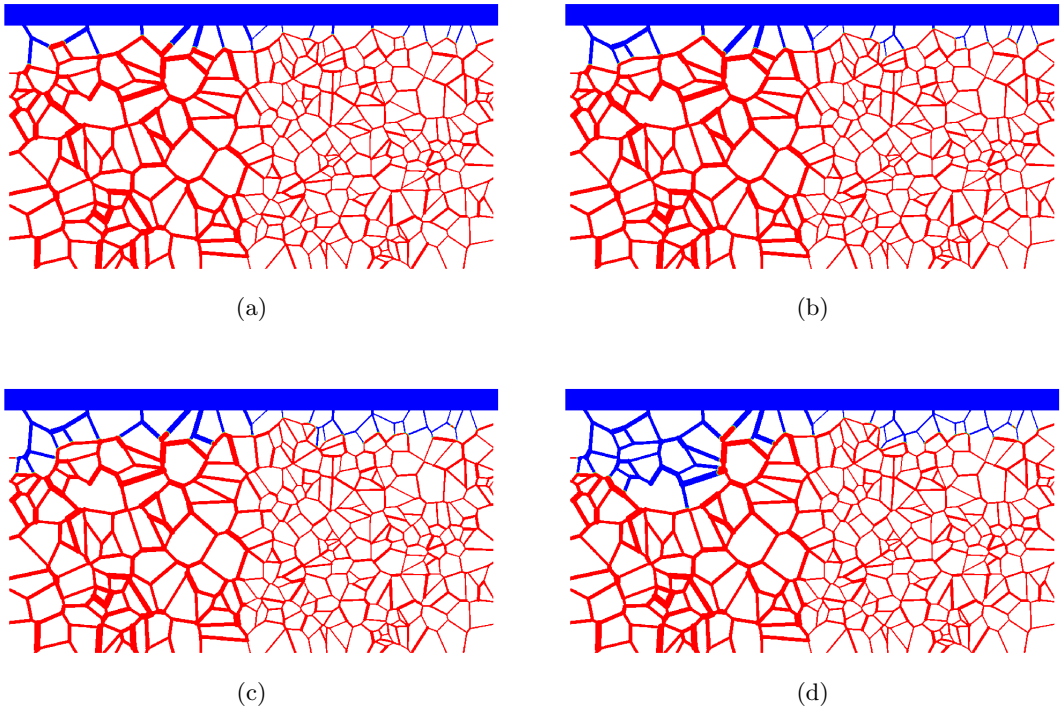

Figure D.1: Final fluid distributions for different contact angles: (a) $\theta = \pi/4$; (b) $\theta = \pi/6$; (c) $\theta = \pi/8$ and (d) $\theta = \pi/10$. Note that the water and the oil are shown in blue and red, respectively.

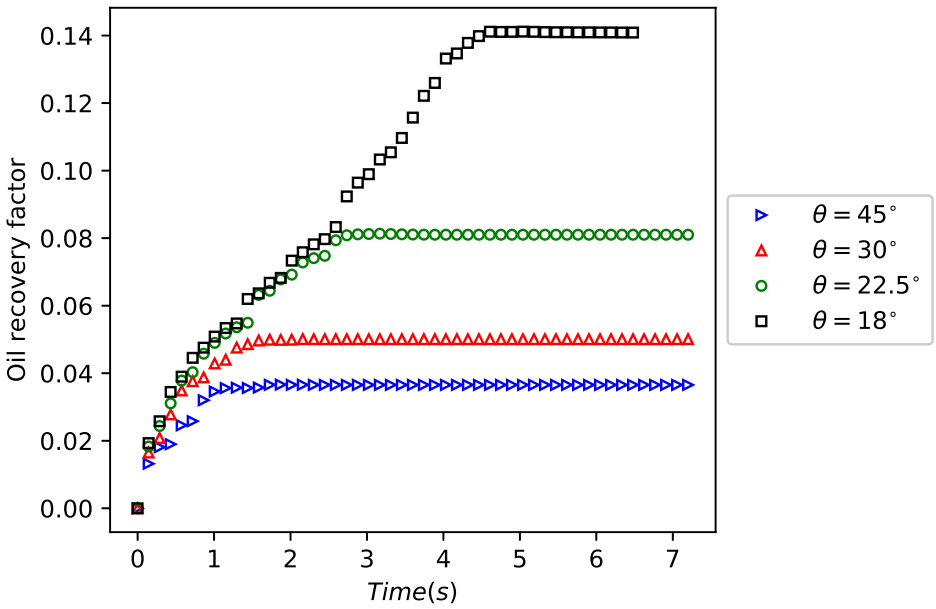

Figure D.2: The oil recovery factor as a function of time for the contact angles of $\pi/4$, $\pi/6$, $\pi/8$ and $\pi/10$.

Bibliography

[1] MJ Blunt. *Multiphase Flow in Permeable Media: A Pore-Scale Perspective*. Cambridge University Press, February 2017. xiv, 2, 3, 52, 106

[2] Changyong Zhang, Mart Oostrom, Thomas W. Wietsma, Jay W. Grate, and Marvin G. Warner. **Influence of Viscous and Capillary Forces on Immiscible Fluid Displacement: Pore-Scale Experimental Study in a Water-Wet Micromodel Demonstrating Viscous and Capillary Fingering**. *Energy & Fuels*, **25**:3493–3505, 2011. xiv, 5, 6, 66

[3] Roland Lenormand, Eric Touboul, and Cesar Zarcone. **Numerical Models and Experiments on Immiscible Displacements in Porous Media**. *Journal of Fluid Mechanics*, **189**:165, 1988. xiv, 5, 6

[4] Qisu Zou and Xiaoyi He. **On Pressure and Velocity Boundary Conditions for the Lattice Boltzmann BGK Model**. *Physics of Fluids*, **9**:1591–1598, June 1997. xiv, 23, 56, 58, 60

[5] X. D. Niu, C. Shu, Y. T. Chew, and T. G. Wang. **Investigation of Stability and Hydrodynamics of Different Lattice Boltzmann Models**. *Journal of Statistical Physics*, **117**:665–680, November 2004. xv, 36

[6] Yan Ba, Haihu Liu, Jinju Sun, and Rongye Zheng. **Color-Gradient Lattice Boltzmann Model for Simulating Droplet Motion with Contact-Angle Hysteresis**. *Physical Review E*, **88**:043306, October 2013. xv, xx, 38, 39

[7] Takashi Akai, Branko Bijeljic, and Martin J Blunt. **Wetting Boundary Condition for the Lattice Boltzmann Method : Validation with Analytical and Experimental Data**. *Advances in Water Resources*, **116**:56–66, 2018. xv, 38, 43

[8] Jacob Bear and J-M. Buchlin. *Modelling and Applications of Transport Phenomena in Porous Media*. 1987. xv, 47

[9] Jacob Bear. *Dynamics of Fluids in Porous Media*. Dover, Mineola, New York, 1972. xv, 1, 48, 50, 52, 58, 63

[10] Norman R Morrow and Geoffrey Mason. **Recovery of Oil by Spontaneous Imbibition**. *Current Opinion in Colloid & Interface Science*, **6**:321–337, August 2001. 1, 75

[11] R. Juanes, E. J. Spiteri, F. M. Orr, and M. J. Blunt. **Impact of Relative Permeability Hysteresis on Geological CO2 Storage**. *Water Resources Research*, **42**, 2006. 2

[12] Thomas Ramstad, Pål-Eric Øren, and Stig Bakke. **Simulation of Two-Phase Flow in Reservoir Rocks Using a Lattice Boltzmann Method**. *SPE Journal*, **15**:1–11, 2010. 3, 24, 38

[13] Mehran Pooladi-Darvish and Abbas Firoozabadi. **Cocurrent and Countercurrent Imbibition in a Water-Wet Matrix Block**. *SPE Journal*, **5**:3–11, March 2000. 3

[14] Jay W. Grate, Marvin G. Warner, Jonathan W. Pittman, Karl J. Dehoff, Thomas W. Wietsma, Changyong Zhang, and Mart Oostrom. **Silane Modification of Glass and Silica Surfaces to Obtain Equally Oil-Wet Surfaces in Glass-Covered Silicon Micromodel Applications**. *Water Resources Research*, **49**:4724–4729, 2013. 4

[15] R. Lenormand, C. Zarcone, and A. Sarr. **Mechanisms of the Displacement of One Fluid by Another in a Network of Capillary Ducts**. *Journal of Fluid Mechanics*, **135**:337–353, October 1983. 4, 9

[16] Vidar Frette, Jens Feder, Torstein Jøssang, Paul Meakin, and Knut Jørgen Måløy. **Fast, Immiscible Fluid-Fluid Displacement in Three-Dimensional Porous Media at Finite Viscosity Contrast**. *Physical Review E*, **50**:2881–2890, October 1994. 6

[17] M. Ferer, Chuang Ji, Grant S. Bromhal, Joshua Cook, Goodarz Ahmadi, and Duane H. Smith. **Crossover from Capillary Fingering to Viscous Fingering for Immiscible Unstable Flow: Experiment and Modeling**. *Physical Review E*, **70**:016303, July 2004. 6

[18] Christophe Cottin, Hugues Bodiguel, and Annie Colin. **Drainage in Two-Dimensional Porous Media: From Capillary Fingering to Viscous Flow**. *Physical Review E*, **82**:046315, October 2010. 6

[19] Ying Wang, Changyong Zhang, Ning Wei, Mart Oostrom, Thomas W. Wietsma, Xiaochun Li, and Alain Bonneville. **Experimental Study of Crossover from Capillary to Viscous Fingering for Supercritical CO2–Water Displacement in a Homogeneous Pore Network**. *Environmental Science & Technology*, **47**:212–218, January 2013. 6

[20] Takeshi Tsuji, Fei Jiang, and Kenneth T. Christensen. **Characterization of Immiscible Fluid Displacement Processes with Various Capillary Numbers and Viscosity Ratios in 3D Natural Sandstone**. *Advances in Water Resources*, **95**:3–15, September 2016. 6

[21] Paul Meakin and Alexandre M. Tartakovsky. **Modeling and Simulation of Pore-Scale Multiphase Fluid Flow and Reactive Transport in Fractured and Porous Media**. *Reviews of Geophysics*, **47**, September 2009. 6

[22] Martin J. Blunt, Branko Bijeljic, Hu Dong, Oussama Gharbi, Stefan Iglauer, Peyman Mostaghimi, Adriana Paluszny, and Christopher Pentland. **Pore-Scale Imaging and Modelling**. *Advances in Water Resources*, **51**:197–216, January 2013. 6

[23] Thomas Ramstad, Nasiru Idowu, Cyril Nardi, and Pål-Eric Øren. **Relative Permeability Calculations from Two-Phase Flow Simulations Directly on Digital Images of Porous Rocks**. *Transport in Porous Media*, **94**:487–504, September 2012. 6, 7, 8, 38

[24] Shiyi Chen and Gary D Doolen. **Lattice Boltzmann Method for Fluid Flows**. *Annual review of fluid mechanics*, **30**:329–364, 1998. 6, 26

[25] Mark Sussman, Peter Smereka, and Stanley Osher. **A Level Set Approach for Computing Solutions to Incompressible Two-Phase Flow**. *Journal of Computational Physics*, **114**:146–159, September 1994. 6

[26] C. W Hirt and B. D Nichols. **Volume of Fluid (VOF) Method for the Dynamics of Free Boundaries**. *Journal of Computational Physics*, **39**:201–225, January 1981. 6

[27] Ruben Scardovelli and Stéphane Zaleski. **Direct Numerical Simulation of Free-Surface and Interfacial Flow**. *Annual Review of Fluid Mechanics*, **31**:567–603, 1999. 6

[28] Ali Q. Raeini, Martin J. Blunt, and Branko Bijeljic. **Modelling Two-Phase Flow in Porous Media at the Pore Scale Using the Volume-of-Fluid Method**. *Journal of Computational Physics*, **231**:5653–5668, July 2012. 6

[29] Andrea Ferrari and Ivan Lunati. **Direct Numerical Simulations of Interface Dynamics to Link Capillary Pressure and Total Surface Energy**. *Advances in Water Resources*, **57**:19–31, July 2013. 6

[30] V. E. Badalassi, H. D. Ceniceros, and S. Banerjee. **Computation of Multiphase Systems with Phase Field Models**. *Journal of Computational Physics*, **190**:371–397, September 2003. 6

[31] Abdelkader Krimi, Mehdi Rezoug, Sofiane Khelladi, Xesús Nogueira, Michael Deligant, and Luis Ramírez. **Smoothed Particle Hydrodynamics: A Consistent Model for Interfacial Multiphase Fluid Flow Simulations**. *Journal of Computational Physics*, **358**:53–87, April 2018. 6

[32] Bruno Ferréol and Daniel H. Rothman. **Lattice-Boltzmann Simulations of Flow through Fontainebleau Sandstone**. *Transport in Porous Media*, **20**:3–20, August 1995. 7

[33] Nicos S. Martys and Hudong Chen. **Simulation of Multicomponent Fluids in Complex Three-Dimensional Geometries by the Lattice Boltzmann Method**. *Physical Review E*, **53**:743–750, January 1996. 7

[34] Tölke Jonas, Krafczyk Manfred, Schulz Manuel, and Rank Ernst. **Lattice Boltzmann Simulations of Binary Fluid Flow through Porous Media**. *Philosophical Transactions of the Royal Society of London. Series A: Mathematical, Physical and Engineering Sciences*, **360**:535–545, March 2002. 7, 10, 33

[35] Gunstensen K. Andrew and Daniel H. Rothman. **Lattice Boltzmann Model of Immiscible Fluids**. *Physical Review A*, **43**:4320–4327, 1991. 7, 24, 25, 29, 33

[36] C. Pan, M. Hilpert, and C. T. Miller. **Lattice-Boltzmann Simulation of Two-Phase Flow in Porous Media**. *Water Resources Research*, **40**, 2004. 7

[37] C. Manwart, U. Aaltosalmi, A. Koponen, R. Hilfer, and J. Timonen. **Lattice-Boltzmann and Finite-Difference Simulations for the Permeability for Three-Dimensional Porous Media**. *Physical Review E*, **66**:016702, July 2002. 7

[38] H.-J. Vogel, J. Tölke, V. P. Schulz, M. Krafczyk, and K. Roth. **Comparison of a Lattice-Boltzmann Model, a Full-Morphology Model, and a Pore Network Model for Determining Capillary Pressure–Saturation Relationships**. *Vadose Zone Journal*, **4**:380–388, May 2005. 8

[39] Huina Li, Chongxun Pan, and Cass T. Miller. **Pore-Scale Investigation of Viscous Coupling Effects for Two-Phase Flow in Porous Media**. *Physical Review E*, **72**:026705, August 2005. 8

[40] Marcel G. Schaap, Mark L. Porter, Britt S. B. Christensen, and Dorthe Wildenschild. **Comparison of Pressure-Saturation Characteristics Derived from Computed Tomography and Lattice Boltzmann Simulations**. *Water Resources Research*, **43**, 2007. 8

[41] B. Ahrenholz, J. Tölke, P. Lehmann, A. Peters, A. Kaestner, M. Krafczyk, and W. Durner. **Prediction of Capillary Hysteresis in a Porous Material Using Lattice-Boltzmann Methods and Comparison to Experimental Data and a Morphological Pore Network Model**. *Advances in Water Resources*, **31**:1151–1173, September 2008. 8

[42] Qinjun Kang, Dongxiao Zhang, and Shiyi Chen. **Immiscible Displacement in a Channel: Simulations of Fingering in Two Dimensions**. *Advances in Water Resources*, **27**:13–22, January 2004. 8

[43] A. G. Yiotis, L. Talon, and D. Salin. **Blob Population Dynamics during Immiscible Two-Phase Flows in Reconstructed Porous Media**. *Physical Review E*, **87**:033001, March 2013. 8

[44] Haihu Liu, Albert J. Valocchi, Charles Werth, Qinjun Kang, and Mart Oostrom. **Pore-Scale Simulation of Liquid CO2 Displacement of Water Using a Two-Phase Lattice Boltzmann Model**. *Advances in Water Resources*, **73**:144–158, 2014. 8, 38, 60

[45] Haihu Liu, Yonghao Zhang, and Albert J. Valocchi. **Lattice Boltzmann Simulation of Immiscible Fluid Displacement in Porous Media: Homogeneous versus Heterogeneous Pore Network**. *Physics of Fluids*, **27**:052103, 2015. 8

[46] Yuan Yu, Haihu Liu, Yonghao Zhang, and Dong Liang. **Color-Gradient Lattice Boltzmann Modeling of Immiscible Two-Phase Flows on Partially Wetting Surfaces**. *Proceedings of the Institution of Mechanical Engineers, Part C: Journal of Mechanical Engineering Science*, **232**:416–430, February 2018. 8, 40

[47] Zi Li, Sergio Galindo-Torres, Guanxi Yan, Alexander Scheuermann, and Ling Li. **A Lattice Boltzmann Investigation of Steady-State Fluid Distribution, Capillary Pressure and Relative Permeability of a Porous Medium: Effects of Fluid and Geometrical Properties**. *Advances in Water Resources*, **116**:153–166, June 2018. 8

[48] A. M. Saidi. **Simulation of Naturally Fractured Reservoirs**. In *SPE Reservoir Simulation Symposium*. Society of Petroleum Engineers, January 1983. 9

[49] Haibo Li, Hekun Guo, Zhengming Yang, Hongmei Ren, Lixin Meng, Haibing Lu, Hongcheng Xu, Yuping Sun, Tiening Gao, and Hewen Zhang. **Evaluation of Oil Production Potential in Fractured Porous Media**. *Physics of Fluids*, **31**:052104, May 2019. 9

[50] M. R. Rokhforouz and H. A. Akhlaghi Amiri. **Phase-Field Simulation of Counter-Current Spontaneous Imbibition in a Fractured Heterogeneous Porous Medium**. *Physics of Fluids*, **29**:062104, June 2017. 9, 10, 75, 93, 94, 111

[51] C. C. Mattax and J. R. Kyte. **Imbibition Oil Recovery from Fractured, Water-Drive Reservoir**. *Society of Petroleum Engineers Journal*, **2**:177–184, June 1962. 9

[52] L.E. Cuiec, B. Bourbiaux, and F. Kalaydjian. **Oil Recovery by Imbibition in Low-Permeability Chalk**. *SPE Formation Evaluation*, **9**:200–208, September 1994. 9

[53] Xiaoyun Zhang, Norman R. Morrow, and Shouxiang Ma. **Experimental Verification of a Modified Scaling Group for Spontaneous Imbibition**. *SPE Reservoir Engineering*, **11**:280–285, November 1996. 9

[54] Ma Shouxiang, Norman R. Morrow, and Xiaoyun Zhang. **Generalized Scaling of Spontaneous Imbibition Data for Strongly Water-Wet Systems**. *Journal of Petroleum Science and Engineering*, **18**:165–178, November 1997. 9

[55] Iman Jafari, Mohsen Masihi, and Masoud Nasiri Zarandi. **Numerical Simulation of Counter-Current Spontaneous Imbibition in Water-Wet Fractured Porous Media: Influences of Water Injection Velocity, Fracture Aperture, and Grains Geometry**. *Physics of Fluids*, **29**:113305, November 2017. 9, 10, 75

[56] Ole Torsaeter. **An Experimental Study of Water Imbibition in Chalk From the Ekofisk Field**. In *SPE Enhanced Oil Recovery Symposium*. Society of Petroleum Engineers, January 1984. 9

[57] R. W. Parsons and P. R. Chaney. **Imbibition Model Studies on Water-Wet Carbonate Rocks**. *Society of Petroleum Engineers Journal*, **6**:26–34, March 1966. 9

[58] P.M. Blair. **Calculation of Oil Displacement by Countercurrent Water Imbibition**. *Society of Petroleum Engineers Journal*, **4**:195–202, September 1964. 9

[59] Al Muatasim Al Bahlani and Tayfun Babadagli. **Heavy-Oil Recovery in Naturally Fractured Reservoirs with Varying Wettability by Steam Solvent Co-Injection**. In *International Thermal Operations and Heavy Oil Symposium*. Society of Petroleum Engineers, January 2008. 9

[60] T Babadagli, A Al-Bemani, and F Boukadi. **Analysis of Capillary Imbibition Recovery Considering the Simultaneous Effects of Gravity, Low IFT, and Boundary Conditions**. *Society of Petroleum Engineers*, page 9, January 1999. 9

[61] D. S Schechter, D Zhou, and F. M Orr. **Low IFT Drainage and Imbibition**. *Journal of Petroleum Science and Engineering*, **11**:283–300, September 1994. 9

[62] E. R. Brownscombe and A. B. Dyes. **Water-Imbibition Displacement-A Possibility for the Spraberry**. In *Drilling and Production Practice*. American Petroleum Institute, January 1952. 9

[63] Liang Cheng Chang, Jui Pin Tsai, Hsin Yu Shan, and Hung Hui Chen. **Experimental Study on Imbibition Displacement Mechanisms of Two-Phase Fluid Using Micro Model**. *Environmental Earth Sciences*, **59**:901–911, 2009. 9

[64] V. Joekar Niasar, S. M. Hassanizadeh, L. J. Pyrak-Nolte, and C. Berentsen. **Simulating Drainage and Imbibition Experiments in a High-Porosity Micromodel Using an Unstructured Pore Network Model**. *Water Resources Research*, **45**, 2009. 9

[65] Benyamin Yadali Jamaloei, Koorosh Asghari, Riyaz Kharrat, and Farid Ahmadloo. **Pore-Scale Two-Phase Filtration in Imbibition Process through Porous Media at High- and Low-Interfacial Tension Flow Conditions**. *Journal of Petroleum Science and Engineering*, **72**:251–269, June 2010. 9

[66] E. R. Rangel-German and A. R. Kovscek. **Experimental and Analytical Study of Multidimensional Imbibition in Fractured Porous Media**. *Journal of Petroleum Science and Engineering*, **36**:45–60, October 2002. 9, 85

[67] Iman Jafari, Mohsen Masihi, and Masoud Nasiri Zarandi. **Experimental Study on Imbibition Displacement Mechanisms of Two-Phase Fluid Using Micromodel: Fracture Network, Distribution of Pore Size, and Matrix Construction**. *Physics of Fluids*, **29**:122004, December 2017. 10

[68] Akshay Gunde, Tayfun Babadagli, Susanta Sinha Roy, and Sushanta Kumar Mitra. **Pore-Scale Interfacial Dynamics and Oil–Water Relative Permeabilities of Capillary Driven Counter-Current Flow in Fractured Porous Media**. *Journal of Petroleum Science and Engineering*, **103**:106–114, 2013. 10, 38, 75, 78

[69] Zhiyuan Xu, Haihu Liu, and Albert J. Valocchi. **Lattice Boltzmann Simulation of Immiscible Two-Phase Flow with Capillary Valve Effect in Porous Media**. *Water Resources Research*, **53**:3770–3790, 2017. 10, 12, 40, 42, 43, 75

[70] H Huang, M Sukop, and Xi-Yun Lu. *Multiphase Lattice Boltzmann Methods: Theory and Application*. 2015. 10, 26

[71] Haihu Liu, Qinjun Kang, Christopher R. Leonardi, Sebastian Schmieschek, Ariel Narváez, Bruce D. Jones, John R. Williams, Albert J. Valocchi, and Jens Harting. **Multiphase Lattice Boltzmann Simulations for Porous Media Applications**. *Computational Geosciences*, pages 777–805, 2015. 10, 26

[72] Qingqing Gu, Haihu Liu, and Yonghao Zhang. **Lattice Boltzmann Simulation of Immiscible Two-Phase Displacement in Two-Dimensional Berea Sandstone**. *Applied Sciences*, **8**:1497, 2018. 10

[73] Haibo Huang, Jun-Jie Huang, and Xi-Yun Lu. **Study of Immiscible Displacements in Porous Media Using a Color-Gradient-Based Multiphase Lattice Boltzmann Method**. *Computers & Fluids*, **93**:164–172, April 2014. 10, 38

[74] Yu Chen, Yaofa Li, Albert J. Valocchi, and Kenneth T. Christensen. **Lattice Boltzmann Simulations of Liquid CO2 Displacing Water in a 2D Heterogeneous Micromodel at Reservoir Pressure Conditions**. *Journal of Contaminant Hydrology*, **212**:14–27, May 2018. 10

[75] Meng Xu and Haihu Liu. **Prediction of Immiscible Two-Phase Flow Properties in a Two-Dimensional Berea Sandstone Using the Pore-Scale Lattice Boltzmann Simulation**. *The European Physical Journal E*, **41**:124, October 2018. 10

[76] Zhaoli Guo and Chang Shu. *Lattice Boltzmann Method and Its Applications in Engineering*. May 2013. 15, 46

[77] Prabhu Lal Bhatnagar, Eugene P Gross, and Max Krook. **A Model for Collision Processes in Gases. I. Small Amplitude Processes in Charged and Neutral One-Component Systems**. *Physical review*, **94**:511, 1954. 16

[78] Y. H. Qian, D. d'Humières, and P. Lallemand. **Lattice BGK Models for Navier-Stokes Equation**. *Europhysics Letters*, **17**:479–484, February 1992. 18, 20

[79] Xiaowen Shan, Xue-Feng Yuan, and Hudong Chen. **Kinetic Theory Representation of Hydrodynamics: A Way beyond the Navier–Stokes Equation**. *Journal of Fluid Mechanics*, **550**:413–441, March 2006. 18

[80] Li-Shi Luo. **Unified Theory of Lattice Boltzmann Models for Nonideal Gases**. *Physical Review Letters*, **81**:1618–1621, August 1998. 19

[81] Zhaoli Guo, Chuguang Zheng, and Baochang Shi. **Discrete Lattice Effects on the Forcing Term in the Lattice Boltzmann Method**. *Physical Review E*, **65**:046308, April 2002. 19, 30

[82] Takaji Inamuro, Masato Yoshino, and Fumimaru Ogino. **A Non-slip Boundary Condition for Lattice Boltzmann Simulations**. *Physics of Fluids*, **7**:2928–2930, December 1995. 20

[83] Chongxun Pan, Li-Shi Luo, and Cass T. Miller. **An Evaluation of Lattice Boltzmann Schemes for Porous Medium Flow Simulation**. *Computers & Fluids*, **35**:898–909, September 2006. 21

[84] Xiaoyi He, Qisu Zou, Li-Shi Luo, and Micah Dembo. **Analytic Solutions of Simple Flows and Analysis of Nonslip Boundary Conditions for the Lattice Boltzmann BGK Model**. *Journal of Statistical Physics*, **87**:115–136, April 1997. 21

[85] Seung Hyun Kim and Heinz Pitsch. **A Generalized Periodic Boundary Condition for Lattice Boltzmann Method Simulation of a Pressure Driven Flow in a Periodic Geometry**. *Physics of Fluids*, **19**:108101, October 2007. 22

[86] Qisu Zou, Shuling Hou, Shiyi Chen, and Gary D. Doolen. **A Improved Incompressible Lattice Boltzmann Model for Time-Independent Flows**. *Journal of Statistical Physics*, **81**:35–48, October 1995. 22

[87] Xiaoyi He and Li-Shi Luo. **Lattice Boltzmann Model for the Incompressible Navier–Stokes Equation**. *Journal of Statistical Physics*, **88**:927–944, August 1997. 22

[88] Daniel H. Rothman and Jeffrey M. Keller. **Immiscible Cellular-Automaton Fluids**. *Journal of Statistical Physics*, **52**:1119–1127, 1988. 24, 25

[89] X. Shan and H. Chen. **Lattice Boltzmann Model for Simulating Flows with Multi Phases and Components**. *Physical Review E*, **47**:1815–1819, 1993. 24, 25

[90] Michael Swift, E Orlandini, W. Osborn, and J. Yeomans. **Lattice Boltzmann Simulations of Liquid-Gas and Binary Fluid Systems**. *Physical Review E*, **54**:5041–5052, 1996. 24, 25

[91] Xiaoyi He, Xiaowen Shan, and Gary D. Doolen. **Discrete Boltzmann Equation Model for Nonideal Gases**. *Physical Review E*, **57**:R13–R16, 1998. 24, 25

[92] Haibo Huang, Manfred Krafczyk, and Xiyun Lu. **Forcing Term in Single-Phase and Shan-Chen-Type Multiphase Lattice Boltzmann Models**. *Physical Review E*, **84**:046710, October 2011. 25

[93] Q. Li, K. H. Luo, and X. J. Li. **Forcing Scheme in Pseudopotential Lattice Boltzmann Model for Multiphase Flows**. *Physical Review E*, **86**:016709, July 2012. 25

[94] Q. Li, K. H. Luo, and X. J. Li. **Lattice Boltzmann Modeling of Multiphase Flows at Large Density Ratio with an Improved Pseudopotential Model**. *Physical Review E*, **87**:053301, May 2013. 25

[95] Daniel Lycett-Brown and Kai H. Luo. **Improved Forcing Scheme in Pseudopotential Lattice Boltzmann Methods for Multiphase Flow at Arbitrarily High Density Ratios**. *Physical Review E*, **91**:023305, February 2015. 25

[96] Linlin Fei, Andrea Scagliarini, Andrea Montessori, Marco Lauricella, Sauro Succi, and Kai H. Luo. **Mesoscopic Model for Soft Flowing Systems with Tunable Viscosity Ratio**. *Physical Review Fluids*, **3**:104304, October 2018. 25

[97] A. N. Kalarakis, V. N. Burganos, and A. C. Payatakes. **Galilean-Invariant Lattice-Boltzmann Simulation of Liquid-Vapor Interface Dynamics**. *Physical Review E*, **65**:056702, April 2002. 25

[98] A. N. Kalarakis, V. N. Burganos, and A. C. Payatakes. **Three-Dimensional Lattice-Boltzmann Model of van Der Waals Fluids**. *Physical Review E*, **67**:016702, January 2003. 25

[99] Xiaoyi He, Shiyi Chen, and Raoyang Zhang. **A Lattice Boltzmann Scheme for Incompressible Multiphase Flow and Its Application in Simulation of Rayleigh–Taylor Instability**. *Journal of Computational Physics*, **152**:642–663, July 1999. 25

[100] J. S. Rowlinson and B. Widom. *Molecular Theory of Capillarity*. 1982. 26, 37, 38

[101] R. R. Nourgaliev, T. N. Dinh, T. G. Theofanous, and D. Joseph. **The Lattice Boltzmann Equation Method: Theoretical Interpretation, Numerics and Implications**. *International Journal of Multiphase Flow*, **29**:117–169, January 2003. 26

[102] Irina Ginzburg. **Equilibrium-Type and Link-Type Lattice Boltzmann Models for Generic Advection and Anisotropic-Dispersion Equation**. *Advances in water resources*, **28**:1171–1195, 2005. 27

[103] Irina Ginzburg, Frederik Verhaeghe, and Dominique d'Humieres. **Two-Relaxation-Time Lattice Boltzmann Scheme: About Parametrization, Velocity, Pressure and Mixed Boundary Conditions**. *Communications in computational physics*, **3**:427–478, 2008. 27

[104] Irina Ginzburg, Frederik Verhaeghe, and Dominique d'Humieres. **Study of Simple Hydrodynamic Solutions with the Two-Relaxation-Times Lattice Boltzmann Scheme**. *Communications in computational physics*, **3**:519–581, 2008. 27

[105] Kruger Timm, Halim Kusumaatmaja, and Alexandr Kuzmin. *The Lattice Boltzmann Method: Principles and Practice*. Springer, Switzerland, 2016. 27

[106] Irina Ginzburg and Dominique d'Humieres. **Multireflection Boundary Conditions for Lattice Boltzmann Models**. *Physical Review E*, **68**:066614, 2003. 28

[107] W. A. England, A. S. Mackenzie, D. M. Mann, and T. M. Quigley. **The Movement and Entrapment of Petroleum Fluids in the Subsurface**. *Journal of the Geological Society*, **144**:327–347, March 1987. 28

[108] YQ Zu and S He. **Phase-Field-Based Lattice Boltzmann Model for Incompressible Binary Fluid Systems with Density and Viscosity Contrasts**. *Physical Review E*, **87**:043301, 2013. 28

[109] Daryl Grunau, Shiyi Chen, and Kenneth Eggert. **A Lattice Boltzmann Model for Multiphase Fluid Flows**. *Physics of Fluids A: Fluid Dynamics*, **5**:2557–2562, 1993. 29

[110] T Reis and T N Phillips. **Lattice Boltzmann Model for Simulating Immiscible Two-Phase Flows**. *Journal of Physics A: Mathematical and Theoretical*, **40**:4033–4053, 2007. 29

[111] SV Lishchuk, CM Care, and I Halliday. **Lattice Boltzmann Algorithm for Surface Tension with Greatly Reduced Microcurrents**. *Physical Review E*, **67**:036701, 2003. 29

[112] J. U Brackbill, D. B Kothe, and C Zemach. **A Continuum Method for Modeling Surface Tension**. *Journal of Computational Physics*, **100**:335–354, June 1992. 30

[113] I Halliday, R Law, CM Care, and A Hollis. **Improved Simulation of Drop Dynamics in a Shear Flow at Low Reynolds and Capillary Number**. *Physical Review E*, **73**:056708, 2006. 30

[114] Haihu Liu, Albert J. Valocchi, and Qinjun Kang. **Three-Dimensional Lattice Boltzmann Model for Immiscible Two-Phase Flow Simulations**. *Physical Review E*, **85**:1–14, 2012. 31, 33

[115] M. Latva-Kokko and Daniel H. Rothman. **Diffusion Properties of Gradient-Based Lattice Boltzmann Models of Immiscible Fluids**. *Physical Review E*, **71**:1–8, 2005. 33

[116] U. D'Ortona, D. Salin, Marek Cieplak, Renata B. Rybka, and Jayanth R. Banavar. **Two-Color Nonlinear Boltzmann Cellular Automata: Surface Tension and Wetting**. *Physical Review E*, **51**:3718–3728, April 1995. 34

[117] I Halliday, AP Hollis, and CM Care. **Lattice Boltzmann Algorithm for Continuum Multicomponent Flow**. *Physical Review E*, **76**:026708, 2007. 34

[118] Anand Kumar. **Isotropic Finite-Differences**. *Journal of Computational Physics*, **201**:109–118, November 2004. 34

[119] Xiaowen Shan. **Analysis and Reduction of the Spurious Current in a Class of Multiphase Lattice Boltzmann Models**. *Physical Review E*, **73**:047701, April 2006. 34

[120] M. Sbragaglia, R. Benzi, L. Biferale, S. Succi, K. Sugiyama, and F. Toschi. **Generalized Lattice Boltzmann Method with Multirange Pseudopotential**. *Physical Review E*, **75**:1–13, 2007. 34, 43

[121] Sébastien Leclaire, Marcelo Reggio, and Jean Yves Trépanier. **Isotropic Color Gradient for Simulating Very High-Density Ratios with a Two-Phase Flow Lattice Boltzmann Model**. *Computers & Fluids*, **48**:98–112, 2011. 34

[122] E. Buckingham. **On Physically Similar Systems; Illustrations of the Use of Dimensional Equations**. *Physical Review*, **4**:345–376, October 1914. 35

[123] Yonghao Zhang, Rongshan Qin, and David R. Emerson. **Lattice Boltzmann Simulation of Rarefied Gas Flows in Microchannels**. *Physical Review E*, **71**, April 2005. 36

[124] M. Latva-Kokko and Daniel H. Rothman. **Static Contact Angle in Lattice Boltzmann Models of Immiscible Fluids**. *Physical Review E*, **72**:046701, October 2005. 37

[125] Sebastien Leclaire, Kamilia Abahri, Rafik Belarbi, and Rachid Bennacer. **Modeling of Static Contact Angles with Curved Boundaries Using a Multiphase Lattice Boltzmann Method with Variable Density and Viscosity Ratios**. *International Journal for Numerical Methods in Fluids*, **82**:451–470, 2016. 38, 40

[126] Hang Ding and Peter D. M. Spelt. **Wetting Condition in Diffuse Interface Simulations of Contact Line Motion**. *Physical Review E*, **75**:046708, April 2007. 39

[127] Sébastien Leclaire, Andrea Parmigiani, Orestis Malaspinas, Bastien Chopard, and Jonas Latt. **Generalized Three-Dimensional Lattice Boltzmann Color-Gradient Method for Immiscible Two-Phase Pore-Scale Imbibition and Drainage in Porous Media**. *Physical Review E*, **95**:033306, 2017. 40

[128] Royal Eugene Collins. *Flow of Fluids through Porous Materials*. Pennwell books, 1961. 45

[129] Changyong Zhang, Mart Oostrom, Jay W. Grate, Thomas W. Wietsma, and Marvin G. Warner. **Liquid CO2 Displacement of Water in a Dual-Permeability Pore Network Micromodel**. *Environmental Science & Technology*, **45**:7581–7588, September 2011. 46, 73

[130] Riyadh Al-Raoush and Apostolos Papadopoulos. **Representative Elementary Volume Analysis of Porous Media Using X-Ray Computed Tomography**. *Powder Technology*, **200**:69–77, June 2010. 47

[131] Peter Dietrich, Rainer Helmig, Martin Sauter, Heinz Hötzl, Jürgen Köngeter, and Georg Teutsch. *Flow and Transport in Fractured Porous Media*. 2005. 49

[132] S. Majid Hassanizadeh and William G. Gray. **Thermodynamic Basis of Capillary Pressure in Porous Media**. *Water Resources Research*, **29**:3389–3405, 1993. 51, 100

[133] Mark L. Porter, Marcel G. Schaap, and Dorthe Wildenschild. **Lattice-Boltzmann Simulations of the Capillary Pressure–Saturation–Interfacial Area Relationship for Porous Media**. *Advances in Water Resources*, **32**:1632–1640, November 2009. 51

[134] Brooks Corey, R. *Hydraulic Properties of Porous Media*. Colorado State University, Fort Collins, Colorado, 1964. 52, 53

[135] A. T. Corey. **Measurement of Water and Air Permeability in Unsaturated Soil 1**. *Soil Science Society of America Journal*, **21**:7–10, January 1957. 53

[136] C. M. Pooley, H. Kusumaatmaja, and J. M. Yeomans. **Modelling Capillary Filling Dynamics Using Lattice Boltzmann Simulations**. *The European Physical Journal Special Topics*, **171**:63–71, April 2009. 56

[137] Andreas G. Yiotis, John Psihogios, Michael E. Kainourgiakis, Aggelos Papaioannou, and Athanassios K. Stubos. **A Lattice Boltzmann Study of Viscous Coupling Effects in Immiscible Two-Phase Flow in Porous Media**. *Colloids and Surfaces A: Physicochemical and Engineering Aspects*, **300**:35–49, 2007. 59

[138] Edo S. Boek and Maddalena Venturoli. **Lattice-Boltzmann Studies of Fluid Flow in Porous Media with Realistic Rock Geometries**. *Computers and Mathematics with Applications*, **59**:2305–2314, 2010. 59

[139] Dong Hun Kang and Tae Sup Yun. **Minimized Capillary End Effect during CO2 Displacement in 2D Micromodel by Manipulating Capillary Pressure at the Outlet Boundary in Lattice Boltzmann Method**. *Water Resources Research*, **54**:895–915, 2018. 63

[140] B. Dong, Y. Y. Yan, and W. Z. Li. **LBM Simulation of Viscous Fingering Phenomenon in Immiscible Displacement of Two Fluids in Porous Media**. *Transport in Porous Media*, **88**:293–314, 2011. 66

[141] Amer M. Alhammadi, Ahmed AlRatrout, Kamaljit Singh, Branko Bijeljic, and Martin J. Blunt. **In Situ Characterization of Mixed-Wettability in a Reservoir Rock at Subsurface Conditions**. *Scientific Reports*, **7**:1–9, September 2017. 70

[142] M. Rücker, W.-B. Bartels, K. Singh, N. Brussee, A. Coorn, H. van der Linde, A. Bonnin, H. Ott, S. M. Hassanizadeh, M. J. Blunt, H. Mahani, A. Georgiadis, and S. Berg. **The Effect of Mixed Wettability on Pore Scale Flow Regimes Based on a Flooding Experiment in Ketton Limestone**. *Geophysical Research Letters*, **0**. 70

[143] Jacob Bear. *Dynamics of Fluids in Porous Media*. Courier Corporation, 2013. 73, 74

[144] Dipsikha Debnath, James S Gainer, Can Kilic, Doojin Kim, Konstantin T Matchev, and YuanPao Yang. **Identifying Phase-Space Boundaries with Voronoi Tessellations**. *The European Physical Journal C*, **76**:645, 2016. 73

[145] Martin J Blunt. **Pore Level Modeling of the Effects of Wettability**. *SPE Journal*, **2**:494–510, 1997. 74

[146] Anthony J. C. Ladd. **Numerical Simulations of Particulate Suspensions via a Discretized Boltzmann Equation. Part 1. Theoretical Foundation**. *Journal of Fluid Mechanics*, **271**:285–309, July 1994. 75

[147] Can Ulas Hatiboglu and Tayfun Babadagli. **Pore-Scale Studies of Spontaneous Imbibition into Oil-Saturated Porous Media**. *Physical Review E*, **77**:1–11, 2008. 75

[148] E. R. Rangel-German and A. R. Kovscek. **A Micromodel Investigation of Two-Phase Matrix-Fracture Transfer Mechanisms**. *Water Resources Research*, **42**, March 2006. 78, 85, 95

[149] John Shipley Rowlinson and Benjamin Widom. *Molecular Theory of Capillarity*. Courier Corporation, 2013. 78

[150] Piotr Garstecki, Michael J. Fuerstman, Howard A. Stone, and George M. Whitesides. **Formation of Droplets and Bubbles in a Microfluidic T-Junction—Scaling and Mechanism of Break-Up**. *Lab on a Chip*, **6**:437–446, 2006. 83

[151] M. De Menech, P. Garstecki, F. Jousse, and H. A. Stone. **Transition from Squeezing to Dripping in a Microfluidic T-Shaped Junction**. *Journal of Fluid Mechanics*, **595**:141–161, January 2008. 83

[152] Haihu Liu and Yonghao Zhang. **Droplet Formation in a T-Shaped Microfluidic Junction**. *Journal of Applied Physics*, **106**:034906, August 2009. 83

[153] Can Ulas Hatiboglu and Tayfun Babadagli. **Oil Recovery by Counter-Current Spontaneous Imbibition: Effects of Matrix Shape Factor, Gravity, IFT, Oil Viscosity, Wettability, and Rock Type**. *Journal of Petroleum Science and Engineering*, **59**:106–122, October 2007. 90

[154] David T. Snow. **Rock Fracture Spacings, Openings, and Porosities**. *Journal of the Soil Mechanics and Foundations Division*, **94**:73–92, 1968. 94

[155] T. Bai, D. D. Pollard, and H. Gao. **Explanation for Fracture Spacing in Layered Materials**. *Nature*, **403**:753–756, February 2000. 94

[156] Orlando J. Ortega, Randall A. Marrett, and Stephen E. Laubach. **A Scale-Independent Approach to Fracture Intensity and Average Spacing Measurement**. *AAPG Bulletin*, **90**:193–208, February 2006. 94

[157] J. Gong and W. R. Rossen. **Characteristic Fracture Spacing in Primary and Secondary Recovery for Naturally Fractured Reservoirs**. *Fuel*, **223**:470–485, July 2018. 94

[158] Nicolas P. Roussel and Mukul M. Sharma. **Optimizing Fracture Spacing and Sequencing in Horizontal-Well Fracturing**. *SPE Production & Operations*, **26**:173–184, May 2011. 94

[159] Jonathan Morrill and Jennifer Lynne Miskimins. **Optimization of Hydraulic Fracture Spacing in Unconventional Shales**. In *SPE Hydraulic Fracturing Technology Conference*. Society of Petroleum Engineers, January 2012. 94

[160] Kan Wu and Jon E. Olson. **Investigation of the Impact of Fracture Spacing and Fluid Properties for Interfering Simultaneously or Sequentially Generated Hydraulic Fractures**. *SPE Production & Operations*, **28**:427–436, November 2013. 94

[161] C.J. Jin, Leopoldo Sierra, and Mike Mayerhofer. **A Production Optimization Approach to Completion and Fracture Spacing Optimization for Unconventional Shale Oil Exploitation**. In *Unconventional Resources Technology Conference, Denver, Colorado, 12-14 August 2013*, pages 601–612, Denver, Colorado, USA, August 2013. Society of Exploration Geophysicists, American Association of Petroleum Geologists, Society of Petroleum Engineers. 94

[162] Chongxun Pan, Jan F. Prins, and Cass T. Miller. **A High-Performance Lattice Boltzmann Implementation to Model Flow in Porous Media**. *Computer Physics Communications*, **158**:89–105, April 2004. 100